Max-Planck-Institut
für Plasmaphysik

Characterization of α-Particle Transport in Reactor Relevant Burning Plasmas

by

Alena Gogoleva

a dissertation presented to
Universidad Carlos III de Madrid
in candidacy for the degree of
Doctor en Plasmas y Fusión Nuclear
and to
Gent University
in candidacy for the degree of
Doctor of Engineering Physics

Advisor: Prof. Dr. Victor Tribaldos

Co-Advisor: Dr. Craig Beidler
Promotor: Prof. Dr. ir. Kristel Crombé

Leganés, July 2020

Acknowledgments

I owe my profound gratitude and sincere thanks to many people, without whom the completion of this thesis would not have been possible.

First and foremost, I would like to express my deepest appreciation to my supervisor, Victor Tribaldos, for his invaluable guidance and persistent help in every aspect of the research process. I am forever grateful to you for teaching me to form expectations at the beginning and motivating me to reach maximum results at the end.

I would also like to extend my gratitude to my co-advisor, Craig Beidler, for his unpayable contribution to the thesis and sophisticated comments on my writing. I must also thank the theory department of IPP Greifswald for their hospitality during my numerous research visits.

I am deeply indebted to Jose Miguel Reynolds-Barredo, Raul Sánchez, Jorge Alcusón and Andrés Bustos, whose help along the way led to co-authorship of two publications. Thank you for always keeping your doors open for me.

None of this would be possible for me without Erasmus Mundus educational programmes, I am grateful to every professor, university staff and student involved in it, foremost to professors Guido Van Oost, Jean-Marie Noterdaeme and Kristel Crombé.

Many thanks to my colleagues from the UC3M physics department, who can always colour grey working days with singular conversations over a cup of coffee. I immensely enjoyed working alongside you. I cannot wait to see what new heights you will reach.

I also wish to thank professors Vladimir Rozhansky and Ilya Senichenkov from SPbPU for introducing me to the field of fusion plasmas.

It has been a true pleasure to meet and a great honour to work with such extraordinary gifted people during my Ph.D.

This thesis is dedicated to my family, whose unconditional love, belief and support motivated me to move on. I owe it all to you; especially to my mom, Elena Mitina, who told me 'you are capable of doing whatever you want, just be happy' and I ended up writing this.

I wish to sincerely thank my closest friends for their support along the way. Arina and Elena, you are there for me as far as I can remember myself. Maria, Marina, Julia, Aleksandra, Andrei, Viktor and Egor, thanks for the years of friendship and the trips we share, especially for 800 km of Camino de Santiago and Azores. Dario, Liliana, Nerea, Irena, Milos and Marco, it has been wonderful to share tips and tricks of being an international Ph.D. student with you. Special credit to Elena, who proofread the manuscript; not only you enriched my English with glorious expressions, but also became the best companion in time of the pandemic.

I am thankful to my teachers for shaping me into a researcher, my family for raising me capable of it, my friends for reminding me to do something else.

Alena

Contents

Abstract

Nuclear fusion has the potential to provide humanity with a safe, clean, abundant, efficient and reliable energy source for the generations to come, but up to date finding a viable fusion reactor concept remains an ongoing area of research. One of the main difficulties to attain economically viable magnetically controlled thermonuclear fusion reactors is the confinement of α-particles. These α-particles are responsible of sustaining the extreme temperatures required for nuclear reactions, and their loss poses a serious threat to the reactor operational control and to its plasma-facing components.

In toroidally shaped fusion devices with a non-uniform magnetic field, α-particles with small parallel velocity become trapped between areas of the high field bouncing between reflection points, whose position is highly susceptible to field corrugations. With the exception of symmetric magnetic fields, like those of ideal tokamaks, these so-called trapped α-particles experience non-zero radial average drifts, which might lead to their collisionless losses. There are two principal collisionless mechanisms connecting trapped particle losses with the inhomogeneities of the confining magnetic field. The first is ripple trapping, in which particles fall into local ripples and experience strong radial drifts usually being convective (ballistic). The second mechanism is ripple induced stochastic processes with milder drifts caused by the radial motion of particle reflection points, which result either in the banana tip stochastic diffusion or particle transitions, in which the particles change the orbit type near the reflection points. While the mitigation of these losses is widely considered in the literature on fusion reactor designs, far too little attention was paid to the statistical characterization of the processes underlying collisionless transport of trapped α-particles, whose nature is generally considered diffusive.

This thesis is intended to provide such statistical description and

clarify the nature of collisionless trapped α-particle transport for reactor scale configurations in cases of broken symmetry of the underlying magnetic field. To this end, detailed analyses were performed on large ensembles of α-particle trajectories, calculated with the guiding center orbit following Monte Carlo code MOCA for several magnetic configurations: a purely toroidal model with ITER parameters and four quasi-toroidal stellarators loosely based on NCSX project with different levels of magnetic field symmetry.

The simulations suggest that while the perfect toroidal magnetic field symmetry of the ITER configuration grants perfect confinement, an increasing departure from quasi-toroidal symmetry leads to faster and larger α-particle losses, most of which belong to particles born with a small parallel velocity in areas of a weak magnetic field on the outer midplane of the configurations. Based on the resulting numerical trajectories, novel techniques were developed capable to calculate the fraction of trapped α-particles and identify the orbit types. Estimates show that about a third of the particles are trapped for ITER, and a fifth for the stellarators, independently on the level of symmetry. These trapped particles mainly follow banana orbits and, to a lesser extent, potato, transition and ripple trapped orbits. Statistical analysis was done for the basic parameters of banana orbits, and it was found that the most probable banana width becomes wider, and that the most probable bouncing time becomes longer as configuration departs from toroidal symmetry. The results of the trapped particle fractions and the most probable bouncing times are in agreement with those obtained by an independent numerical procedure based on the depth of the confining magnetic field and the assumption that α-particles move along the filed lines. To that end, a new figure of merit measuring the level of toroidal symmetry was introduced.

The convection velocity and the diffusion transport coefficients were estimated by two methods: using the most probable banana widths and bouncing times, and fitting the time dependence of the moments of the radial probability density functions of banana centers, which were calculated with a new algorithm based on the positions of the reflection points. Their statistical analysis suggests that the collisionless transport of trapped α-particles cannot be properly described as being diffusive when the magnetic configuration departs from symmetry.

The assumption that ripple-enhanced radial transport of trapped

α-particles is diffusive has been extensively used to model experimental data. But it is limited to describe only Gaussian and Markovian transport processes and thus neglects correlations, memory, and spatial effects, that have recently been proved relevant for fusion plasma, especially in cases of turbulent driven transport.

In this thesis, the techniques used in characterizing the non-diffusive dynamics of turbulent transport were adapted to study collisionless α-particle neoclassical transport. To build an effective transport model, α-particle trajectories were analyzed with a whole set of tools imported from fractional transport theory. Using the Eulerian propagator and Lagrangian rescale range $[R/S]$ analysis techniques, the Hurst H, the spatial α and the temporal β exponents appearing in fractional transport theory were estimated to describe non-diffusive transport.

The results for the ideal toroidally symmetric ITER ripple-less magnetic configuration analyzed by the Lagrangian $[R/S]$ method show an almost zero Hurst exponent pointing out, as expected, to the absence of radial transport. While all perfectly confined trapped α-particles were analyzed for ITER, for the four stellarators, only the particles contributing the most to the losses were considered, i.e. α-particles that get lost in the region with the steepest slope in the loss fraction. The estimated spatial and temporal transport exponents found indicate that the underlying nature of transport is non-diffusive with non-Gaussian and non-Markovian statistics. As the level of toroidal symmetry decreases, the presence of spatial correlations, particularly strong anti-correlations, becomes more pronounced. For all stellarators, there are signs of self-similarity and significant memory effects. The agreement in the Hurst exponents, estimated by both the Lagrangian and Eulerian techniques, shows that as the level of quasi-toroidal symmetry increases transport becomes strongly subdiffusive. Although, the validity of the fractional model itself becomes doubtful in the limiting high and low symmetry cases.

The work presented in the thesis can be naturally extended to study the validity of the fractional transport model onto other types of confining magnetic fields and various α-particle-related effects, such as collisions, α-particle birth profiles, etc.

Resumen

La fusión nuclear tiene el potencial de abastecer a la humanidad con una energía segura, limpia, abundante, eficiente y fiable para las generaciones venideras, pero hasta la fecha, encontrar un concepto viable de reactor de fusión es un área de investigación en curso. Una de las mayores dificultades a la hora de conseguir reactores termonucleares económicamente viables es el confinamiento de las partículas α. Estas partículas son las encargadas de mantener las temperaturas extremas que se requieren para las reacciones nucleares y su pérdida supone una seria amenaza para la operación y control del reactor y el de sus componentes en contracto con el plasma.

En dispositivos de fusión con forma toroidal y con un campo magnético no uniforme, las partículas α con una velocidad paralela pequeña, quedan atrapadas entre las zonas del campo alto, rebotando entre puntos, cuya posición es muy sensible a las ondulaciones del campo. Exceptuando los campos magnéticos simétricos, como los de los tokamaks ideales, dichas partículas α atrapadas experimentan derivas radiales promedio distintas de cero, que pueden conducir a pérdidas no colisionales. Hay dos mecanismos principales no colisionales que conectan las pérdidas de partículas atrapadas con las heterogeneidades del campo magnético confinante. El primero es el debido al *ripple trapping*, en el que las partículas caen en *ripples* locales y experimentan fuertes desviaciones radiales que generalmente son convectivas (balísticas). El segundo mecanismo consiste en procesos estocásticos inducidos por los *ripples* donde las leves desviaciones causadas por el movimiento radial de los puntos de rebote de las partículas dan como resultado una difusión estocástica al cambiar la trayectoria las partículas cerca de los puntos de reflexión. Mientras que la mitigación de estas pérdidas ha sido ampliamente estudiada en la literatura relativa a los diseños de reactores de fusión, no se ha prestado mucha atención a la carac-

terización estadística de los procesos de transporte de las partículas α atrapadas no colisionales, cuya naturaleza en general se ha considerado difusiva.

El objetivo de esta tesis es aportar dicha descripción estadística y aclarar la naturaleza del transporte de las partículas α atrapadas no colisionales en configuraciones de tipo reactor cuando hay una ruptura de simetría en su campo magnético. Con este propósito, realizaremos análisis detallados en muestras amplias de trayectorias de partículas α calculadas con el código Monte Carlo MOCA de seguimiento de órbitas del centro guia, para varias configuraciones magnéticas: un modelo puramente toroidal con parámetros de ITER y cuatro stellarators cuasi-toroidales, inspirados en el proyecto NCSX, con diferentes niveles de simetría magnética.

Las simulaciones sugieren que, si bien la perfecta simetría toroidal del campo magnético de la configuración ITER garantiza un confinamiento perfecto, una desviación creciente de la simetría cuasi-toroidal conduce a mayores y más rápidas pérdidas de partículas α, la mayoría de las cuales pertenecen a partículas nacidas con un ángulo de ataque pequeño en regiones de campo magnético bajo en la zona externa del plano ecuatorial de las configuraciones. Sobre la base de las trayectorias numéricas resultantes, se desarrollaron nuevas técnicas capaces de calcular la fracción de partículas α atrapadas e identificar los tipos de órbitas. Las estimaciones muestran que alrededor de un tercio de las partículas están atrapadas para ITER, y un quinto para los stellarator, independientemente del nivel de simetría. Estas partículas atrapadas siguen principalmente órbitas de tipo banana y, en menor medida, órbitas *potatoes*, en tránsito y *ripple trapped*. En el análisis estadístico de los parámetros básicos de las órbitas banana se encontró que el ancho más probable de las bananas se hace mayor, y que el tiempo de rebote más probable se hace más largo cuando la configuración magnétical carece de simetría toroidal. Los resultados de las fracciones de partículas atrapadas y los tiempos de rebote más probables están de acuerdo con los obtenidos por un procedimiento numérico independiente basado en la profundidad del campo magnético confinante y la suposición de que las partículas α se mueven a lo largo de las líneas del campo. Con este propósito, se introdujo una nueva figura de mérito que mide el nivel de simetría toroidal.

Las velocidades convectivas y los coeficientes de difusión se estimaron con dos métodos: utilizando los valores más probables de los

anchos de las banana y los tiempos de rebote y ajustando la dependencia temporal de la función de distribución radial de probabilidad de los centros de las órbitas de las bananas, que se calcularon con un nuevo algoritmo basado en las posiciones de los puntos de reflexión. Su análisis estadístico sugiere que el transporte de las partículas α atrapadas no colisionales no puede ser descrito como difusivo cuando la configuración magnétical pierde la simetría.

La suposición de que el transporte radial de partículas α atrapadas inducido por *ripple* es difusivo se ha utilizado ampliamente para modelar datos experimentales. No obstante, su aplicación se limita a describir solo los procesos de transporte Gaussianos y Markovianos y por lo tanto no tiene en cuenta las correlaciones, la memoria y los efectos espaciales, que recientemente han demostrado ser relevantes en plasmas de fusión, especialmente en casos de transporte turbulento.

En esta tesis, las técnicas utilizadas para caracterizar la dinámica no difusiva del transporte turbulento se adaptaron para estudiar el transporte neoclásico de partículas α no colisionales. Para construir un modelo de transporte efectivo, se han analizado las trayectorias de las partículas α con un conjunto de herramientas importadas de la teoría de transporte fraccionario. Usando las técnicas de propagadores Eulerianos y el anaĺisis $[R/S]$ Lagrangiano, se estimaron el exponente de Hurst H y los exponentes espacial α y temporal β que aparecen en la teoría del transporte fraccionario para describir el transporte no difusivo.

Los resultados para la configuración magnética sin *ripple* de ITER con simetría toroidal ideal analizada por el método $[R/S]$ Lagrangiano muestran un exponente de Hurst casi igual a cero que señala, como se esperaba, la ausencia de transporte radial. Mientras que para ITER se analizaron las trayectorias de todas las partículas α atrapadas perfectamente confinadas, para los cuatro stellarators, solo se consideraron las partículas que más contribuyeron a las pérdidas, es decir, partículas α que se pierden en la región con la pendiente más pronunciada en la fracción de pérdidas. Los exponentes espaciales y temporales estimados que se encontraron indican que la naturaleza subyacente del transporte es no difusiva y con estadísticas no Gaussianas y no Markovianas. A medida que disminuye el nivel de simetría toroidal, la presencia de correlaciones espaciales, particularmente fuertes anti-correlaciones, se vuelve más pronunciada. Para todos los stellarators, hay signos de autosimilaridad y efectos significativos en la memoria. El acuerdo en-

tre los exponentes de Hurst, estimados por las técnicas Lagrangiana y Euleriana, muestra que a medida que el nivel de simetría aumenta, el transporte se vuelve fuertemente subdifusivo. Aunque, la validez del modelo fraccionario en sí mismo se vuelve dudosa en los casos limítes de alta y baja simetría.

El trabajo presentado en esta tesis puede extenderse naturalmente para estudiar la validez del modelo de transporte fraccionario en otros tipos de campos magnéticos confinantes y estudiar varios efectos relacionados con las partículas α, como colisiones, perfiles de nacimiento de las partículas α, etc.

Overzicht

Kernfusie heeft het potentieel om de mensheid een energiebron te verschaffen voor toekomstige generaties die niet alleen veilig en zuiver is (en CO2-vrij), maar ook efficiënt en betrouwbaar, en waarvan de grondstoffen overvloedig aanwezig zijn. Eén geschikte reactor is echter nog steeds in een ontwikkelingsfase. Eén van de grote moeilijkheden om een economisch rendabele magnetisch gestuurde thermonucleaire fusiereactor te realiseren, is de opsluiting van α-deeltjes. Deze α-deeltjes zijn mede noodzakelijk voor het in stand houden van de extreem hoge temperaturen, die nodig zijn voor de kernreacties. Het verlies van α-deeltjes uit de reactor vormt een ernstige bedreiging voor de operationele controle van de reactor en voor onderdelen die met het plasma in contact komen.

Bij torus-vormige fusiemachines met niet-uniforme magneetvelden raken α-deeltjes met een kleine parallelle snelheid, gevangen ('trapped') tussen gebieden van hoge veldsterkte, waardoor ze beginnen stuiteren tussen reflectiepunten. De precieze locatie waarop dit gebeurt, hangt af van de exacte niet-uniformiteit in de magneetveldsterkte. Met uitzondering van symmetrische magnetische velden, zoals die van ideale tokamaks, ervaren deze α-deeltjes radiale gemiddelde drifts die niet nul zijn en die kunnen leiden tot verliezen zonder botsingen ('collisionless'). Er zijn twee mechanismes te onderscheiden bij dit soort verliezen. Het eerste is een opsluiting in magnetische rimpels ('magnetic ripple'). Deeltjes belanden in locale magnetische rimpels en ervaren een sterke radiale drift, die gewoonlijk van het convectie type is (ballistisch). Het tweede mechanisme is een stochastisch proces, dat eveneens door de magnetische rimpels wordt geïnduceerd. Hierbij zijn de drifts milder. Deze soort drifts wordt veroorzaakt door radiale bewegingen van de deeltjes tussen reflectiepunten en resulteert in een stochastische diffusie van de tips van de banaan-vormige ingesloten

bewegingsbaan ('trapped banana orbit') van de deeltjes. Het is ook mogelijk dat deeltjes hierbij overgaan naar een ander type bewegingsbaan in de torus.

Hoewel de beperking van deze verliezen in het algemeen wel wordt overwogen in de literatuur over het ontwerpen van fusiereactoren, werd tot hiertoe weinig aandacht besteed aan het statistisch karakteriseren van de processen die ten grondslag liggen aan het transport zonder botsingen van de ingesloten α-deeltjes, waarvan de aard algemeen als diffuus wordt beschouwd. Dit proefschrift is bedoeld om een dergelijke statistische beschrijving te geven en de aard van dit transport te verduidelijken voor reactor-configuraties waarbij de symmetrie van het onderliggende magnetische veld is verbroken. Daartoe worden gedetailleerde analyses uitgevoerd op grote ensembles van trajecten van α-deeltjes. Deze worden berekend met de zogenaamde 'guiding-center orbit' methode volgens een Monte Carlo-code, en dit voor verschillende magnetische configuraties: een puur toroïdaal model met ITER relevante parameters en vier quasi-toroïdale stellarators, met parameters die zijn geïnspireerd op het NCSX project, en met verschillende niveaus van symmetrie voor het magneetveld.

Simulaties suggereren dat een perfecte symmetrie van het toroïdaal magneetveld in ITER een perfecte opsluiting garandeert. Echter, hoe meer wordt afgeweken van de quasi-toroïdale symmetrie, hoe meer en sneller de α-deeltjes uit de reactor verdwijnen. Het zijn voornamelijk de α-deeltjes die zijn geboren met een kleine parallelle snelheid in gebieden met een zwak magneetveld (i.e. aan de buitenzijde van de torus).

Gebaseerd op de resulterende numerieke banen van de deeltjes, werden nieuwe technieken ontwikkeld waardoor de fractie van ingesloten ('trapped') α-deeltjes kunnen worden bepaald en ook de eigenschappen van hun bewegingsbaan. Een derde van de α-deeltjes in ITER doorlopen naar schatting een dergelijke ingesloten bewegingsbaan. Voor een stellarator is dat ongeveer een vijfde, ongeacht het niveau van symmetrie. De baan van deze deeltjes is voornamelijk van het banana-type ('banana orbits'). Er zijn ook deeltjes op zogenaamde 'potato-orbits', alsook op transitie-banen en andere zitten gevangen in de magnetische veld rimpels ('ripple trapped orbits'). Een statistische analyse werd uitgevoerd voor basisparameters van de banana-orbits. Er kon worden geconcludeerd dat als de configuratie meer afwijkt van een symmetrie toestand, zal de baan verbreden en de tijd dat

het deeltje stuitert tussen de uiteinden, zal toenemen. De resultaten voor de fractie van ingesloten deeltjes en voor de meest waarschijnlijke stuiter-tijd zijn in overeenstemming met resultaten van een onafhankelijke numerieke procedure die is gebaseerd op de diepte van het opsluitend magneetveld en de veronderstelling dat α-deeltjes zich bewegen langs de lijnen van het magneetveld. Hiervoor werd een nieuwe karakteristieke eigenschap gedefinieerd die het niveau van de toroïdale symmetrie beschrijft.

De convectie-snelheid en diffusiecoëfficiënten voor het transport werden geschat door middel van twee verschillende methodes: (i) gebruik makend van de meest waarschijnlijke breedte van de banaanvormige baan en de stuiter-tijden, en (ii) door het fitten van de tijdsafhankelijkheid van de momenten van de radiale waarschijnlijkheidsdistributie functie van de centra van de banana-orbit. Deze centra werden berekend met een nieuw algoritme op basis van de reflectiepunten van de baan. De statistische analyse suggereert dat het transport zonder botsingen van ingesloten α-deeltjes niet goed kan worden beschreven als louter diffuus wanneer de magnetische configuratie niet symmetrisch is.

De veronderstelling dat een verhoogd radiaal transport van ingesloten α-deeltjes door magnetische rimpels, diffuus van aard is, werd tot hiertoe nochtans uitgebreid toegepast om experimentele data te modelleren. Het is echter beperkt en kan enkel Gaussiaanse of Markoviaanse transport processes beschrijven. Het houdt geen rekening met correlaties, geheugen-effecten of ruimtelijke invloeden. Aspecten die niettemin recent relevant zijn gebleken voor fusieplasma's, in het bijzonder bij de turbulente transportprocessen.

In de thesis werden precies deze technieken die de niet-diffuse dynamica van turbulent transport beschrijven, toegepast op de studie van het neoklassiek transport van α-deeltjes zonder botsingen. Om een effectief transportmodel te bouwen, werden de trajecten van α-deeltjes geanalyseerd door middel van technieken geïmporteerd uit de fractionele transporttheorie. Gebruik maken van een Euler propagator en een Lagrangiaanse herschalingsbereik $[R/S]$ analyse, werden de Hurst H, de ruimtelijke α en de tijdsafhankelijke β exponenten, die verschijnen in de fractionele transporttheorie, geschat. Zo kon het niet-diffuse aandeel van het transport worden beschreven.

De resultaten voor ITER met de Langrangiaanse $[R/S]$ methode, in een ideale configuratie, die toroïdale symmetrisch is en zonder rip-

ple, geven een Hurst exponent die bijna nul is. Dit stemt overeen met de verwachting dat er geen radiaal transport is. Voor de ITER configuratie werden alle ingesloten α-deeltjes geanalyseerd. Voor de vier stellarator configuraties, werden enkel de deeltjes in rekening gebracht die het meest bijdragen tot de verliezen, i.e. α-deeltjes die verloren raken in de regio met de meest steile helling van de verliesfractie. De geschatte ruimtelijke en temporele transportexponenten geven aan dat de onderliggende aard van het transport niet diffuus is met niet-Gaussiaanse en niet-Markoviaanse statistieken. Wanneer de toroïdale symmetrie afneemt, worden de aanwezigheid van ruimtelijke correlaties meer uitgesproken, in het bijzonder sterke anti-correlaties worden waargenomen. Voor alle stellarators zijn er tekenen van zelfgelijkvormigheid en aanzienlijke geheugeneffecten. De overeenkomst in de Hurst exponent, geschat zowel met Lagrangiaanse als Euleriaanse technieken, toont aan dat het transport sterk sub-diffuus wordt als het niveau van quasi-toroïdale symmetrie toeneemt. In de limiet van hoge en van lage symmetrie wordt de toepasbaarheid van het fractionele model evenwel twijfelachtig.

Het werk dat in de thesis is voorgesteld, kan nog worden uitgebreid om de toepasbaarheid van het fractionele transportmodel op andere types van magnetische opsluiting te bestuderen, evenals verschillende effecten die verband houden met α-deeltjes, zoals botsingen, profielen waar de α-deeltjes worden geboren, etc.

Published & Submitted Content

Articles or other contributions (co)-authored by the Doctoral candidate that are included as part of the thesis and that have been published:

- A. Gogoleva, V. Tribaldos, J.M. Reynolds-Barredo and C.D. Beidler. "*Statistical description of Collisionless α-particle transport in cases of broken symmetry: from ITER to quasi-toroidally symmetric stellarators*". Nuclear Fusion **60**, 056009 (2020).

  https://doi.org/10.1088/1741-4326/ab7936

  This item is wholly included in Chapter 2. The material from this source that is included in this thesis has not been singled out with typographic means; appropriate references are made. Reproduced here with permission of the copyright owner, *Institute of Physics (IOP).*

Articles or other contributions (co)-authored by the Doctoral candidate that are included as part of the thesis and that have been accepted for publication:

- A. Gogoleva, V. Tribaldos, J.M. Reynolds-Barredo, R. Sánchez, J. Alcusón and A. Bustos. "*Non-diffusive nature of collisionless α-particle transport: dependence on toroidal symmetry in stellarator geometries*". Physics of Plasmas, (2020).

  This item is wholly included in Chapter 3. The material from this source that is included in this thesis has not been singled out with typographic means; appropriate references are made. Reproduced here with permission of the copyright owner, *AIP Publishing.*

Articles or other contributions (co)-authored by the Doctoral candidate that are not included in this thesis:

- A. Gogoleva and V. Tribaldos. "*Evaluation of fast particle transport for quasi-symmetrical magnetic fields*". 44th European Physical Society Conference, Belfast (2017).

Chapter 1

Introduction

1.1 Nuclear Fusion

1.1.1 Energy demand

The energy demand of humanity has tremendously escalated for the past centuries and keeps increasing in recent times. According to the BP Statistical Review of World Energy (2019) [1], by earlier 2000 the yearly global primary energy consumption - the total energy received from all energy resources and consumed by mankind in all sectors of the economy in each country - has increased tenfold over the past century. The nuclear and hydropower made up for $\sim 5\%$ of the energy supply, biofuels $\sim 10\%$, natural gas 20%, coal 25% and crude oil 40%. Just over the last 20 years the global energy consumption grew by almost 50%, which was provided by the same key sources in the energy market (mainly fossil fuels) in similar percentage with a small contribution $\sim 1.5\%$ of the renewable sources as wind and solar. Looking at the world regional statistics, the Asian Pacific market - known as a region with by far the largest economic boost and digital revolution - is mainly responsible for increased energy demand, as between 2000 and 2018 it more than doubled its primary energy consumption. The regional energy infrastructure is closely tied to its economic situation. Since the difference in energy consumption between developed and developing countries reduces globally, the International Energy Agency (IEA) gave a projection in the World Energy Outlook 2019 [2] that by 2040, the global energy demand will increase by at least 20%. The energy market should be ready to meet the needs of energy services,

both industrial and domestic, in the long run.

Currently, most of the energy is generated by non-renewable sources like fossil fuels. The non-sustainable energy production has numerous negative effects for humanity and the environment, which may be immediate or deferred until next generations. Accidents at nuclear power plants, such as the Chernobyl 1986 and the Fukushima Daiichi 2011 disasters, had an instant dramatic impact on both of them. The cumulative effects of energy production are no less dangerous, like high life-threatening risks related to fossil fuels production; negative impact due to storage of radioactive waste; floodings; the rise of sea levels; ozone depletion, greenhouse effect and deforestation that keep escalating the global warming. Our society requires clean, inexhaustible, sustainable and environmentally friendly sources of energy as soon as possible. According to the IEA [2], in 20 years the renewable solar and wind power plants might become key components of the world installed power generation capacity. Currently, both are at the same level of the installed power generation capacity. In the next 15 years solar energy generation is expected to be the same as of gas and by 2040 outpace all other sources. Nevertheless, the renewable energy sources have numerous downsides, such as their short lifespan, cost-effectiveness, manufacture pollutions, unoptimized disposal, and strong dependence on weather conditions, since no sufficiently large energy store systems are available yet.

An alternative sustainable concept is nuclear fusion. Nuclear fusion rests on a brilliant and elegant idea of recreating a reaction similar to the one that powers stars under controlled conditions here on Earth. Nuclear fusion has a potential to provide stable, safe, environmentally friendly and large-scale power supply, as the fuel sources, mainly Deuterium and Lithium for the planed future reactors, are abundant in nature, and greenhouse gas emissions are zero. Though, thermonuclear fusion reactors will be cataloged as radioactive installations, they can be decommissioned and dismantled in just 100 years after their shutdown. Moreover, the amount of radioactive fuels in the reactor at any time will be minute, and runaway nuclear chain reactions are inherently impossible.

1.1.2 Fusion basic concept

Nuclear fusion is a reaction where two light nuclei are combined, *fused*, into a heavier one. Future fusion reactors will harness the kinetic energy of the reaction products due to the mass defect in accordance with Einstein's famous mass-energy equivalence equation $E = mc^2$.

Fusion reaction requires temperatures in the range of 10-100 kilo-electron Volts (keV) at which matter can exist only in the plasma state. Plasma is a state of matter being a quasi-neutral mixture of charged particles. Stars are an example of burning plasma in nature, where the temperatures are high enough for nuclei to overcome the Coulomb electrostatic repulsion and trigger fusion nuclear reactions, that in turn further increase both the temperature and the pressure needed to sustains the reactions. The Sun is powered by proton-proton chain fusion reaction, converting $\Delta m = 4 \cdot 10^9$ kg of matter into energy per second.

Since gravitational confinement cannot be used to replicate the conditions inside stars, two alternative methods have been developed to attain net energy gain by fusion reactions on Earth: Inertial and Magnetic confinement. The former produce fusion conditions through the implosion of hydrogen fuel pellets using powerfull laser pulses. The latter creates, shapes and contains plasma in a chamber with magnetic fields created by, usually superconducting, electromagnets.

To achieve and control thermonuclear reactions, the reactants must retain their energy within a reacting region for sufficient time. A criteria developed by Lawson [3] is used to estimate how far a plasma is from achieving fusion conditions. This criteria states that the product of density n, energy confinement time τ_E (that measures how fast the plasma looses its energy) and temperature T must be $\sim 3 \cdot 10^{21}$ m^{-3} s keV. While the inertial fusion reaction proceeds for short times, picoseconds, at high densities, 10^{30} particles per cubic meter, the magnetic confinement takes place for moderate times, seconds, at low densities, 10^{20} particles per cubic meter. This work is focused on magnetic confinement fusion.

In fusion reaction, the energy released per nucleon peaks for the lightest elements with low binding energy. Table 1.1 lists the fusion reactions for hydrogen isotopes with the smallest threshold energies together with the released energies [4].

The Deuterium-Trtium D-T reaction has the largest nuclear cross-

Table 1.1: Optimal terrestrial fusion reactions together with threshold energy required for their activation and released energies.

Reactants	Byproducts and Energy released	Threshold energy
D+T	^{4}He (3.5 MeV) + n (14.1 MeV)	10 keV
D+^{3}He	^{3}He (3.7 MeV) + p (14.7 MeV)	30 keV
D+D	T (1 MeV) + p (3 MeV)	35 keV
D+D	^{3}He (0.8 MeV) + n (2.5 MeV)	35 keV

section at lower temperatures and is the easiest to achieve [5]. While Deuterium is stable, available in abundance in sea water and could be injected directly in a plasma, Tritium cannot be found in nature because of its fast disintegration rate but could be bred from Lithium in a reactor. A lithium blanket facing the plasma will be installed for this purpose and to slow down the energetic neutrons from the fusion reaction. The consumables are therefore Dueterium and Lithium, where Tritium is just an *intermediate* fuel.

The byproducts of D-T reaction serve different purposes. Being charged, α-particles stay inside the confining magnetic field and transfer their high energy to the rest of the plasma species through collisions. The combination of neutrons and Lithium plays a double role. At high energy, the nuclear reaction with Lithium produces Tritium, while at low energy, Lithium thermalises neutrons. The deposited energy is transferred to a heat exchange circuit to initiate a conventional electricity production cycle.

In steady state conditions, the power balance is attained when the power generated by α-particles and external power sources compensates the plasma power losses. There are two main loss mechanisms in the plasma: particle power losses and radiative losses (mainly Bremsstrahlung). The fusion device performance is characterized by the fusion gain factor Q, which is the ratio of the total produced fusion power to the external input power: $Q = P_{fus}/P_{ext}$. When the two powers compensate each other, $Q = 1$, the fusion reactor can sustain the plasma in steady state. This condition is usually called *breakeven*. Ignition is attained when the plasma can be sustained without any external power, $Q \to \infty$, i.e. solely by α-particle heating. A commercially viable fusion reactor should exceed *breakeven* and operate a burning plasma with predominantly P_α heating, corresponding to

$Q \geq 5 - 10$ for D-T reactions.

So far, the biggest laboratory fusion device, the Joint European Torus JET, was very close to breakeven, reaching $Q \sim 0.67$. The next fusion experiment, ITER (International Thermonuclear Experimental Reactor), which is under construction in the south of France should operate between $Q = 5$ and 10. The international fusion community has already begun designing the first demonstration nuclear power station DEMO to put net fusion energy into the grid.

1.1.3 Fusion devices

The first fusion reactors will use D-T reactions; i.e. the least energy demanding nuclear reaction [5] has to fulfill the Lawson criteria $n\tau_E T \sim 3 \cdot 10^{21}$ m^{-3} s keV, where n and T are the plasma density and temperature and τ_E is the energy confinement time. Whereas the plasma density can be modified injecting more fuel (though with some limitations due to plasma instabilities), the achieved temperature depends on both the power injected and the confinement time. For example, for a 1 meter container at the temperature necessary for D-T reactions, ions average thermal speed is around 10^6 m/s, and the confinement time for a free expanding gas is around 1μs. Since the plasma is composed of charged particles, one possible way to increase the confinement time (or to reduce the speed at which ions leave the reactor) is to use magnetic fields.

In the simplified case of a uniform magnetic field, charged particles are forced to gyrate and move along the magnetic field lines. To guide and contain particles, the magnetic field lines must be bend into a toroid to avoid the losses at the ends. However, in a purely toroidal field, the curvature and gradient of magnetic field cause charge separation that leads to outward particle drifts and plasma loss. To counterbalance this effect, additional poloidal B_θ and to a lesser extend vertical magnetic field B_v components are required. In the resulting helical field $\vec{B} = \vec{B_\varphi} + \vec{B_\theta} + \vec{B_v}$, the magnetic field lines wrap around the plasma column and form a set of nested closed magnetic surfaces. There are two main ways to generate the required poloidal component of the magnetic field B_θ, depending on whether the needed electric current flows in a set of coils, as it does in stellarators, or in the plasma itself like in tokamaks.

Figure 1.1 illustrates the schematic of the key components and

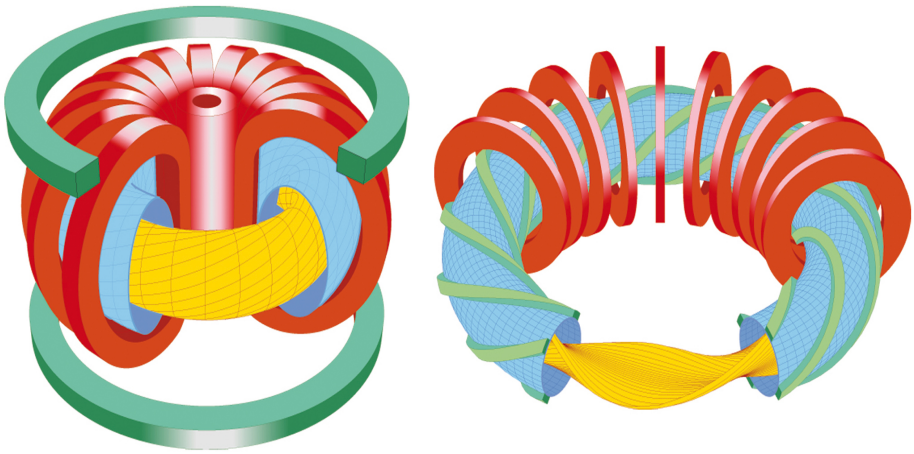

Figure 1.1: Classical tokamak (left): transformer (pink cylinder), poloidal field coils (green), toroidal field coils (red), vacuum chamber (blue) and plasma (yellow). Classical stellarator (right): toroidal coils (red), helical coils (green), vacuum chamber (blue) and plasma (yellow).

resulting plasma column of a classical tokamak (left) and a classical stellarator (right) [6]. In tokamaks, the toroidal field coils (red) surrounding the vacuum vessel (blue) generate a toroidal magnetic field $\vec{B_\varphi}$, and the plasma itself (yellow) creates the poloidal field $\vec{B_\theta}$ using the same principle as an electrical transformer, where a time increasing current in a central solenoid acts as the primary circuit and the plasma as the secondary circuit. The outer poloidal field coils (green) are used for positioning, shaping and stabilizing the plasma column. Except for the small wobbling effect due to the finite number of toroidal field coils, tokamak plasmas may be considered two dimensional, something that significantly simplifies any analytical or numerical analysis. However, in tokamaks it is the plasma that creates the indispensable poloidal magnetic field component, on which the plasma confinement relies. This makes the problem of plasma confinement non-linear since the plasma is responsible for its own confinement.

Stellarators do not rely on the plasma to create any of the required magnetic fields, in fact, the magnetic surfaces exist there even in the absence of plasma. A classical stellarator (Figure 1.1 right) besides

toroidal field coils (red) has helically shaped coils (green) that are wrap around the vacuum vessel (blue). The resulting plasma column (yellow) is twisted and is fully tridimensional. Helical fields could be either formed by torsatron-like coils, where each coil wraps around the vessel (like ivy around a tree brunch) and can repeat itself N times giving raise to a multiple period device, or by modular coils of different three-dimensional shapes surrounding the vessel at a certain toroidal position just as toroidal coil does. The stellarator construction challenges both engineers to manufacture the coils and physicists to analyze fields and plasmas, yet they grant a moderate non-linear plasma description as most of the confining magnetic field is created by coils. Moreover, its 3D geometry could be used as an advantage, since it gives more freedom to optimize the magnetic field.

1.1.4 Quasi-symmetry

One of the strategies to optimize the magnetic field of stellarators is to make them *tokamak-like*, that is, to create configurations with confinement properties that resemble the properties of the symmetric magnetic field of a tokamak but without their dependence on plasma currents. Such configurations are referred to as *quasi-toroidally symmetric stellarators*.

Boozer coordinates

Prior to considering the question of stellarator optimization it is useful to introduce a suitable coordinate system. The coordinates for describing the magnetic field of fusion devices must be adapted to the toroidal shape of the flux surfaces. The coordinate system, where the toroidal magnetic field has a simplified expression, is usually referred to as the flux coordinates, i.e. one of the coordinate is a flux surface label.

One of the most commonly used flux coordinates is the Boozer coordinates [7], whose distinctive feature is the fact that the magnetic field lines are straight. In Boozer coordinates (ψ, θ, φ), the toroidal magnetic field flux ψ is used as the radial coordinate, φ is the geometrical toroidal angle, and θ is a curvilinear periodic poloidal angle defined to make magnetic field lines straight. Thus, a magnetic field line could be expressed as $\theta + \iota(\psi)\varphi = a$, where ι is the slope of θ vs

φ and does not change from point to point on the flux surface, and a is a constant. It is important to note that these coordinates are non-orthogonal and only valid for closed flux surfaces.

The magnetic field in Boozer coordinates $\vec{B} = \vec{B}(\psi, \theta, \varphi)$ can be written in covariant and contravariant representations as:

$$\begin{aligned} \vec{B} &= g\nabla\varphi + I\nabla\theta \qquad \text{covariant} \\ \vec{B} &= \nabla\psi \times \nabla\theta + \iota\nabla\varphi \times \nabla\psi \qquad \text{contravariant} \end{aligned}$$

where g is the poloidal current outside a flux surface and I is the toroidal current within a flux surface. The volume element is given by $d^3r = J(\psi, \theta, \varphi)d\psi d\varphi d\theta$ with the Jacobian of the transformation being $J \sim B^2/(g + \iota I)$.

Using Boozer coordinates, a Fourier-decomposition of the magnetic field for each flux surface could be written as:

$$B(\psi, \theta, \varphi) = \sum_{m,n} [{}^{s}B^{\psi}_{mn} \sin(m\theta - n\varphi) + {}^{c}B^{\psi}_{mn} \cos(m\theta - n\varphi)] \quad (1.1)$$

where ${}^{s,c}B^{\psi}_{mn}$ are the flux functions, m and n are a pair of integers.

Quasi-symmetry

In magnetically controlled fusion devices, the confinement in based on reducing the radial particle drifts. To improve particle confinement the magnetic field is optimized to reduce particle losses [8].

Magnetic fields ensuring zero time-averaged radial drifts are called *omnigenous* [9]. There are two common ways to achieve omnigeneity: to endow the magnetic field with *isodynamicity* or *symmetry*. In isodynamicity, the contours of constant magnetic field strength are closed poloidally, making particles to precess poloidally around the torus. An example of a configuration *approaching* isodynamicity, for this reason being called *quasi-isodynamic*, is Wendelstein 7-X stellarator [10] operating in IPP Greifswald, Germany.

In Boozer coordinates, the magnetic field strength of symmetric configurations is a function of the radial coordinate and just one of the two angular coordinates or a fixed linear combination of them: $B = B(\psi, m\theta - n\varphi)$. There are three types of symmetries [11], whose constant-B curves are closed:

i) Toroidal Symmetry: $n = 0$;
ii) Poloidal Symmetry: $m = 0$;
iii) Helical Symmetry: m and n are non-zero.

In realistic toroidal fusion devices, perfect symmetry is unattainable and can only be approached approximately, what is usually referred to as *quasi-symmetry*. Magnetic fields with quasi-toroidal symmetry besides a dominant B_{m0} harmonic have other $B_{mn} \neq 0$ components in their Fourier decomposition with $n \neq 0$. Similarly, the dominant mode in Boozer representation for quasi-poloidal symmetry is B_{0n}, and for quasi-helical symmetry it is B_{mn}.

Figure 1.2 shows the contours of the constant B of the stellarator designs already implemented or proposed. An example of configuration approaching toroidal symmetry is the NCSX device (National Compact Stellarator eXperiment) from Princeton Plasma Physics Laboratory [12], see Figure 1.2 left. At the same time, the Oak Ridge National Laboratory proposed the quasi-poloidally symmetric configuration named Quasi Poloidal Stellarator (QPS) [13, 14], see Figure 1.2. Quasi-helical symmetry was explored in the Helically Symmetric eXperiment (HSX) project, that was built at the University of Wisconsin-Madison [15], which is a linear combination of angular variables given by $m = 1$ and $n = 4$, see Figure 1.2 right.

Of particular interest is quasi-toroidal symmetry, as it allows to create stellarator configurations with confinement properties close to those of tokamaks but without some of their problems, as their dependence on plasma current to create a magnetic field. In this work, we will consider both tokamaks and quasi-toroidally symmetric stellarators in order to characterize the difference in particle confinement as the magnetic field configuration departs from toroidal symmetry. The confinement of plasma particles is quantified by their level of transport, the main mechanisms of which are discussed in the next chapter.

1.2 Transport basics

Controlled thermonuclear fusion comes down to the task of energy and particle confinement that in turn is determined by charged particle motion. In this case, the strong magnetic field to a large extend determines the microscopic particle dynamics; leaving aside for the moment the transport self-generated by electric and magnetic fields

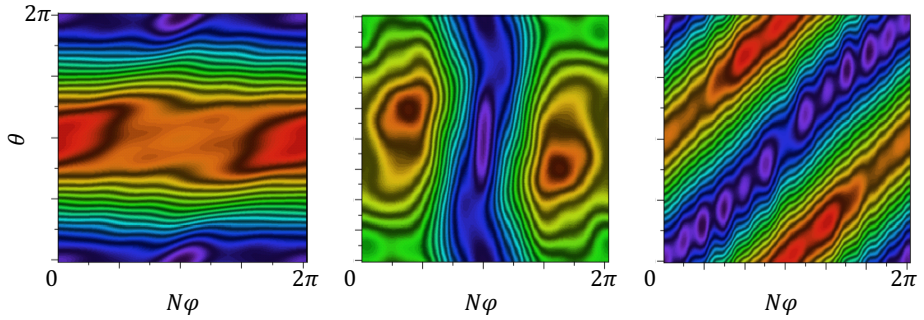

Figure 1.2: Contours of constant magnetic field strength for one field period at half radius for NCSX (left), QPS (centre) and HSX (right) in Boozer coordinates. High/low magnetic field regions appear in red/blue.

that is commonly referred to as turbulent transport.

1.2.1 Classical transport

Sir J. Larmor discovered that in a uniform magnetic field B, the motion of a charged particle consists on a uniform motion along the magnetic field direction at speed $v_\parallel$ and a gyration of radius $\rho_L = v_\perp/\omega_c = mv_\perp/qB$ around the magnetic field, where m and q its charge and mass, $v_\perp$ is perpendicular component if its velocity $\vec{v} = \vec{v}_\perp + \vec{v}_\parallel$ (its pitch $p = v_\parallel/v$) and the cyclotron frequency $\omega_c = qB/m$. In this simplified description, the only mechanism that can disturb particle motion is the interaction with other particles, usually referred to as *collisions*, that can randomly change particle position on a distance of the order of the Larmor radius, see Figure 1.3. This process is known as *classical particle transport*. Since collisions happen randomly, particle trajectory resembles that of a drunkard's walk, who changes the direction with frequency ν over a distance L. This motion is modeled as a random walk process with zero average displacement $< r >= 0$ and linearly growing in time average squared displacement $< r^2 > \sim Dt$, where D is a transport coefficient referred to as the classical diffusion coefficient. For example, the electron classical diffusion coefficient would be $D_{cl} \sim \rho_{L_e}^2 \nu_{ei}$, where ν_{ei} is the fastest electron collision frequency and ρ_{L_e} its Larmor radius.

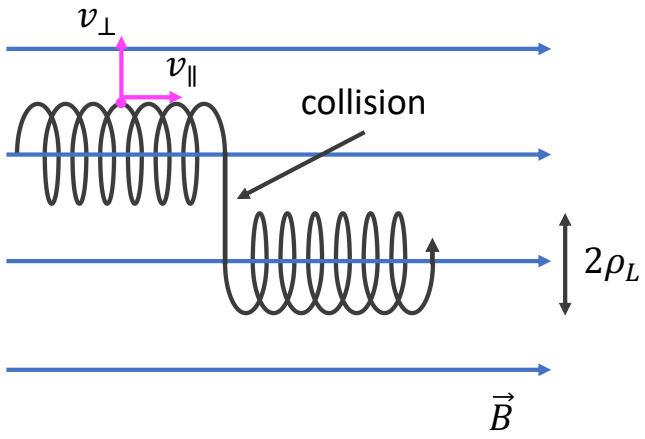

Figure 1.3: Single particle motion in a uniform magnetic field.

1.2.2 Neoclassical transport

In fusion devices - tokamaks and stellarators - the magnetic field is non-uniform and its strong variation and curvature cause other mechanisms to move away particles from the field lines, which surpasses classical transport, the so-called neoclassical transport. In a purely toroidal field a charged particle streams along field line (its gyration could be neglected), but it experiences drifts due to the magnetic field gradient and curvature $\sim \vec{B} \times \vec{\nabla} B$. These drifts cause charge separation, as particles with different signs drift to opposite directions, i.e. up or down, which in turn induces a vertical electric field $\vec{E}$ and $\vec{E} \times \vec{B}$ drift pushing particles away.

The non-uniform magnetic field not only causes drifts but also divides particle trajectories into two types. Figure 1.4 illustrates the schematic of a tokamak with major radius R and a minor radius a, with the two possible ion trajectories either passing or trapped/reflected. On the left, the passing particle has sufficient parallel velocity $v_\parallel$ to overcome the magnetic field change and continue to stream along it. On the right, the trapped or reflected particle due to its small parallel velocity (or small pitch p) is unable to access the regions of high magnetic field and remains in the outer side bouncing back and forth. At the reflection points (where the pitch is zero) particle changes the direction of motion and, accordingly, reverses its pitch sing. The poloidal cross-section of the resulting trajectory resembles a banana and is the

reason for naming them banana orbits. It is customary to characterize these orbits based on the time between two consecutive reflection points, or bouncing time τ, and the banana width Δw, which is radial distance between the two sides of the banana.

The contribution to the transport of passing particles is insignificant, since in the collisionless approximation their average radial drift is zero, and after a collision, their radial displacement is of the order of the Larmor radius. Despite trapped particles represent a minor fraction of a total particle ensemble (the rough estimation of this fractions is $f \sim \sqrt{a/R} = \sqrt{\epsilon}$, where ϵ is the inverse aspect ratio), their radial excursions are of the order of the banana orbit width $\Delta w \sim \rho_L/\iota\sqrt{\epsilon}$ [16]. The resulting neoclassical diffusion coefficient due to trapped particles is more that order of magnitude larger than the classical one: $D_{neo} \sim \Delta w^2 \nu_{eff} \sqrt{\epsilon} = D_{cl}/\iota^2 \epsilon^{3/2}$.

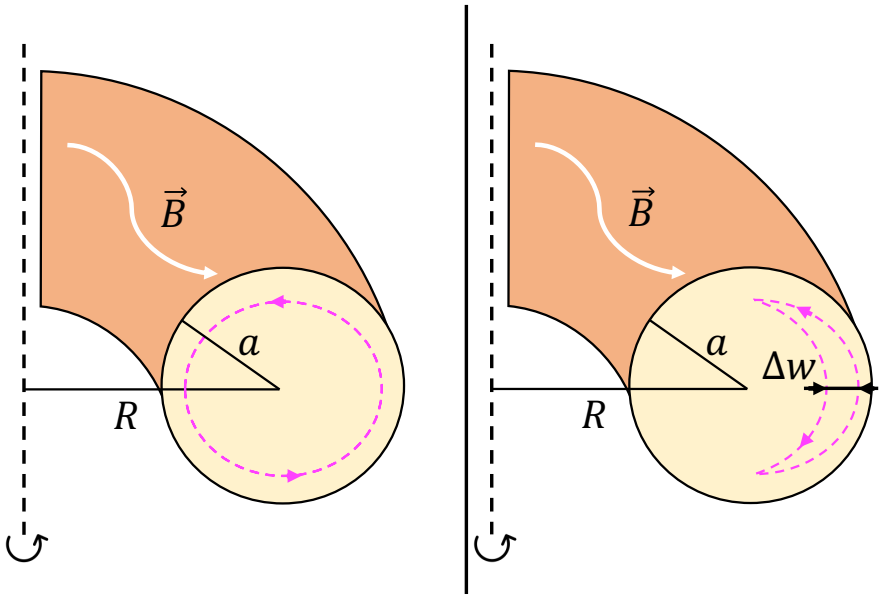

Figure 1.4: Single particle motion in a non-uniform magnetic field of a torus. Left: passing particle orbit. Right: trapped particle orbit.

Neoclassical transport coefficient D_{neo} strongly depends on the collisionality, ν^*, defined as a ratio of effective collision frequency to bounce frequency (characteristic orbit time). Figure 1.5 sketches the overall dependence on collisionality for both tokamaks and stellarators. Three regimes are found for tokamaks [17]: one at high collisionality

with $\nu^* \gtrsim \epsilon^{-3/2}$ called the Pfirsh-Schlüter (PS), where $D \sim \nu^*$; an intermediate one with $1 \lesssim \nu^* \lesssim \epsilon^{-3/2}$, where D is approximately constant, called *Plateau*; followed at low collisionalities $\nu^* \lesssim 1$ by the so-called banana regime, where $D \sim \nu^*$. Two new regimes are found at low collisionalities in stellarators, one with $D \sim 1/\nu^*$, partly due to helically trapped particles, that are localized poloidally and rapidly drift outwards. This deleterious dependence is reduced by the radial electric field through the $\vec{E} \times \vec{B}$ rotation that limits helical particle excursions resulting in a more favorable $D \sim \sqrt{\nu^*}$ dependence.

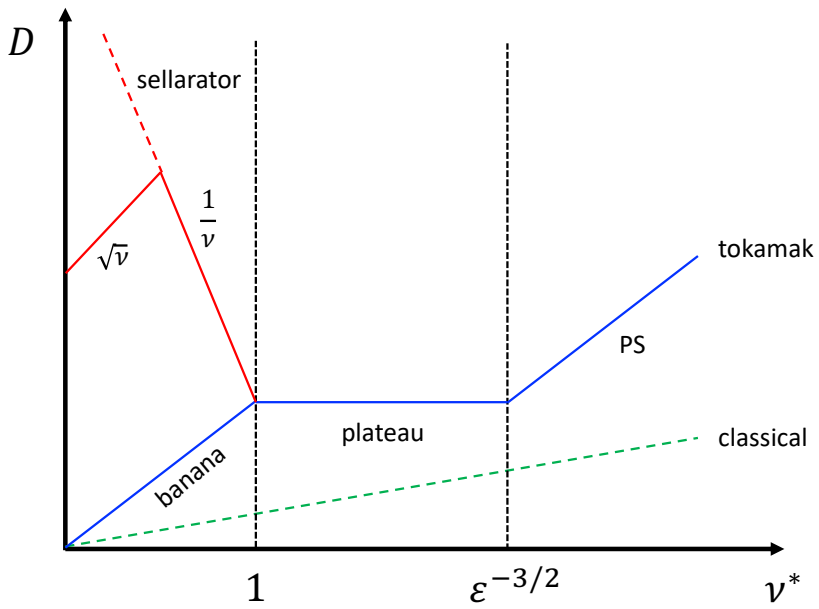

Figure 1.5: Neoclassical diffusion coefficient dependence on collisionality for tokamaks and stellarators.

1.2.3 Turbulent transport

In magnetically confined fusion devices, the unavoidable gradients, arising from quite different temperatures needed for the nuclear reactions and those of the container, represent a huge source of free energy that drives the plasma out of the thermodynamic equilibrium. Nowadays, the consensus is that the main reason explaining the particle

and energy transport across these gradients is self-generated, fluctuating, electric and magnetic fields. This is commonly referred to as turbulent transport. Since the diffusion coefficient could be estimated as $D \sim$ (size of turbulent structure)^2/(correlation time), eddies result in significant level of transport unless they are distorted or broken. Fortunately, turbulence can generate coherent shear flows, that are radially non-uniform (for example, flow is stronger close to the plasma edge than in its core) and are capable to radially decorrelate eddies, thus making them smaller and less transport-relevant. Though, the turbulent transport is beyond the scope of this thesis.

1.2.4 Transport equations

The connection between the microscopic particle dynamics described above and the macroscopic transport behaviour is commonly expressed via transport equations. These equations aim to connect the thermodynamic forces (spatial gradients of particle density, pressure, temperature, etc) with the induced thermodynamic fluxes (particle, momentum, energy, etc). The simplest of these transport equations is the diffusive model that assumes a linear relation between them.

Diffusive model

In the diffusive model the particle density $n(x,t)$ evolution is directly related to the particle flux $\Gamma(x,t)$ and is given by the continuity equation arising from particle conservation:

$$\frac{\partial n}{\partial t} = -\frac{\partial \Gamma}{\partial x}$$

Fick's law [18] postulates that the induced flux $\Gamma(x,t)$ develops proportional to the density gradient direction and opposing to it:

$$\Gamma = -D\frac{\partial n}{\partial x}$$

where D is the diffusion coefficient. The two equations can be combined giving the classical diffusion equation else known as a Fick's second law:

$$\frac{\partial n}{\partial t} = D\frac{\partial^2 n}{\partial x^2} \tag{1.2}$$

Fickian diffusion assumes that the underlying microscopic transport processes are local (i.e. particle random movement can be statistically described by a gaussian distribution) and Markovian (i.e. the probability of future events is independent on the present or past state of the system). Diffusive models can only be used when particle steps are uncorrelated both in space and time, though they are frequently used when these conditions are not met.

Non-diffusive model

When classical diffusive models fail, the non-diffusive models are capable to describe transport and have been shown to be valuable tools for some systems. An example given by nature is the motion of sharks hunting for fishes. Within an area full of fish, sharks move approximately randomly, until they are forced to leave and cover long distances to find the next feeding location. The spatial jumps of sharks are described not by Gaussian, but by Lévy distribution with non-negligible probability of large steps (Lévy flights). Lévy distributions are characterized by long tails, which means that they are able to describe non-local effects without a single characteristic scale, the so-called scale-free effects. As this jumps are not independent of each other, the transport model must also include long-range non-Markovian temporal correlations.

The dynamics of systems that exhibit non-local and non-Markovian effects can be described by a fractional transport equation:

$$\frac{\partial n}{\partial t} = D_t^{1-\beta}\left[K\frac{\partial^\alpha n}{\partial |x|^\alpha}\right], \qquad 0<\beta<1,\ 0<\alpha<2, \tag{1.3}$$

where D_t^γ represents the fractional Riemann-Liouville operator of the order γ, K is a constant and $\partial^\alpha n/\partial|x|^\alpha$ is the Riesz fractional derivative of the order α [19].

While the random walk models are used to describe diffusive processes, their generalization - the continuous-time random walk (CTRW) models [20] are capable to describe dynamics beyond diffusive, where both the step-sizes Δx and waiting times Δt could be arbitrary distributed. Particularly, the probability density functions (pdf) of the step-sizes $p(\Delta x)$ and waiting times $\psi(\Delta t)$ should be able to account for scale-free effects with divergent moments. The generalized central limit theorem states that such distributions belong to a subfamily

of Lévy pdfs with following asymptotic behavior: $p(\Delta x) \sim \Delta x^{-(1+\alpha)}$ with $0 < \alpha < 2$ ($\Delta x \to \infty$) and $\psi(\Delta t) \sim \Delta t^{-(1+\beta)}$ with $0 < \beta < 1$ ($\Delta t \to \infty$) [21].

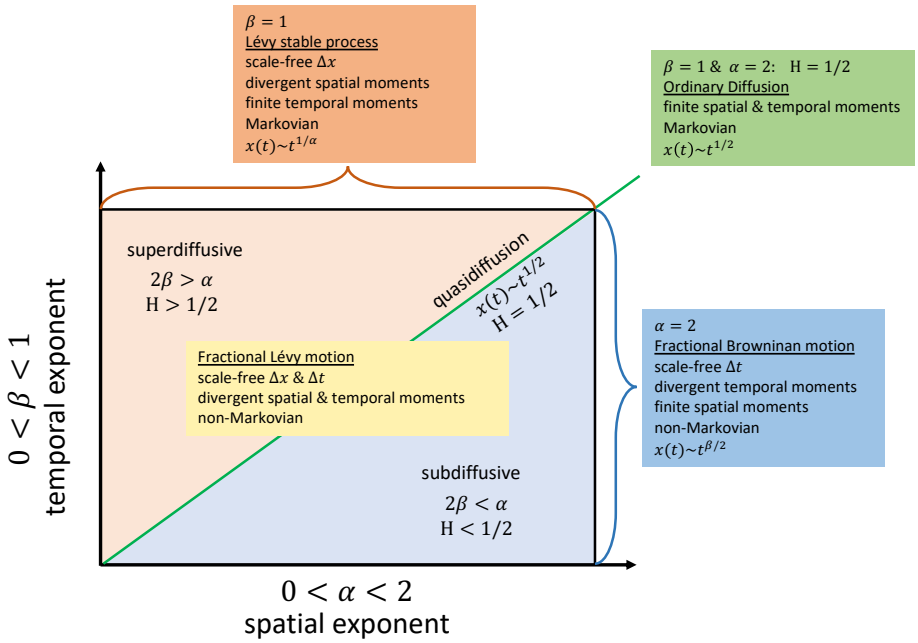

Figure 1.6: Spatial and temporal transport exponents.

The exponents α and β are known as the fractional transport exponents, describing the spatial and temporal dependences respectively. From the two exponents it is common to introduce the third one, the Hurst exponent $H \equiv \beta/\alpha$ with $0 < H < 1$.

Figure 1.6 illustrates different transport regimes and corresponding transport exponents. For arbitrary $\alpha < 2$ and $\beta < 1$ the transport is characterized as fractional Lévy motion, where usually cases with $H < 1/2$ are referred to as subdiffusive (light blue area) and $H > 1/2$ as superdiffusive (light pink area). Ordinary diffusion is recovered only when $\beta = 1$ and $\alpha = 2$ ($H = 1/2$) (see the green box), where fractional transport equation 1.3 reduces to classical diffusion equation 1.2. When $H = 1/2$ but $\alpha \neq 2$ and $\beta \neq 1$ the transport is called quasidiffusive (marked by the green line), which scales as classical diffusion but having non-Gaussian and non-Markovian distributions of spatial and temporal steps respectively. In the limiting case, when a

Lévy distributions becomes Gaussian, transport is described as Fractional Brownian motion with finite spatial moments and $\alpha = 2$ (see the blue box). The last limit is described with $\beta = 1$, the so-called Lévy stable process, which is Markovian (loss of memory) and has finite temporal moments (see the light orange box).

Non-diffusive transport in fusion

The usual procedure to quantify the particle transport involves analyzing particle losses (if present) and characterizing the corresponding transport coefficients assuming that the underlying transport is diffusive. It has been shown recently, that this traditional diffusion approach fails to adequately describe transport, mainly because the underlying processes lack characteristic temporal and/or spatial scales, and that a fractional transport description is necessary to capture such dynamics.

Examples of this are electrostatic plasma edge fluctuation measurements across fusion devices as tokamaks, stellarators and reverse field pinches, where self-similar behaviour in observed [22]. The fluctuation dynamics is shown to have long-range time correlations revealing its non-Gaussian nature and pointing out to a superdiffusive behaviour with a Hurst parameter value well above 0.5 [23, 24]. The turbulence induced transport also resembles avalanche dynamics, that is known to be governed by self-organized criticality (SOC). The typical example of avalanche-like behaviour is the way how particles could be either trapped in eddies for long time or travelled across a number of eddies in a single flight, the so-called stochastic jets, giving rise to anomalus diffusion. To investigate the turbulent transport numerically, the common approach is to follow tracer pseudo-particles. B.A. Carreras [25] demonstrated that transport in eddies induced by pressure-gradient-driven turbulence has super-diffusive character. Similarly, D. del Castillo-Negrete [26, 27] showed that tracer displacements due to eddies have superdiffusive character. He also proposed a transport model based on fractional derivatives, which reveals non-local effects in space (due to anomalously large jumps of tracers through several eddies resulting in fractional derivative operator $\beta = 0.5$ in time) and memory effects (resulting in fractional derivative operator $\alpha = 0.75$ in space), thus giving $H = 0.66$. L. Garcia [28] has extended this work to the case of toroidal geometries coming to the same conclusion and

obtaining $\alpha = 1.1$ and $\beta = 0.7$. It has been numerically established, that the unstable growths of waves in the absence of subdominant diffusive channel, such as dissipative trapped electron modes (DTEM), also lead to superdiffusive radial transport [29, 30, 31] with strongly non-Gaussian and non-Markovian character, whereas the subdominant diffusive channel has a stabilizing effect on perturbed mode leading towards *Gaussianity* and *Markovianity*.

Besides being driven by the excess of pressure, the turbulent transport particularly due to ion-temperature gradient ITG, exhibits features of Self-Organized Criticality [32]. Further simulations demonstrated that the nature of ITG driven turbulent transport in the presence of sheared zonal flows in tokamaks is non-Gaussian and exhibits subdiffusive features [33, 34, 35]. Recently, the effect of poloidal magnetic field quasi-symmetry on ITG turbulence was studied [36], revealing that as the degree of quasi-symmetry increases, the turbulent transport becomes subdiffusive. G. Sanchez Burillo and co-workers came to the same conclusion [37], when analyzing shear Alfven, drift tearing and ballooning modes for the Compass tokamak, showing nonlocal, non-Markovian and subdiffusive turbulent transport.

A number of experimental and numerical studies address the suprathermal ion transport associated with turbulence in TORPEX device, indicating that this transport has non-diffusive nature [38, 39, 40, 41, 42], which is varying from subdiffusion to superdiffusion depending on the beam energy and turbulence fluctuation amplitude, where large intermittent and persistent $E \times B$ drifts lead to superdiffusion, while their suppression results in subdiffusion.

A detailed summary of fractional transport theory and applications to fusion plasmas can be found in the review by R. Sánchez and D. Newman [43].

1.3 α-particle transport

Self-sustained burning in a future fusion reactor relies on the satisfactory confinement of α-particles, being a direct byproduct of D-T fusion reaction. α-particles must deposit their 3.5 MeV energy to the rest of the core plasma by collisions and whose unanticipated losses could cause negative effects on the power balance and the plasma-facing components. This makes a quantitative understanding of α-particle

transport crucial for a future fusion reactor.

The magnetic field of a fusion device, independently of being a tokamak or a stellarator, is not only non-uniform due to its toroidal shape, but also has corrugations, for example, caused by a finite number of field coils. Up to date, the transport of α-particles due to field corrugations in the collisionless limit was assumed to be diffusive. Recently, non-diffusive models capable to address more general transport problems were shown to be relevant for describing turbulent transport in fusion plasmas. This fact prompted us to check whether what has been done so far regarding α-particle transport is accurate or a more general approach is needed. The remainder of the chapter is devoted to the α-particle transport starting from the basic equations of motion, from which α-particle trajectories could be obtained and characterized. At the end of the chapter, a short summary on α-particle diffusion is given, and the objectives of our study are highlighted.

1.3.1 Basic equations

The collisionless motion of charged particles in magnetized plasmas consists of a streaming along the magnetic field lines and a fast gyration around it. The gyration frequency (the cyclotron frequency, $\omega = qB/m$) is so high and its radius (the Larmor radius $\rho_L = mv_\perp/qB$) is so small, compared to other plasma frequencies and spatial scale-lengths, that it is customary to use its guiding center as a reference frame for tracking particle trajectories. The new set of equations of motion do not describe the position of the particles but rather that of their guiding centers. This approximation is known as the *small gyroradius ordering*, or drift ordering and allows to split the fast/small and slow/large time/space scales. Despite of α-particles high birth energy (3.5 MeV), the guiding centre approximation can be safely applied to the study their dynamics. The typical Larmor radius value in reactor relevant conditions is $\rho_\alpha \sim 0.05$ m, which is smaller than any characteristic plasma parameter either relevant to profile scales or magnetic field corrugations perhaps except at the pedestal. The statistical kinetic description of the plasma is thus given for the distribution function of the guiding centers $f = f(t, \vec{r}, v, p)$, which evolves in time according to the drift kinetic equation (DKE) $df/dt = C(f)$ introduced by Hazeltine in 1973 [44], where $C(f)$ is the collision operator. This represents a six dimensional problem, where $\vec{r}$ is a guiding center

position in 3D space, v and p are the speed and pitch ($p = \vec{v} \cdot \vec{B}/v$) in velocity space and t is time. In this coordinates, the DKE can be written as:

$$\frac{\partial f}{\partial t} + \frac{d\vec{r}}{dt}\frac{\partial f}{\partial \vec{r}} + \frac{dp}{dt}\frac{\partial f}{\partial p} + \frac{dv}{dt}\frac{\partial f}{\partial v} = C(f) \tag{1.4}$$

where the drift speed $d\vec{r}/dt = \vec{v}_g$ contains three terms accounting for the fast streaming along the field line, the slow curvature and ∇B drifts across it and the slow $\vec{E} \times \vec{B}$ drift due to the electric field:

$$\frac{d\vec{r}}{dt} = pv\frac{\vec{B}}{B} + \frac{mv^2}{2qB^3}(1+p^2)\,\vec{B} \times \vec{\nabla} B + \frac{\vec{E} \times \vec{B}}{B^2} \tag{1.5}$$

The time derivative of the pitch $p = v_{\parallel}/v$ is given by:

$$\frac{dp}{dt} = -\frac{v}{2B^2}(1-p^2)\vec{B} \cdot \vec{\nabla} B - \frac{p}{2B^2}(1-p^2)\frac{\vec{E} \times \vec{B}}{B^2} \cdot \vec{\nabla} B \tag{1.6}$$

and the time derivative of the kinetic energy is:

$$\frac{dv}{dt} = -\frac{v}{2B}(1+p^2)\frac{\vec{E} \times \vec{B}}{B^2} \cdot \vec{\nabla} B \tag{1.7}$$

The total kinetic energy, $\mathcal{E} = mv^2/2 + q\Phi$, and magnetic field moment, $\mu = mv_{\perp}^2/2B$, are conserved and are responsible for the bouncing of some particles at regions with high magnetic fields.

It is common to consider the system to be at steady state and neglect the first term of DKE $\partial f/\partial t = 0$. Further approximations relevant for the α-particle transport are neglecting the effect of the electric field - as it would require unrealistic electric fields to make it comparable to the α-particles thermal speed $v_\alpha = 1.3 \times 10^7$ m/s. The second approximation is neglecting collisions.

Under these approximations, the motion of α-particles is described by a reduced set of guiding-center equations, where the last terms in equations 1.5 and 1.6 together with the entire equation 1.7, $dv/dt = 0$, could be neglected; i.e. α-particles are considered as collisionless and monoenergetic.

Although DKE solutions provide a complete picture of neoclassical transport processes, distribution functions are extremely difficult to calculate. A different approach to estimate particle transport is

to calculate transport relevant quantities by ensemble averaging over guiding center particle orbits using the Monte Carlo method by solving numerically the equations of motion 1.5 and 1.6. For example, it is possible to calculate the transport coefficients, the convection velocity and the diffusion coefficient, from the time dependence of the moments of the radial distribution according to the Einstein's estimates [45].

When written in Boozer coordinates [7], the equations of motion reduce to 4 ordinary differential equations [46], describing the variation of the three spatial coordinates (ψ, θ, φ) and the pitch p:

$$\begin{aligned}
\frac{d\psi}{dt} &= -\frac{\mathcal{E}(1+p^2)}{qB\gamma}\left[g\frac{\partial B}{\partial \theta} - I\frac{\partial B}{\partial \varphi}\right] \\
\frac{d\varphi}{dt} &= \frac{pvB}{\gamma}(\rho_\parallel I' + 1) - \frac{I}{\gamma}\left[\frac{\mathcal{E}(1+p^2)}{qB}\frac{\partial B}{\partial \psi}\right] \\
\frac{d\theta}{dt} &= -\frac{pvB}{\gamma}(\rho_\parallel g' - \iota) + \frac{g}{\gamma}\left[\frac{\mathcal{E}(1+p^2)B}{q}\frac{\partial B}{\partial \psi}\right] \\
\frac{dp}{dt} &= \frac{(1-p^2)v}{2\gamma}\left[(\rho_\parallel g' - \iota)\frac{\partial B}{\partial \theta} - (\rho_\parallel I' + 1)\frac{\partial B}{\partial \varphi}\right]
\end{aligned}$$

where $2\pi\psi$ is the toroidal magnetic flux, θ and φ are the periodic poloidal and toroidal angles, g is the poloidal current outside a flux surface, I is the toroidal current within a flux surface, ι is the rotational transform, $\gamma = g(\rho_\parallel I' + 1) - I(\rho_\parallel g' - \iota)$, the prime denotes radial derivative and $\rho_\parallel = mvp/qB$.

These equations depend only on the magnetic field strength B and its derivatives with respect to the three spatial coordinates. The solution of this set of equations, which is only possible to obtain numerically, provides an accurate description of the α-particles guiding center trajectories, that will be used through the rest of this work.

1.3.2 Particle classification

α-particle trajectories can be classified into two categories as trapped or passing according to whether they change, or not, their direction of motion, i.e. the sign of their pitch angle is manteined or not, see Figure 1.4. The toroidal movement of trapped particles is limited by the fact that when streaming along the field lines, which are twisted because of the rotational transform, they cannot go to the inside part of

the torus in their poloidal movement, and are bouncing back toroidally. The reason why they cannot enter regions with higher magnetic field magnitude is the conservation of energy and magnetic moment. The resulting orbits are called banana orbits and are due to the different radial particle drifts, which they follow when moving along and against the direction of the magnetic field. A particle trajectory following a banana orbit is reflected twice and does not encircle the magnetic axis of the device. A common approach to characterize banana orbits is with their bouncing time τ and orbit width Δw, respectively. The bounce time is the time it takes a particle to bounce between two consecutive reflection points, being the orbit width its radial extension.

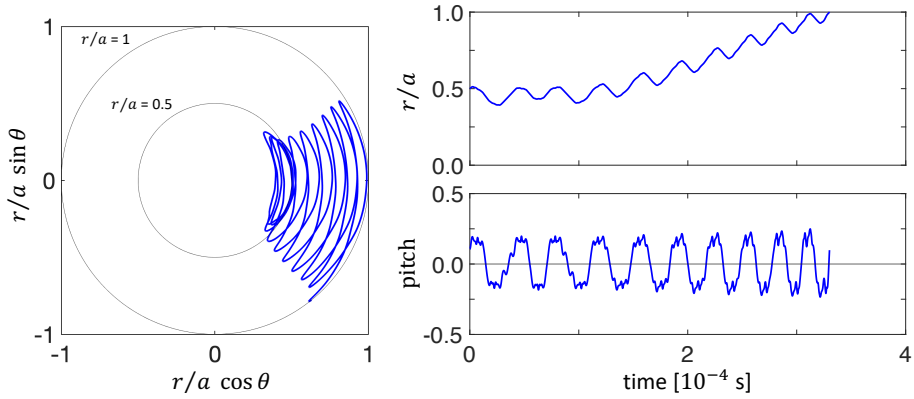

Figure 1.7: Left: poloidal projection of a trapped α-particle trajectory following banana orbits in Boozer coordinates from its initial position at $r/a = 0.5$ till its lost at r/a =1. Right: time evolution of the radial position r/a (top) and pitch (bottom) of the same trajectory.

In a non-uniform magnetic field, α-particles are affected by field corrugations, which are typically caused by the discrete number of coils, as in tokamaks, or by the discrete number of coils and other helical ripples, as in stellarators. The field inhomogeneities are of primary concern for trapped particles. Contrary to passing particles, that always circulate in the same direction, trapped particles change the sign of their pitch at the bouncing points, whose position is strongly affected by the inhomogeneities of the magnetic field. Figure 1.7 illustrates an example of a trapped α-particle trajectory in a quasi-toroidally symmetric stellarator, which follows banana orbits and experiences severe drifts leading to its loss due to the magnetic

field corrugations.

In addition to banana-type orbits, the inhomogeneities of the magnetic field also give rise to a variety of trapped particle orbits [47]. Examples of such orbits are given in Figure 1.8 for a non-uniform magnetic field of a quasi-toroidally symmetric stellarator. The orbit of a trapped particle is called *potato* (magenta/solid line) if it encircles the magnetic axis. Another type is the orbits that change from being trapped to passing and vice versa and that are called *transition* orbits (cyan/dashed line). The ripple trapped orbits (red/dotted line) differ from the other two types in that they neither encircle the axis nor necessarily cross the equatorial plane in between reflection points. From these orbits, ripple trapped orbits are the most harmful for confinement, as they are 'doomed' to be lost, unless collisions send them to more favorable regions in phase space.

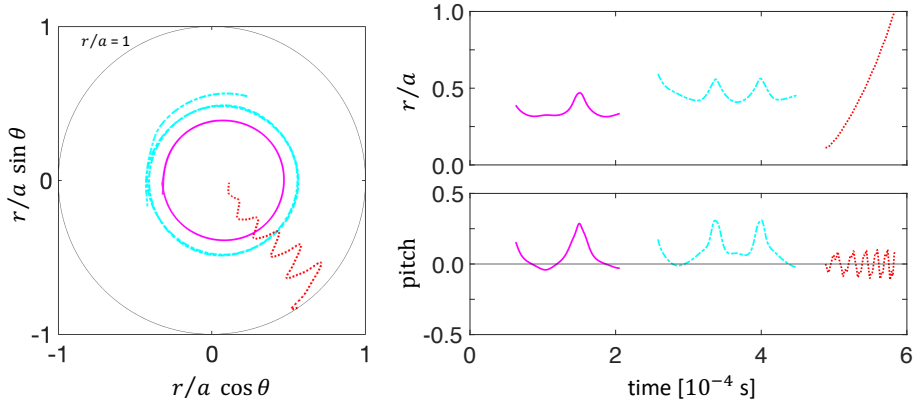

Figure 1.8: Left: poloidal projection of α-particle trapped orbits, where magenta/solid is a potato orbit, cyan/dashed is a transition orbit and red/dotted is a ripple trapped orbit in Boozer coordinates. Right: time evolution of the radial position r/a (top) and pitch (bottom) of the same orbits.

Characteristics of banana orbits: τ and Δw

The two usual quantities used to characterize banana orbits are its bouncing τ time and normalized width Δw. There is an extensive literature devoted to their analytical estimation for tokamaks [16, 48, 49, 50], that vary across authors up to a numerical coefficient. The

expressions for the bouncing time and normalized orbit width are $\tau \approx R/\iota\sqrt{\epsilon}v_\alpha$ and $\Delta w \approx \rho_\alpha/\iota\sqrt{\epsilon}a$, where R and a are the major and minor plasma radii, $\epsilon = a/R$ is the inverse aspect ratio, ι is the rotational transform and ρ_α and v_α are the α-particles Larmor radius and thermal speed. Although several alternatives were obtained for peculiar particle behavior or conditions [51, 52, 53].

Less is known about characteristic scales of motion for trapped particles in stellarators and it is not clear to what extent they differ from tokamaks. For trapped α-particles, Nagornyj and Yavorskij [54] found that the formula for the bouncing time in a stellarator resemble the one for a typical tokamak up to a coefficient. A similar conclusion was reached for common trapped particles in the collisionless $1/\nu$ regime, see Figure 1.5, when Wakatani [55] in 1998 calculated the bouncing time according to a dominant field component (the helical component and its modulation) for a heliotron with multiple helicity. Finite orbit width effects in stellarator geometry has also been studied numerically by Rome in 1995 [56], who suggested that the banana width of a helically trapped particle should be inversely proportional to the number of periods of a stellarator, which makes it smaller compared to a tokamak with identical conditions.

Research on this subject has been mostly restricted to analytical estimations, with the exception of a few numerical studies [47, 56, 57, 58]. The orbit parameters have been estimated solely relying on the main magnetic field components, excluding the rest of the spectrum. The dependence of the bouncing time and the orbit width on the number of modes used in the description of the magnetic field is an open question, which will be discussed in the next section.

1.3.3 α-particles diffusion

The only possible source of diffusion in the collisionless α-particle dynamics is the separation of particle trajectories from their birth flux surfaces, i.e. the particle drifts. Pure magnetic field symmetries guarantee zero average radial particle drifts, while in a case of symmetry breaking the drifts are unavoidable. This gives a motivation to study the effect of breaking these symmetries on α-particle trajectories and to test whether the transport dynamics can still be described using a diffusive description.

A collisionless scenario in which particles drift straight out of the

plasma cannot be described as being diffusive, but corresponds to convection [59]. The precession of the banana tip due to presence of field ripples is known as stochastic diffusion or GWB diffusion, named after Goldston, White and Boozer [60]. In this work, the stochasticity threshold was considered in the approximation of zero banana orbit width in a simplified geometry. The GWB stochastic diffusion mechanism was extended to consider non-circular cross-section [61, 62, 63] and banana orbit widths effects [64], giving diffusion coefficients in the range of $5 - 25\ m^2/s$ [61, 65, 63, 66]. The diffusion coefficient was calculated as $D \sim d^2/\tau_b$, where d is the shift of the banana tip near the turning point in the radial direction and τ_b is the bouncing time. These theoretical estimations were compared with fast particle experimental results for JET [66, 64, 67] and TFTR [68, 69, 70], where the stochasticity threshold due to the precession of the banana tip turned out to be $1 - 3$ times the threshold specified by the GWB diffusion model, and the experimental losses are approximately twice larger than those theoretically predicted.

Because of ripples, new types of trapped particles orbits arise - the so-called ripple trapped or super-bananas, which are locally trapped between coils. The transport and losses of such orbits were analytically described [59, 71] and numerically evaluated [72] as being convective.

However, there is a possibility of transitions between different types of trapped particle orbits that lead to either convective or diffusive drifts. The conditions for this were described in [73] and [74]. In 1993, Yushmanov [75] analytically described both convective and diffusive losses in up-down asymmetric tokamaks, while in 1997, Isobe [76] demonstrated it experimentally on JT-60U for NBI injected fast particles, indicating that the up-down asymmetry causes radial diffusion of banana orbits in addition to ripple diffusion, but without increasing fast ion losses.

In addition to transitions between types of trapped particle trajectories, the transitions can occur between trapped and passing particles and vice versa, as was demonstrated in [77] and [78]. This stochastic transition is more common for stellarators, where the spectrum of magnetic field modes is broader and there are more types of trapped particles [79, 80]. The theory behind this process along with numerical simulations was summarized in a monograph by Beidler and coworkers in 2001 [81]. Transition effects are claimed to be the main cause for fast particle losses in Wendelstein 7-X line devices. The dif-

fusion coefficient for the transition from trapped to passing particles and vice versa, defined as $D =< \Delta r^2 > /\tau$, could reach 100 m^2/s, where the numerator is the change in a radial coordinate caused by orbit transformation, and the denominator is an average between the trapping and passing times $\tau = (\tau_{trapped} + \tau_{passing})/2$. The possibility of improving the transition particles confinement by radial electric field was studied in [82, 83], while the curing effect of transition particles on plasma stability is discussed in [84].

Moreover, in stellarator geometry, there is a wide variety of trapped orbits, for example, helically trapped, which are typical for devices such as LHD [85, 86, 87] and W7-X [88], which lead to even higher possibilities of transitions between orbits. It is shown that the high order Fourier harmonics strongly affect their motion, precluding any analytical treatment. Recent studies evaluate the level of trapped α-particle loss in reactor-scale devices as unacceptable [89, 90], thus the study of their transport is paramount.

1.4 Objectives and outline

Future fusion reactors must confine α-particles to sustain burning plasma conditions until they share their 3.5 MeV energy with the bulk plasma particles (thermalized) and to prevent damage of plasma-facing components. As being charged particles, α-particles are controlled by the magnetic field, whose structure is intrinsically non-uniform because of its toroidal shape, i.e there are zones of high and low field that divide α-particles into two types either passing or trapped. The latter is highly susceptible to the magnetic field inhomogeneities (that would unavoidably present in any realistic fusion device), which primary alter the positions of their reflection points [60] and might shuffle the trapped orbits types [47]. The transport induced by non-zero radial average drifts of trapped α-particle is usually referred to as ripple-enhanced transport [66]. One of the strategies to reduce this transport is to optimize the magnetic field by imposing an approximate field symmetry [12, 13, 14, 15]. While the mitigation of α-particles losses caused by field corrugations for future fusion reactors was widely addressed in the literature [81, 91, 92, 93, 90], an understanding of the underlying dynamics and methods for transport evaluation are still scarce or controversial.

The classical approach to the transport of fast particles includes the calculation of particle losses and the estimation of transport coefficients. As shown in this Chapter, the ripple-enhanced transport of trapped α-particles has been modelled as being convective/diffusive [59, 60, 79, 80, 81]. The convection and diffusion transport coefficients are commonly estimated based on the characteristic trapped orbit parameters, i.e. bouncing times and orbit widths, whose analytical expressions are developed only based on the dominant magnetic field component and are mainly relevant for tokamaks [49, 50, 54], and where the numerical estimations are scarce. This casts doubt on their validity. In addition, the recent success of fractional transport models for evaluating turbulent transport in fusion plasmas [43] has inspired us to reconsider the classic *Ficksian* diffusive approach to transport [21].

This thesis aims at estimating the transport coefficients, classical or fractional, of ripple-enhanced α-particle transport. Bearing this in mind, we statistically characterize the collisionless behavior of a large ensemble of α-particles typifying the transport in reactor-scale devices. This was done numerically simulating their collisionless guiding center motion with the Monte Carlo code MOCA [94] using the drift ordering approximation and neglecting electric field effects, that allows to consider α-particles as monoenergetic. Throughout this work five magnetic configurations endowed with toroidal symmetry and scaled to reactor size were considered: a perfectly symmetric ITER-like tokamak [95] and a quasi-toroidally symmetric stellarator [12] with different levels of toroidal symmetry.

The main body of the thesis consists of two parts. Chapter 2 statistically describes α-particle transport, where the following questions were addressed: how the magnetic configuration and the initial conditions impact the particle losses? which types of particles and particle orbits contribute to the losses and in what percentages? how does symmetry breaking affect the characteristic parameters of these orbits? which type of transport dynamics is driving them? Since the results of the latter cast doubt on the validity of the diffusion approach to adequately describe α-particle transport, the study was expanded to test non-diffusive models in the next chapter.

Chapter 3 examines the underlying nature of the ripple-enhanced transport of the trapped α-particles by means of fractional transport theory. The fractional transport coefficients, i.e. the Hurst H, the spatial α and the temporal β exponents, were estimated by apply-

ing Lagrangian and Eulerian techniques commonly used for modelling turbulent transport [96, 26, 30]. The purpose of the Chapter 3 is to try to answer the following questions: how does the departure from quasi-toroidal symmetry affect the nature of the trapped α-particle transport? how does a change in confinement in these configurations, caused by a gradual decrease in quasi-toroidal symmetry level, affect the fractional transport coefficients?

Chapter 2

Statistical description of collisionless α-particle transport

The content of this chapter was published in **Nuclear Fusion** by A. Gogoleva, V. Tribaldos, J.M. Reynolds-Barredo and C.D. Beidler under the name "*Statistical description of Collisionless α-particle transport in cases of broken symmetry: from ITER to quasi-toroidally symmetric stellarators*". It is reproduced here with the permission of the copyright owner *Institute of Physics (IOP)*. For the consistency with the rest of the manuscript, the typography has been adapted and only small changes in notation have been made. This is an author-created, un-copyedited version of an article accepted for publication in Nuclear Fusion. Neither the IAEA nor IOP Publishing Ltd is responsible for any errors or omissions in this version of the manuscript and/or any version derived from it. The Version of Record is available online at https://doi.org/10.1088/1741-4326/ab7936.

The goal of the study presented in this chapter is to develop a universal method, capable to address the collisionless α-particle confinement for arbitrary fusion reactor magnetic fields. The present work focuses on the statistical characterization of trapped α-particles motion throughout the toroidal symmetry breaking: from an ideal tokamak to a quasi-toroidally symmetric stellarator. The characteristic parameters of trapped α-particles cast doubt on the validity of the classical diffusion model for describing collisionless ripple-enhanced transport.

Abstract

The confinement of α-particles is vital for any future fusion reactor. Unfortunately, the inevitable appearance of inhomogeneities in the magnetic field activates the non-collisional transport by virtue of ripple trapping and ripple induced stochastization. While a large and growing body of literature is devoted to the mitigation of these channels of losses for future reactor designs, far too little attention has been paid to characterize the statistical nature of the underlying stochastic process, which is generally assumed to be diffusive. Here the effect of breaking the toroidal symmetry on collisionless α-particle transport is analyzed numerically with a guiding center orbit following code MOCA for several configurations: a perfectly toroidally symmetric ITER-like tokamak and four stellarators with different levels of quasi-toroidal symmetry. Statistical characterization of banana widths, bouncing times and banana center evolution put into question the classical convection/diffusion approach to adequately describe collisionless α-particle transport as the magnetic configuration departs from toroidal symmetry.

Keywords: α-particle transport, ITER, quasi-toroidal stellarator

2.1 Introduction

The success of magnetically controlled thermonuclear fusion relies, among other things, on the confinement of α-particles that are not only essential for sustaining fusion conditions, but whose unanticipated losses could compromise the efficiency and, more importantly, put at risk the plasma-facing components. The confinement of α-particles is a complex subject involving the equilibrium magnetic field, plasma and α-particle birth profiles, accompanied by resonant and non-resonant MHD instabilities, turbulence, etc. [66, 97, 98, 99].

Improved particle confinement of reasonably high energetic particles could be achieved by endowing the magnetic field either with a certain type of symmetry, with isodynamicity, which imposes the cross-field drift to vanish at every point, or with the less stringent omnigeneity, that ensures zero time-averaged radial drifts [100, 9, 11]. While for particles that circulate in the plasma with the same direc-

tion of motion the absence of net radial drifts is fulfilled *per se*, for trapped or reflected particles that bounce between the reflection points placed at zones of higher field strength rather than being automatic becomes the optimization goal. In any realistic device, due to field corrugations (caused by the discrete number of coils, as in tokamaks and stellarators or by various ripples, as in stellarators) some of these particles are lost. Two main collisionless mechanisms are described relating reflected particle losses with the inhomogeneities of the confining magnetic field: ripple trapping [59], in which particles falling into local ripples result in super-bananas orbits, and ripple induced stochastic processes that make particles change their orbit type close to the bouncing points [60, 65, 81]. While a body of literature was devoted to the mitigation of these losses for future reactor designs [81, 91, 92, 93, 90], not so much attention has been paid to characterize the statistical nature of the stochastic process, which is generally assumed to be *diffusive* [66, 97, 98, 99, 59, 60, 65, 81].

The goal of this work is to study the effect of breaking the toroidal symmetry on the confinement of collisionless trapped α-particles. To this end, several configurations are examined, starting with an ideal, perfectly toroidally symmetric, ITER configuration that will serve as a reference followed by four stellarator configurations with different levels of quasi-toroidal symmetry. The statistical characterization of trapped particle behavior is done numerically with the guiding center orbit following code MOCA [94] supplemented with other techniques to determine trapped particle parameters such as their bouncing times, orbit widths and the radial movement of those orbits. Probability density functions of these basic parameters were obtained as a function of the level of toroidal symmetry. These results are compared with analytical calculations as well as with some newly developed estimations assuming that particles approximately move along the field lines. The *diffusive* nature of the stochastic transport process is examined with different statistical analyses for the five magnetic configurations.

The remainder of the paper is organized as follows. In Section 2.2 the basic approximations, the guiding center orbit following code and the magnetic configurations are presented along with a new figure of merit to quantify the degree of quasi-toroidal symmetry. Then the impact of the magnetic configurations together with the initial conditions on the orbit types and the fraction of confined and lost reflected particles are discussed. A new technique is presented at the end of

Section 2.2 allowing to obtain banana centers, widths and bouncing times from particle trajectories the results of which are summarized in Section 2.3. The fraction of reflected particles and the most probable banana bouncing times obtained from particle trajectories are compared with bounce averaging estimations along field lines, an approximation that is justified based on a new method for calculating connection lengths for arbitrary magnetic configurations. The end of Section 2.3 is devoted to examine if the statistical properties of α-particle transport agree with the diffusive paradigm. Finally, Section 2.4 summarizes the results and presents a brief discussion.

2.2 Configurations and Methods

In trying to establish the basic relation between the confinement of α-particles and the symmetry of the underlying magnetic field three main approximations were made through this work, namely: i) the *small gyroradius ordering*, or drift ordering, ii) neglecting the effect of the electric field and iii) ignoring the collisions with other particle species. The small gyroradius approximation requires $\rho_\alpha/L \sim \omega/\omega_c \sim V_E/v_\alpha << 1$, where ρ_α is the α-particle Larmor radius, L a characteristic plasma spatial scale length (either relevant to profile scales, magnetic field corrugations or banana orbit widths), ω is a characteristic frequency (circulating or bounce α-particles frequency), ω_c is the cyclotron frequency and V_E and v_α are the $\vec{E} \times \vec{B}$ drift and α-particle speeds respectively. Anticipating some of the results of next sections, it is possible to justify that these conditions are fulfilled for α-particles in reactor relevant plasmas. The value of $\rho_\alpha \approx 5$ cm has to be compared with the spatial scales of the orbit widths, $L \sim 0.1 - 0.2\,a \sim 0.3 - 0.6$ m (see Figure 2.7 left), the magnetic field corrugations $L \sim 1$ m (see Figure 2.9) and is reasonably valid except perhaps in the pedestal region. The characteristic circulating $\tau_c \sim 2\pi R/v_\alpha \sim 3-10\mu$s, bouncing $\tau \sim 10 - 25\mu$s (Figure 2.7 right) and collisional slowing-down times $\tau_{slow} \sim 1$ s are also much slower than the cyclotron time. The disparity between v_α and $V_E = \vec{E}\times\vec{B}/B^2$ also justifies neglecting the effect of the radial electric field. A rough estimation of the electric field required for the $V_E \sim E_r/B$ to be comparable with the guiding center drift speed $V_d = mv^2(1+p^2)\vec{B} \times \nabla B/2qB^3 \sim \mathcal{E}_k/qBL$ implies an unrealistically large $E_r \sim \mathcal{E}_k/qL \sim 3.5 \times 10^6/L \sim 10^6 - 10^7$ V/m. Neglecting

collisions requires some explanation because despite their initial high speed, α-particles eventually thermalize with the bulk plasma. In reactor conditions α-particle collisional slowing-down time, $\tau_{slow} \sim 1$ s, is faster than the collisional scattering time, $\tau_{scatt} \sim 5$ s [66, 101]. Therefore, depending on the time scales of α-particle confinement it may or may not be justified to include or neglect collisions. Here, to establish a clearer relationship between α-particle confinement and the level of symmetry of the magnetic configuration collisions will be neglected throughout this work.

2.2.1 Equations of motion

Under these approximations, the motion of α-particles is described by a reduced set of guiding-center equations. One for the velocity of the guiding center,

$$\vec{v}_g = pv\frac{\vec{B}}{B} + \frac{mv^2}{2qB^3}(1+p^2)\,\vec{B}\times\vec{\nabla}B \tag{2.1}$$

where the two terms account for the fast streaming along the field line and the slow curvature and ∇B drifts across it. The other equation accounts for the variation of the pitch $p = v_{\|}/v$

$$\frac{dp}{dt} = -\frac{v}{2B^2}(1-p^2)\vec{B}\cdot\vec{\nabla}B \tag{2.2}$$

that arises from the conservation of kinetic energy, $\mathcal{E} = mv^2/2$, and magnetic field moment, $\mu = mv_{\perp}^2/2B$, which is responsible for the bouncing of some particles at regions with high magnetic fields. Note that neglecting the radial electric field effect and the collisions eliminates the need of an equation for the evolution of the α-particles speed, which is conserved.

When written in Boozer coordinates [7], the equations of motion reduce to 4 ordinary differential equations depending only on the magnetic field strength B and its derivatives with respect to the spatial coordinates (ψ, θ, φ). Where ψ is a normalized toroidal magnetic flux and θ and φ are the poloidal and toroidal angles respectively.

2.2.2 Configurations

From the infinite number of possible three-dimensional magnetic configurations, two strategies lead to improved particle confinement by endowing the magnetic field either with a certain type of symmetry or with isodynamicity. Here the study will be focused on the effect of breaking the toroidal symmetry of the magnetic field (the most common symmetry). Five configurations will be considered: a purely toroidally symmetry ideal tokamak, that will be used as a reference case, and four stellarators with different levels of quasi-toroidal symmetry (QTS).

For the toroidally symmetric configuration the natural decision was to consider a *ripple-less* ITER [95] tokamak with the following parameters: $B \sim 5.3$ T, $a = 2.67$ m , $R = 6.2$ m and $V \sim 900$ m^3. The four quasi-toroidally symmetric configurations are loosely based on the NCSX [12, 14] stellarator scaled up to have the same ITER nominal magnetic field and volume, which results in a minor and major radius of $a = 2.15$ m and $R = 9.8$ m respectively.

The detailed structure of the magnetic field has been obtained solving the three-dimensional ideal magnetohydrodynamic (MHD) equations with the VMEC code [102]. VMEC finds three-dimensional equilibrium solutions through a variational procedure that minimizes an energy functional with a spectral/finite differences method. VMEC provides the shapes of a given set of nested flux surfaces and the corresponding magnetic field B as a Fourier series constructed in its own internal flux coordinates with a double periodicity in the poloidal and toroidal angles. The VMEC output is transformed to Boozer flux coordinates (ψ, θ, φ), where the general expression for the magnetic field is also given as a Fourier series for each flux surface:

$$B^{\psi}(\varphi,\theta)/B_0 = 1 + \sum_{n=1}^{\infty}\left({}^{c}B^{\psi}_{0n}\cos(nN_p\varphi) - {}^{s}B^{\psi}_{0n}\sin(nN_p\varphi)\right)$$
$$+\sum_{m=1}^{\infty}\sum_{n=-\infty}^{\infty}\left({}^{c}B^{\psi}_{mn}\cos(m\theta - nN_p\varphi) + {}^{s}B^{\psi}_{mn}\sin(m\theta - nN_p\varphi)\right) \quad (2.3)$$

where N_p is the number of periods of the configuration, $\psi = (r/a)^2$ the normalized toroidal flux, r being the flux surface radius and a the minor radius.

The description of the magnetic field for ITER requires both sine and cosine terms because its D-shape cross-section is not up-and-down symmetric. The expansion for the stellarator only contains cosine terms due to the stellarator symmetry. Despite the full Fourier series has more than 1000 harmonics for each magnetic surface, not all of them are relevant to accurately describe α-particle transport. Here, only modes above a threshold of $|^cB^{\psi}_{mn}|$ or $|^sB^{\psi}_{mn}| > 10^{-4}$ were considered for ITER, which results in including just 7 modes of the expansion (all of them being of the form B^{ψ}_{m0}). The four quasi-toroidal configurations were generated from the same stellarator equilibrium keeping fixed the few largest modes and adding on top different number of smaller harmonics by setting four thresholds. This method is different to what is done in [103], where configuration's long mean free path transport is modified through the main modes in the quasi-isodynamic stellarator W7-X. The one with higher quasi-toroidal symmetry, called QTS4 throughout this work, was obtained with a larger threshold of $|^cB^{\psi}_{mn}| > 10^{-2}$ and comprises just four $^cB_{mn}$ modes; three with $n = 0$ and the smallest one with $n = N_p$, which is responsible for the small toroidal-symmetry breaking. Setting the thresholds to $|^cB^{\psi}_{mn}| > 1/150$ and $1/180$ results in configurations QTS5 and QTS6, described with five and six modes respectively. Finally, the configuration QTS72 is obtained using the same threshold as for ITER ($|^cB^{\psi}_{mn}| > 10^{-4}$) which results in a much broader magnetic field spectrum with seventy-two modes. The ultimate reason for considering these four configurations will become clear in next sections, for the moment it suffices to say that they describe different degrees of departure from quasi-toroidal symmetry. QTS72 configuration looks much more like the configuration one can get with a set of real coils and is further away from the toroidal symmetry. To quantify the degree of quasi-toroidal symmetry of these configurations we followed Alcuson and coworkers and define a figure of merit, σ_{qt}, in a similar way to the one they used for the degree of quasi-poloidal symmetry [36], extending the sums just to the Fourier modes larger than the threshold:

$$\sigma_{qt}(\psi) = \frac{\sum_{m=1}^{M} |B^{\psi}_{m0}|}{\sum_{n=1}^{N} |B^{\psi}_{0n}| + \sum_{m=1}^{M} \sum_{n=-N}^{N} |B^{\psi}_{mn}|} \leq 1 \qquad (2.4)$$

where σ_{qt}=1 stands for perfect quasi-toroidal symmetry, as in a tokamak. Table 2.1 lists σ_{qt} for the five configurations and three radial

positions.

Table 2.1: Values of the quasi-toroidal symmetry ratio σ_{qt} for ITER and the four quasi-toroidal stellarators as a function of radial coordinate.

r/a	ITER	QTS4	QTS5	QTS6	QTS72
0.1	1	0.97	0.96	0.86	0.70
0.5	1	0.94	0.93	0.85	0.62
0.9	1	0.89	0.86	0.83	0.56

According to the guiding center equations of motion in Boozer coordinates, the radial speed is determined by the variation of the magnetic field with the poloidal and toroidal angles, which for toroidally symmetric and quasi-symmetric configurations approximately reduces to just the poloidal dependence $\partial B/\partial\theta$. The poloidal dependence of the normalized magnetic field, B/B_0, along the field line passing through $\theta = \varphi = 0$ over two poloidal turns around the torus is shown in Figure 2.1 for three radial positions $r/a = 0.1$, 0.5 and 0.9 of some of the configurations under study. All three configurations display the basic variation due to toroidicity with lower/higher magnetic fields at the outboard/inboard of the equatorial plane and with magnetic field excursions increasing from the axis to the last closed flux surface. The larger poloidal ripple of ITER, due to its tighter aspect ratio, results in larger radial speeds than for the stellarators. However, faster radial drifts do not necessarily mean poorer confinement since particle transport depends on radial speed averages. Here is where the ideal symmetry, $\sigma_{qt} = 1$, comes into play guaranteeing that radial drifts are averaged out. Unfortunately, when the symmetry is broken, $\sigma_{qt} < 1$, there are no such conservation laws that assure the confinement nor guidelines to establish a relation between the level of quasi-symmetry and the average radial drifts. The actual transport of charged particles is the result of ensemble averaging over all possible particle trajectories subjected to all possible realistic physical processes. To show the relation between the magnetic configuration and the confinement in the clearest possible way collisions were not included in this work. Given the number of modes needed to describe the magnetic field, this could only be achieved numerically.

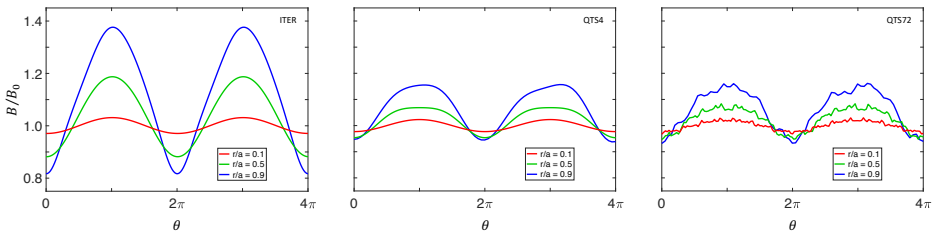

Figure 2.1: Normalized magnetic field strength along the field line passing through $\theta = \varphi = 0$ as a function of poloidal angle θ for three radial positions $r/a = 0.1$, 0.5 and 0.9 at ITER (left) and the quasi-toroidal stellarators QTS4 and QTS72.

2.2.3 Numerical Method

The transport properties of the five magnetic configurations are estimated by ensemble averaging α-particle trajectories, that in turn fully depend on the initial conditions in the absence of collisions. An efficient way to calculate guiding center trajectories consists in solving the equations of motion in Boozer coordinates. This was done with the Monte Carlo code MOCA [94]. This code has been thoroughly and successfully benchmarked [104] for an extensive range of stellarator configurations in the past. MOCA is a parallel Fortran code, in which, to speed up the calculations, the magnetic field and its derivatives are pre-stored in a 3D grid $N_\psi \times N_\theta \times N_\varphi$. The high speed of the α-particles, with $v_\alpha = 1.3 \times 10^7$ m/s, and the characteristic spatial magnetic field variation require a short integration time step, $\Delta t \approx 10^{-8}$ s, and a fine grid containing $\sim 100 \times 360 \times 360$ cells per period for numerical accuracy. The computational domain is bounded from one side by the magnetic axis and from the other by the last closed flux surface (particles which cross it are considered lost). A pseudo-Cartesian coordinate system [105] is used to overcome the numerical singularity in the vicinity of the magnetic axis. To describe the initial conditions for the monoenergetic α-particles, it is sufficient to specify their spatial positions and pitch $(\psi_0, \theta_0, \varphi_0, p_0)$.

To obtain statistically significant ensamble averages, the initial conditions have to be representative of the α-particle birth profiles under reactor conditions. Assuming that deuterium and tritium density and temperature profiles are constant on flux surfaces (at least to first order), all particles are initialized radially at half radius, around

the mean α-particle birth radius [106], and uniformly distributed over the flux surface. To account for the non homogeneous volume element associated with curvilinear coordinates, particles are initialized uniformly in pitch and randomly in the toroidal and poloidal Boozer angles with a distribution inversely proportional to the Jacobian of the transformation $1/J(\psi,\theta,\varphi) = (B(\psi,\theta,\varphi)/B_0)^2$, thus starting more particles in regions of higher magnetic field strength. Here, the Rejection Method[107] has been used to generate a random sequence in the poloidal (ITER) and poloidal-toroidal (QTS) domains with the prescribed $1/J$ distribution function. The results for ITER were obtained using a set of 65536 particles distributed over 256 poloidal angles with 256 pitch values each, while for the stellarators 262144 particles were used with 4096 initial poloidal-toroidal angles with, again, 64 pitch values each. The simulation time is of the same order of the slowing-down time, which for α-particles in reactor conditions ranges between 0.1-1 s.

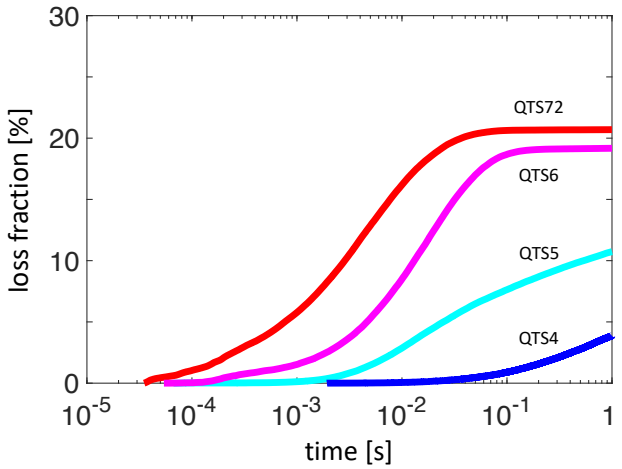

Figure 2.2: Loss fraction of α-particles over time for the four quasi-toroidal stellarators.

Finally, it is worth noting that all the results in this work were checked to be independent of the grid size, the grid interpolation scheme, the integration time step and the number of particles used. Furthermore, the relative energy conservation error has been checked to be below $\sim 10^{-5}\%$ for all particles throughout their lifetimes.

2.2.4 Impact of the magnetic configuration and the initial conditions on the losses

As a first test of the numerical procedure a set of 65536 α-particles, initially at $r/a = 0.5$ and distributed in poloidal angle and pitch, is followed for 1 s in the idealized and perfectly toroidally symmetric ITER configuration finding that, as expected, none of them get lost. Within this set, there are particles circulating the full plasma with fixed direction of motion, never changing the sign of their pitch and which stayed perfectly confined, the so-called *passing particles* (71%, see Table 2.2). The other 29% do change the sign of their pitch and are bounded to stay in plasma regions with low magnetic fields, that is why they are called *trapped or reflected particles* and which follow trajectories whose poloidal projection resembles a banana, the so-called *banana orbits*. The fractions of passing and reflected particles presented in Table 2.2 should not be confused with the effective circulating and trapped particle fractions appearing in neoclassical theory [108, 109, 110] in connection with the dynamics parallel to the magnetic field. In ITER both types have zero average radial drifts, passing particles have it *per se* and reflected particles have it because perfect toroidal symmetry grants well behaved banana orbits. In more realistic ripple tokamaks and quasi-toroidal stellarators trapped particles are expected to experience drifts and precession. This simple picture can easily get blurred when one considers magnetic configurations without symmetry in which new magnetic field ripples give rise to new families of trapped particles with net radial drifts, and even particles that can transit between being passing and being trapped, the so-called *transition particles*. Needless to say, that, even for purely symmetric fields, collisions with background bulk particles may transform passing into trapped particles and vice versa and, moreover, contribute to the net transport by interrupting zero radial average drift orbits.

The next step was to repeat the same calculations for the other quasi-symmetric configurations, but now distributing particles in the poloidal and toroidal directions and in pitch ($64 \times 64 \times 64$). We found that despite having a larger fraction of passing particles, $\sim 10\%$ more than ITER (notice the larger ripples in Figure 2.1), some of the reflected particles get lost. The detailed fractions are given in Table 2.2. Despite all stellarator configurations have roughly the same fraction

Table 2.2: Classification and percentage of α-particle types for particles starting at $r/a = 0.5$ for ITER and the four quasi-symmetric stellarators. The simulation time is 1 s.

	Passing	Reflected	
	Confined	Confined	Lost
ITER	71%	29%	0%
QTS4	81%	15%	4%
QTS5	80%	9%	11%
QTS6	79%	2%	19%
QTS72	79%	1%	20%

of reflected particles, their losses vary from a 4% for QTS4 to a 20% for QTS72. In the absence of collisions, the fate of α-particles only depends on the underlying magnetic field and the initial conditions. Moreover, all lost particles are trapped but not all trapped particles are lost. Figure 2.2 shows the cumulative loss fraction of α-particles up to $1s$ for the four stellarator configurations. As expected, the higher the symmetry the longer it takes particles to start leaving, the lower the loss rate, the longer it takes to saturate and the smaller the loss fraction.

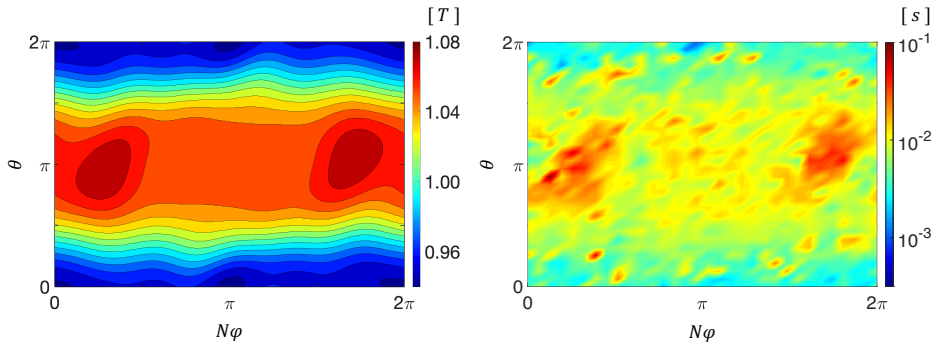

Figure 2.3: Left: Contours of constant magnetic field strength for one field period. Right: Contours of pitch averaged escaping times as a function of the initial poloidal, θ, and toroidal, φ, positions. Both plots correspond to $r/a = 0.5$ and one period of the QTS72 configuration.

To better understand the relation between α-particle confinement,

the magnetic configuration and the initial conditions in the absence of collisions, Figure 2.3 (left) shows the contour levels of the magnetic field magnitude at half radius for the QTS72 configuration. The mild toroidal dependence seen is a signature of the approximate toroidal symmetry, where the magnetic field is higher in the inboard ($\theta \sim \pi$) and lower in the outboard ($\theta \sim 0$) sides. The pitch averaged escaping times, calculated with a set of 262144 particles distributed over toroidal, poloidal angles and in pitch, see Figure 2.3 (right), confirm the weak toroidal dependence and show higher confinement times for particles born in regions of higher magnetic field. Vice versa, particles born in regions with lower magnetic field strength have larger fractions of reflected particles and shorter escaping times.

To further clarify this relation, the escaping times are presented in Figure 2.4 versus the pitch, averaged over the initial toroidal (left) and poloidal (right) angles. Once again, the results show the feeble toroidal dependence due to the underlying quasi-toroidal symmetry and that only reflected particles with initial pitch $|p| \lesssim 0.35$ are lost. This range of pitch values is consistent with the ripple strength calculated from $\sqrt{1 - B_{min}/B_{max}}$ (see Figure 2.3 left) for the flux surface under consideration, $r/a = 0.5$. The small pitch asymmetry observed is also compatible with the inward/outward excursion of trapped particles traveling in the co/counter magnetic field direction. The level contours of the toroidal average outline that more/less particles are lost from the outer/inner sides because of the $\sim 1/R$ dependence of the magnetic field with the major radius R. Furthermore, a comparison of both plots shows that the region originating faster losses corresponds to particles with near zero pitch located in the outer part of the stellarator where $|\theta| \lesssim \pi/4$. Particles born in the boundary between the trapped and passing regions (barely-trapped or barely-passing particles) are the ones surviving the longest.

2.2.5 Trapped Particle classification

The analysis presented for each configuration shows the relation between where particles were born and their final fate without describing the details about their trajectories. In symmetric configurations, most orbits can be classified into two types: those followed by passing particles, enclosing the magnetic axis and never changing the sign of their pitch, and the ones of reflected particles, bouncing back-and-forth and

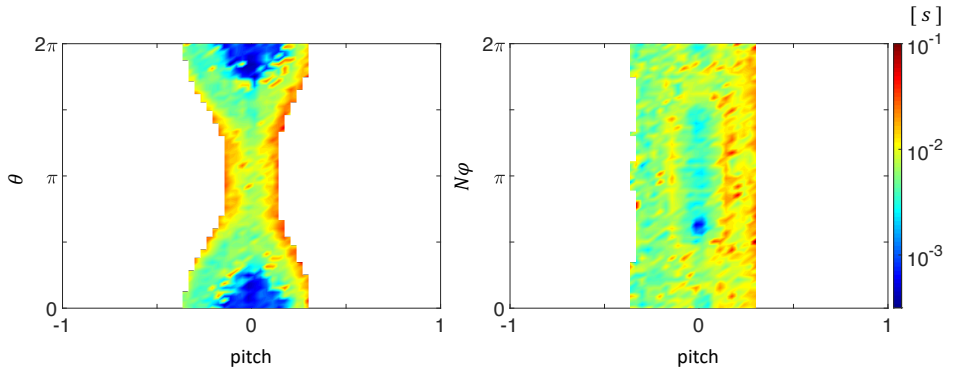

Figure 2.4: Contours of escaping times as a function of the initial pitch and poloidal angle, θ, averaged over the toroidal angle, φ, (left) and pitch and toroidal angle, φ, averaged over the poloidal angle, θ, (right). Both plots correspond to $r/a = 0.5$ and one period of the QTS72 configuration. White color means no losses.

describing *banana*-shaped trajectories never enclosing the axis. Alongside with these two basic types of orbits, the literature describes many other orbits which are usually special cases of these two. One limiting case is the potato shaped orbits that appears when the banana radial position is comparable to its width. As with bananas, these orbits change the sign of their pitch, but contrary to bananas encircle the axis. Another case is the stagnation orbits, which appears in the phase space boundary between passing and trapped regions where the guiding center speed v_g (see equation 2.1) vanishes. In general, these orbits do not encircle the axis nor change the pitch sign, though a general classification, see [47], is out of the scope of this work. The classification is not so simple when the symmetry is broken, even slightly. Along with the passing particles, whose confinement is always guaranteed in the collisionless limit, the lack of symmetry brings new families of orbits, whose radial drifts can lead to the loss of particles or transform trapped into passing particles and vice versa. Therefore, the key element in understanding the confinement of the quasi-symmetric configurations requires characterizing also the new trapped orbits.

The characterization includes the determination of its radial extension, the speed of their radial drift and the frequency of their bouncing. This is done by first selecting those parts of the trajectory of each particle in which it is trapped (this implies that no passing nor

stagnation orbits are considered). These sections are then analysed with a newly developed numerical procedure that classifies the orbits into four different types: bananas, ripple trapped, potatoes and others, and estimates, for the bananas, its center, width and bouncing time based on the pitch variation, particularly, the times at which the pitch changes sign.

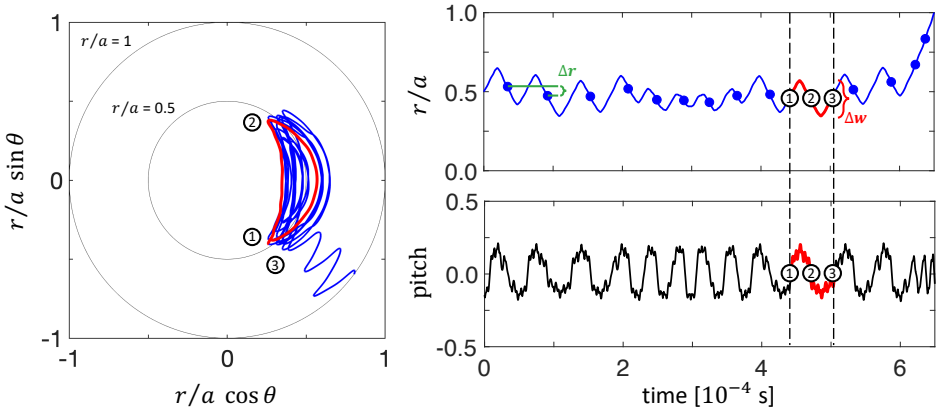

Figure 2.5: Left: poloidal projection of a trapped α-particle trajectory in Boozer coordinates for the QTS72 configuration from its initial position at $r/a = 0.5$ till its lost at r/a =1. Right: time evolution of the radial position r/a (top) and pitch (bottom) of the same trajectory. The centers of all the banana orbits are indicated by the blue circles (top), $\Delta r \sim 0.06$. The single banana orbit marked in red with reflection points labeled from 1 to 3 has a bouncing time τ ~30 μ s and a normalized orbit width of $\Delta w \sim 0.22$.

The classification of trapped orbits uses the poloidal angles at which particles cross the equatorial plane between three consecutive reflection points. Banana orbits, that do not encircle the magnetic axis, are indicated when they only cross the equatorial plane once between reflection points at an angle $\theta = 0$. Potato orbits, that do encircle the magnetic axis, are recognised by the sequence $\theta = 0$ on one orbit side and $\theta = \pi$ on the other, or vice versa. Ripple trapped orbits are distinguished because they do not cross the equatorial plane between consecutive bounces. Obviously, there are orbits that cannot be classified with this method like e.g. those that cross the equatorial plane many times. This is not a severe restriction since reflected orbits are classified for ITER as being $\sim$ 97.3% bananas, $\sim$ 0.2% potatoes

and $\sim$ 2.5% unclassified, while for the QTS configurations approximately 90% are bananas, between 2% (QTS4) and 6% (QTS72) ripple trapped, $\sim$ 1% potatoes and $\sim$ 5% unidentified. No effort was made in further classifying this 5%, though methods for including more types of orbits are advisable by using more than three consecutive reflection points and more complex criteria.

As an example of this method, the trajectory of one trapped α-particle for the QTS72 stellarator is shown in Figure 2.5 in poloidal cross-section (left) together with the time evolution of its radial position (right top) and corresponding pitch (right bottom). The key in the analysis is to notice that every banana orbit is defined by three reflection points, see Figure 2.5. In the figure one individual banana orbit is drawn in red and labeled with points from 1 to 3. The obvious definition of the bouncing time, τ, is the time that a particle spends between two reflection points. From the mid radial position between two consecutive orbit sides, e.g. r_{12} between r_1 and r_2 or r_{23} between r_2 and r_3 (see Figure 2.5), it is possible to define the normalized *banana* orbit center as the midpoint, $r_b = (r_{12} + r_{23})/2a$, and the banana width as the difference, $\Delta w = |r_{12} - r_{23}|/a$. Three different procedures were tried to estimate the mid radial positions between two consecutive reflection points using: i) the average radial position, ii) the radial position corresponding to the mid-time and iii) the radial position corresponding to the fastest parallel motion (the maximum absolute pitch). Finally, the second method was used because it is less computationally intensive, though all three procedures give almost the same results.

Every reflected particle trajectory is split into a series of banana orbits and the above method is applied to obtain a *reduced* banana trajectory consisting in the time evolution of its width, Δw, bouncing time, τ, and center, $r_b(t)$, shown as blue dots in the right upper plot of Figure 2.5. For the orbit of the figure, the bouncing time between points 1-2 and 2-3 is of the order of $\tau \sim 30$ μ s and the normalized orbit width, indicated on the right top plot with a bracket, is $\Delta w = 0.22$. This test particle executes twelve banana orbits in approximately 600 μs and slowly drifts radially from $r_b/a = 0.53$ to $r_b/a = 0.6$ before entering in what looks like a toroidal ripple to quickly drift out of the plasma.

In next section this analysis tool is used to statistically estimate the evolution of the banana centers, banana bouncing times and banana

widths for the five magnetic configurations with the idea of evaluating convective velocities and diffusion coefficients.

2.3 Results

In the collisionless limit, there is a deterministic relation between the initial conditions and the destination of every charged particle for a given magnetic configuration. For the *monoenergetic* α-particles, the initial conditions comprise a four dimensional phase-space with the three spatial dimensions and the pitch $(\psi, \theta, \varphi, p)$. Probability density functions of the bounce times and banana widths or the time dependence of the radial distribution of particles are the result of ensemble averaging over the myriad of possible trajectories. Instead of starting directly with the complete problem, we will first examine a simpler case for ITER configuration (where the toroidal angle φ is irrelevant) fixing the initial radial position at ψ_0, thus reducing the dimensionality of the problem from four to two dimensions (θ, p).

2.3.1 ITER bouncing times and banana widths

With the idea of scanning regions with different well depths, see Figure 2.1, the methodology described in Section 2.2.5 was applied to the trajectories of four sets of 4096 α-particles born with initial poloidal angles $\theta = \{0, \pi/4, \pi/2, 3\pi/4\}$, $r/a = 0.5$ ($\psi_0 = 0.25$) and uniformly distributed in pitch between $-0.6 < p < 0.6$ (i.e. in the approximate region where there are trapped particles). The uniform distribution in pitch guarantees that all trapped populations are considered equally. The fraction of reflected particles monotonically decreases with the initial poloidal angle from $\sim 50\%$ at $\theta = 0$, where the magnetic field is the weakest, to $\sim 18\%$ at $\theta = 3\pi/4$, where the magnetic field is stronger. The 1 ms time averaged bounce time $\langle\tau\rangle$ and banana width $\langle\Delta w\rangle$ of each particle are shown in Figure 2.6 as a function of the initial pitch and poloidal angle. The absence of collisions along with the perfect toroidal symmetry explains why in ITER the curves align nicely depending on its initial poloidal angle. Note that within the guiding center approach no relevant information can be drawn below the Larmor radius ρ_α.

In accordance with [47], the observed dependence of the banana

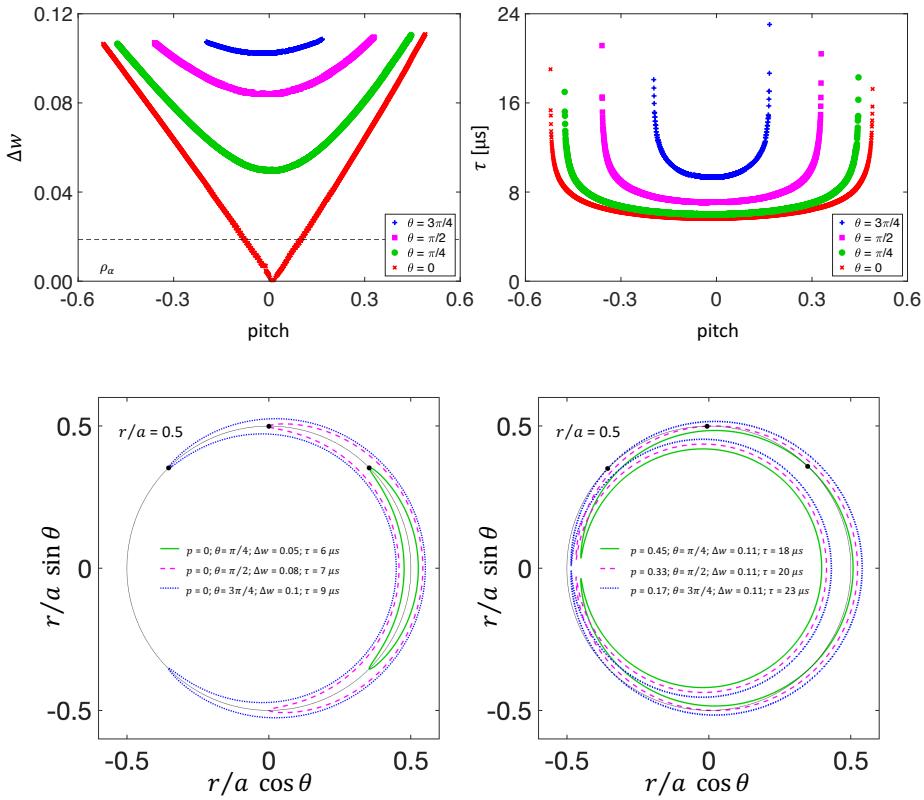

Figure 2.6: Orbit widths (upper left) and bouncing times (upper right) of reflected α-particles as a function of the initial pitch for ITER configuration. Toroidal projection of banana trajectories for $p = 0$ (lower left) and for initial conditions close to the passing-trapped boundary (lower right). Particles are started from $r/a = 0.5$ and distributed at four poloidal angles $\theta = 0$ (red), $\pi/4$ (green), $\pi/2$ (magenta) and $3\pi/4$ (blue). Each point corresponds to a 1 ms time average of a particle. The α-particle Larmor radius is shown for comparison with a dashed line in the upper left plot.

width on the initial poloidal angle and pitch shows that: i) Δw increases with the absolute pitch $|p|$, ii) there is a small pitch asymmetry due to the different inward(co) and outward (counter) banana orbits and to a lesser extent, to the a rotational transform profile, iii) there is a minimum width Δw for reflected particles depending on their initial poloidal position see the lower left plot of Figure 2.6 (the

higher the field the narrower the pitch range), iv) there is maximum width that does not depend on the initial poloidal position and v) at half radius, the widest bananas extend radially over 10% of the minor radius ($\sim$ 30 cm). Regarding the bouncing time it is found that except for the barely trapped particles (the ones initially started at magnetic field B_i and with pitch $|p| \lesssim \sqrt{1 - B_i/B_{max}}$) the bouncing time of most particles is relatively constant, between 6 and 10 μs for our conditions. These values are between 2 to 5 times larger than those traditionally used [16] for the bouncing time, $\tau \approx R/\iota\sqrt{\epsilon}v_\alpha \approx 1.5$ μs and the banana orbit width, $\Delta w \approx \rho_\alpha/\iota a\sqrt{\epsilon} \approx 0.06$, where R is the major radius, $\epsilon = a/R$ the inverse aspect ratio, ι the rotational transform, ρ_α the Larmor radius and v_α the speed. This is not very severe since these expressions are only valid for ideal tokamaks, vary across different authors up to a numerical coefficient [48, 49, 50], or describe specific particle behaviors or conditions [51, 52, 53].

The fact that bouncing times remain almost constant for a wide range of pitch values (parallel speeds) and initial poloidal positions is especially surprising for particles started at the outboard side because of the disparity of banana widths, compared with the curves corresponding to $\theta = 0$ in both upper plots of Figure 2.6. This occurs because larger widths are compensated by faster parallel motion (larger absolute pitch) in the same way as the product of the particle parallel speed with the distance along the particle trajectory leads to the conservation of the longitudinal adiabatic invariant $J = \oint v_\parallel \, dl$. Figure 2.6 also shows that the compensation breaks down for barely trapped particles that spend much longer times close to the bounce points, formally the bouncing time becomes infinite $\tau \to \infty$ [11] since the parallel speed $v_\parallel \to 0$. See the two lower plots of Figure 2.6. The lack of gyrophase correlation between consecutive bounces along with the inhomogeneity of the magnetic field is the ultimate reason for the stochastic transport processes described in the literature [59, 60, 65, 81].

We leave for the next section showing the probability density function of orbit widths and bouncing times when particles are distributed over the flux surface for all five configurations.

2.3.2 Probability density function of bouncing time, orbit width and radial orbit displacement

Using the algorithm presented in Section 2.2.5, which only applies to reflected particles, the ensemble average orbit widths and bouncing times are calculated for a set of 3.5 MeV α-particles started at $r/a = 0.5$ using the same initial distribution of Section 2.2.3 (i.e. uniformly distributed in pitch and randomly in the toroidal and poloidal Boozer angles with a distribution inversely proportional to the Jacobian of the transformation). In the case of the toroidally symmetric version of ITER, with a reflected fraction of 30%, this means that from a set of 65536 α-particle trajectories approximately 20,000 are used for the calculation. Since none of these particles get lost, the ensemble average is quite accurate. As for the stellarator configurations, with roughly the same reflected fraction of 20%, from the 262144 α-particle trajectories around 52,000 trajectories are used, though the ensemble average is not as accurate because trajectories are shorter due to the losses (see Figure 2.1 and Table 1).

To speedup the calculation particles that have not changed their pitch sign during the first 500μs of integration are stopped and eliminated. The precise cutoff was estimated from the escaping time contours of Figures 2.3 and 2.4 and the PDF of bouncing times of Figure 2.7 as a compromise between reducing computer time and taking into account transition particles in the calculation. The probability density functions (PDF) of the normalized banana widths and bouncing times obtained during the lifetime of the simulated particles are presented in Figure 2.7 for all five configurations. The PDFs were constructed using the constant bin content method [111] where in all cases each distribution contains more than 10^8 data inputs.

The probability density function of the normalized orbit widths Δw of reflected α-particles for ITER shows an approximately linear growth that ends abruptly at $\Delta w = 0.11$, in accordance with the negligible number of very small bananas and the maximum orbit width of the left plot in Figure 2.6. The PDFs of the normalized banana orbit widths for the QTS stellarators are much broader than for ITER, extending up to $\Delta w \sim 0.3$. This clearly indicates the appearance of new wide banana populations and severely puts into question any local approach to transport. There are two main differences compared to ITER: the most probable orbit width is almost twice as large $\Delta w = 0.18$ and that

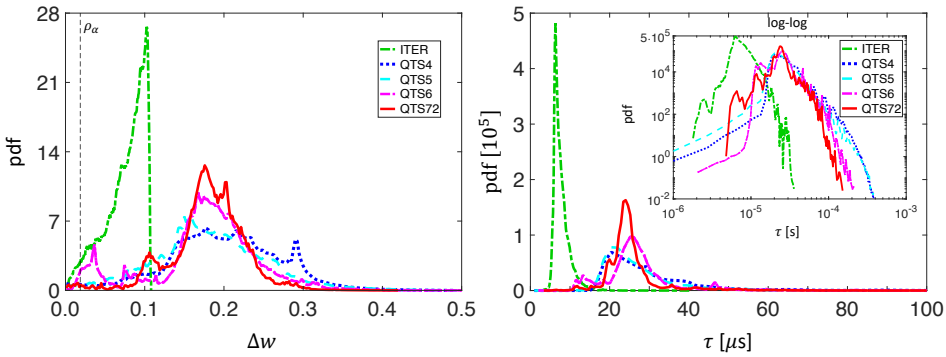

Figure 2.7: Left: Probability density functions of orbit widths, Δw, of trapped α-particles for ITER and the four quasi-toroidal stellarators. Right: Probability density function of bouncing times, τ, in linear and logarithmic scales.

there are other side peaks in the PDF. The extra peaks are probably due to the high order small modular ripples and wider helically trapped bananas.

The right plot of Figure 2.7 shows the probability density function of the bouncing times τ of trapped α-particles in linear and logarithmic scales. The PDF for ITER has a sharp rise, peaking around $\tau = 8$ μs, followed by a very fast decay (see the log-log scale) ending a bit earlier than $\tau = 16$ μs, which is in perfect agreement with the right plot in Figure 2.6. The results for the four stellarators are also much broader with the most probable values between $\tau = 20$ and 25 μs. Unfortunately, there is no simple way to compare these results with any analytical expression since little is known about the characteristic scales of motion of trapped particles in stellarators [54, 86, 55] (or even non-ideal tokamaks) and it is unclear to what extent they differ from ideal tokamaks. This is because of the high order field modes, which are virtually impossible to consider analytically and whose effect might be insignificant for trapped particles in general but may be substantial for α-particles. The only available results were carried out numerically for specific configurations considering only the main components of the magnetic field neglecting the rest of the spectrum [47, 56, 57, 58].

The logarithmic scale reveals another difference between the configurations. Whereas an exponential decay in the PDF of ITER starts around $\tau = 10$ μs and lasts till $\tau = 50$ μs, the decay for the stellarators

not only starts much later $\tau = 50$ μs but also continues much longer $\tau = 200$ μs. These long tails imply that there are much longer characteristic bouncing times, though their impact into PDFs is of minor relevance - five to nine orders of magnitudes smaller compared to the peak values.

The last piece of information collected from reflected particle trajectories is the evolution of the center of the orbits, $r_b(t)$, and more specifically, the displacements of orbit centers $\Delta r(t_i) = r_b(t_{i+1}) - r_b(t_i)$. In the stochastic view [59, 60, 65, 81] of collisionless transport, it is precisely the *random-walk* displacement of the orbits which gives rise to diffusion. In Figure 2.8 the probability density function of the orbit center displacements is presented for the five configurations under study. The displacement of ITER trapped orbits is negligible because of its pure toroidal symmetry. On the other hand, the broken symmetry configurations display large and inward/outward asymmetric displacements, which become narrower with higher toroidal symmetry. Note that the most probable orbit widths for these configurations is around $\Delta w \approx 0.2$, and there is a significant probability of having quite large displacements Δr, e.g. the cumulative probabilities $P(|\Delta r| \geq 0.05) \sim 0.25$ and $P(|\Delta r| \geq 0.1) = 0.05$. Moreover, the PDFs clearly show a complex structure with several slopes corresponding to different spatial scales, possibly due to different orbit types, that put into question the local and diffusive nature of the underlying process.

The behavior of reflected particles, rebounding at regions of high magnetic field, together with the structure of the magnetic field along the field lines, shown in Figure 2.1, suggest other procedures to characterize the configurations and estimate the bouncing times, which offers the possibility to confirm the results of this Section 2.3.2.

2.3.3 Bouncing times and connection lengths

So far, the bouncing time was calculated integrating the guiding center trajectories and explicitly measuring how long does it take particles to reverse their parallel motion. A possible way to validate the results of Section 2.3.2 is to assume that particles where simply streaming along the field lines. In this approach the time of going along the field line from l_1 to the next consecutive bounce point l_2 would just be $\tau(B) = \int_{l_1}^{l_2} dl/v_\parallel$ where $v_\parallel(l) = v_\alpha \sqrt{1 - B(l)/B}$ and $v_\alpha = 1.3 \times 10^7$

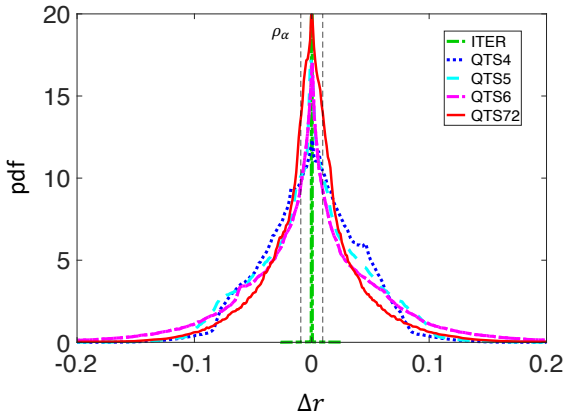

Figure 2.8: Probability density functions of orbit center displacements Δr (see right upper plot of Figure 2.5) of trapped α-particles for ITER and the four stellarator configurations.

m/s. However, to use this approximation it is necessary to justify that the distance travelled along the field line between bounces is approximately the same as the guiding center trajectory. The fact that the most probable banana widths are $0.1\,a$ (~ 30 cm) for ITER and $0.2\,a$ (~ 60 cm) for the stellarators (see Figure 2.7) is an encouraging first step, but is not enough until the average distance between bounce points along the field line $\langle |l_2 - l_1| \rangle$ is known. Estimating this distance for an ideal circular tokamak is not very difficult but the same calculation for a D-shape tokamak or a general stellarator has to be done numerically integrating the actual distance along the field line and using the 3D geometric properties of the equilibrium field. Fortunately, this can be done using the toroidal coordinates, (R, Z, φ), of a flux surface ψ, which are given by a series expansion in Boozer coordinates, (θ, φ), similar to equation 2.1:

$$R^\psi(\varphi,\theta) = \sum_{m,n\neq 0} {}^cR^\psi_{mn}\cos(m\theta - nN\varphi) + {}^sR^\psi_{mn}\sin(m\theta - nN\varphi) \quad (2.5)$$

$$Z^\psi(\varphi,\theta) = \sum_{m,n\neq 0} {}^sZ^\psi_{mn}\sin(m\theta - nN\varphi) + {}^cZ^\psi_{mn}\cos(m\theta - nN\varphi) \quad (2.6)$$

Exploiting that in Boozer coordinates the magnetic field lines are described simply by $\theta = \iota\varphi$, the arc length along the field line and

the magnetic field magnitude can be both parametrized as a function the toroidal angle using $dl(\varphi) = \sqrt{(dR/d\varphi)^2 + R^2 + (dZ/d\varphi)^2}d\varphi$ and the expansions of equations 2.5 and 2.6. Note that $l(\varphi)$ contains the dependence of the flux surface geometry and the local rotational transform (which is constant in Boozer coordinates) and makes $B(l)$, see Figure 2.9, different from $B(\theta)$ shown in Figure 2.1, though they look similar.

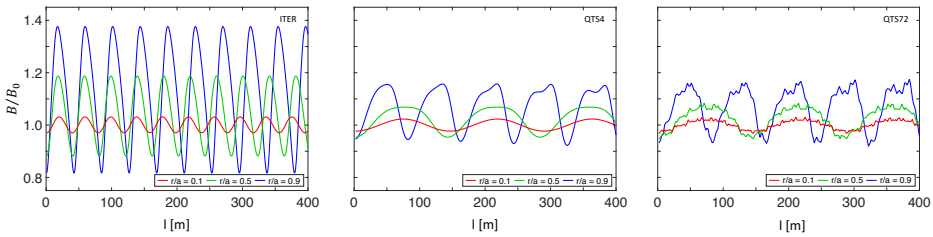

Figure 2.9: Normalized magnetic field strength along the field line passing through $\theta = \varphi = 0$ as a function of the distance along the field line for three radial positions $r/a = 0.1$, 0.5 and 0.9 at ITER (left) and the quasi-toroidal stellarators QTS4 (center) and QTS72 (right).

If particles were just streaming along field lines, without drifting radially, reflected particles would be bouncing between consecutive points with the same magnetic field. There is a neat way to obtain the characteristic lengths, i.e. the connection lengths, of a configuration for a given flux surface by applying the discrete Fourier transform to $B(l)$, see Figure 2.10. The main spatial periodicities of the magnetic field, giving rise to the banana orbits, appear as peaks in the Fourier transform, from which the main connection lengths can be calculated for every magnetic configuration and magnetic surface. To accurately capture all the details of the configurations is necessary to follow the field line over a sufficient number of turns around the device. While there is only one significant connection length for ITER of the order of 40 m $\approx 2\pi R$ ($R = 6.2$ m), the stellarator configurations clearly show two of them. The longer connection lengths found for the stellarator configurations, ≈ 140 m, are due to their larger aspect ratio and helical magnetic field components. The largest modes for these stellarators are basically equal because they correspond to the same underlying configuration described by different number of Boozer modes. Moving away from quasi-symmetry, as in QTS72, lead to the

appearance of shorter connection lengths with amplitudes larger than 10% of the largest mode. The leading connection lengths obtained using the Fourier transform for ITER, QTS4 and QTS72 are summarized in Table 2.3 at three radial positions, $r/a = 0.1$, 0.5 and 0.9. The small radial dependence found for ITER is due to the compensation between the field line pitch and the radius, which changes from almost circular close to the axis to a D-shape at outer radii. For the stellarators, the observed smaller connection lengths at outer radius are probably due to the increased importance of the toroidal components, which corresponds to the second most important harmonic ($R = 9.8$ m; $2\pi R \approx 60$ m).

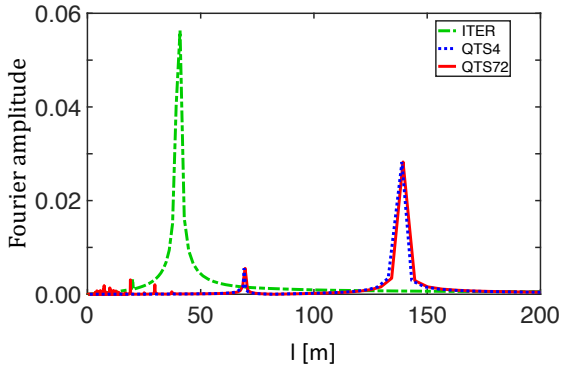

Figure 2.10: Fourier mode magnitude of the magnetic field along a field line versus $2\pi/k$ at $r/a = 0.5$ for ITER, QTS4 and QTS72.

Table 2.3: Connection lengths, bouncing times and fraction of reflected particles, f_r, for ITER and the quasi-toroidal stellarators QTS4 and QTS72 at three radial positions. Only connection lengths with Fourier mode amplitudes larger than 10% of the largest mode are shown in decreasing order of magnitude.

	ITER			QTS4			QTS72		
r/a	l [m]	τ [μs]	f_r	l [m]	τ [μs]	f_r	l [m]	τ [μs]	f_r
0.1	41	14	15%	142	56	13%	146 - 71 - 17	17	16%
0.5	41 - 20	6	31%	137 - 69	28	18%	139 - 69 - 16	13	22%
0.9	39 - 20	4	38%	76 - 38	10	25%	76 - 40	8	29%

The smooth radial dependence of the connection lengths together with their magnitude, much larger than that of the most probable radial extension of the orbits (see Figure 2.7), justifies the assumption that the particles approximately stream along the field lines. Therefore, using the dependence of the magnetic field on the distance along the field line for several turns around the device, it is possible to estimate the average bouncing times for the trapped α-particles using the conservation of energy, $\mathcal{E} = mv^2/2$, and magnetic moment, $\mu = mv_\perp^2/2B$. For a connected region along the field line with magnetic field smaller than a given value $B(l_i < l < l_{i+1}) < B_j$ for $i = 1, ..., N_j$, the time taken between bounces in that well is obtained as the integral $\tau_i(B_j) = \int_{l_i}^{l_{i+1}} dl/v_\parallel$. The procedure is repeated for all connected regions N_j along the field line to get a mean bouncing time for a given magnetic field value $\langle \tau(B_j) \rangle = \sum_i \tau_i(B)/N_j$. Finally, the method is replicated in a regular pitch grid which corresponds to the magnetic field values $B_{min} < B_j < B_{max}$ for $j = 1, ..., N$ to get the mean bouncing time $\tau = \sum_j \langle \tau(B_j) \rangle / N$. A sketch of the procedure is outlined in Figure 2.11. Likewise, the fraction of reflected particles can be calculated averaging the pitch range over which particles are trapped depending on the depth of the magnetic wells along the field line $\langle f_r \rangle = \int \sqrt{1 - B(l)/B_{max}} dl / \int dl$.

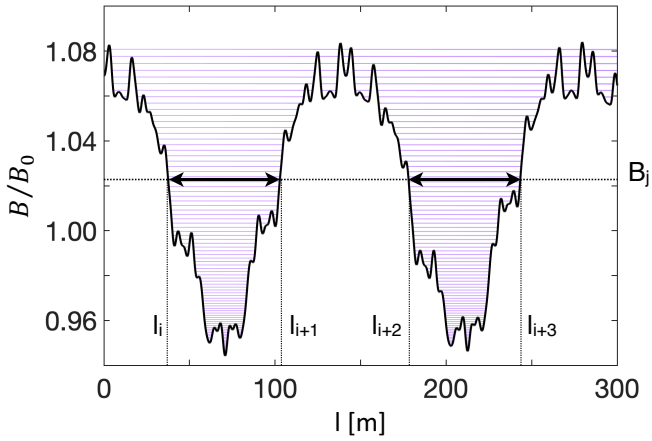

Figure 2.11: Magnetic field strength versus the length along a field line passing through $\theta = \varphi = 0$ for $r/a = 0.5$ of the QTS72 configuration.

The results of this analysis show a decrease of the bouncing time

for increasing radius, independently of the configuration. In case of ITER, τ ranges from 14 μs in the center to 4 μs at the edge. The explanation for the longer bouncing times (56 - 10 μs) for the QTS4 stellarator is their longer connection lengths. This effect is compensated by the appearance of shorter connection lengths related to the new ripples in the QTS72 stellarator (17 - 8 μs). It is important to notice, that whereas the connection length l is a property of the equilibrium magnetic field, the bouncing time τ is an approximation of the real α-particle motion assuming that particles move along the field lines. The remarkable agreement found in all cases between the bouncing times obtained for $r/a = 0.5$, see Table 2.3, and the most probable values obtained from the banana orbits of the α-particles, shown in Figure 2.7, support both the Monte Carlo calculations and the procedure just described along with its approximations. Moreover, the fraction of reflected particles $\langle f_r \rangle$ at $r/a = 0.5$ of Table 2.3 is also in accordance with the values of Table 2.2.

The connection lengths found are between 40 and 150 m, the average banana radial scale length ranges from $0.1a \sim 0.3$ m at ITER to $0.3a \sim 0.6$ m for the four stellarators, which barely supports the local approximation when the minor radii are $a = 2.62$ m and $a = 2.90$ m respectively. On the positive side, both results support the small gyroradius approximation $\rho_\alpha \sim 5$ cm and the gyroaveraged guiding center equations of motion used in this work. The average bouncing times found range from 10 to 30 μs, which are far from α-particle collisional slowing-down $\tau_{slow} \sim 1$ s and scattering $\tau_{scatt} \sim 5$ s times and the expected confinement timescales $\tau_E \sim 5$ s [101], thus partly justifying neglecting collisions in the simulations.

2.3.4 Transport dynamics

The traditional approach to estimate radial transport consists in assuming that it can be described by a continuous-time stochastic Wiener [112] process, usually referred to as Brownian motion [113] or *random walk*. A convective velocity V and a diffusion coefficient D are traditionally defined from the time evolution of the radial distribution of a set of particles initialized at the same radial position and randomly distributed in the poloidal and toroidal angles and in pitch by using the running moments method [114]. This method, based on [45] estimates both V and D from the slopes of the first and second mo-

ments of the radial distribution dependence on time: $\langle \tilde{r}_b \rangle \sim Vt$ and $\langle (\tilde{r}_b - \langle \tilde{r}_b \rangle)^2 \rangle \sim 2Dt$ at very long times, and where $\tilde{r}_b$ is the radial distance travelled by the center of the banana. Thus, in principle one can evaluate the collisionless convection and diffusion due to a magnetic field inhomogeneity from the time dependence of ensemble averages, $\langle\ \rangle$, of the radial particle distribution.

What is often forgotten is that this method and the underlying assumptions can only be applied when the number of particles is conserved, i.e. when the zero-order moment of the distribution does not depend on time, and for unbound systems (or systems where particles never approach the limits of the system). A condition that only applies when the process is sufficiently slow or when particles do not depart significantly (local *ansatz*) from their initial locations r_0. Unfortunately, the probability density functions of orbit displacements, Δr, and banana width, Δw, shows that this condition is not fulfilled and moreover a considerable fraction of reflected particles can leave the plasma in the quasi-symmetric configurations.

So, the question is to what extent α-particle transport can be described by a Wiener process in toroidally symmetric and quasi-symmetric configurations. The easiest way is to calculate the time dependence of the radial probability density function of α-particle banana orbit centers and check if it has a gaussian shape and/or if it radially drifts. This was done from the simulations of Section 2.3.2 where the escaping times and radial position of the banana orbit centers were stored at fixed times using the method described in Section 2.2.5. The escaping time is needed to discard lost reflected particles from the calculation to preserve the conservation of probability.

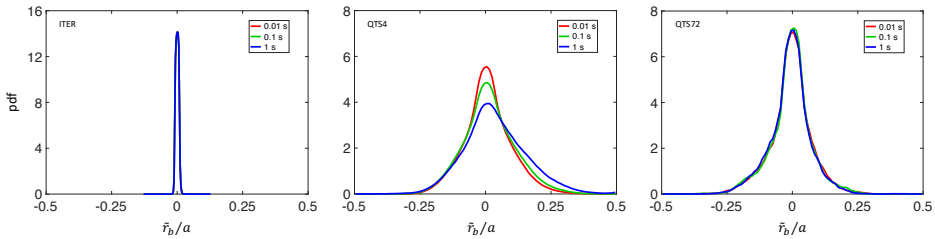

Figure 2.12: Probability density functions of normalized orbit centers, $\tilde{r}_b/a$, for confined reflected α-particles for ITER (left), QTS4 (center) and QTS72 (right) at $t = 0.01, 0.1$ and 1 s.

The radial probability density function of orbit centers of confined reflected α-particles is presented in Figure 2.12 for ITER (left), QTS4 (center) and QTS72 (right) configurations at three instants: $t = 0.01, 0.1$ and 1 s. The centers of the banana orbits at ITER, as expected, do not broaden nor drift radially neither inwards nor outwards. The observed width of the distribution, $\Delta r = 0.02a \sim 5$ cm $\approx \rho_\alpha$ serves as an indication of the accuracy of the algorithm determining the banana orbit centers (see Section 2.2.5). The results for the QTS72 configuration (Figure 2.12 right) are a bit surprising at first since they resemble those of ITER, although with a much broader radial distribution, which suggests a similarity between the orbit types that survive until 1 s. The difference being that they are a 31% of the particles in ITER and a minuscule 1% in QTS72 (see Table 2.2). The only confined reflected particles in QTS72 are radially frozen because otherwise they would have been lost. The central plot of Figure 2.12 shows a substantial and asymmetric broadening together with a slow outward radial drift for QTS4 configuration. Some particles will be inevitably lost soon after 1s; something that can be anticipated seeing the positive slope of the loss fraction for QTS4 in Figure 2.2.

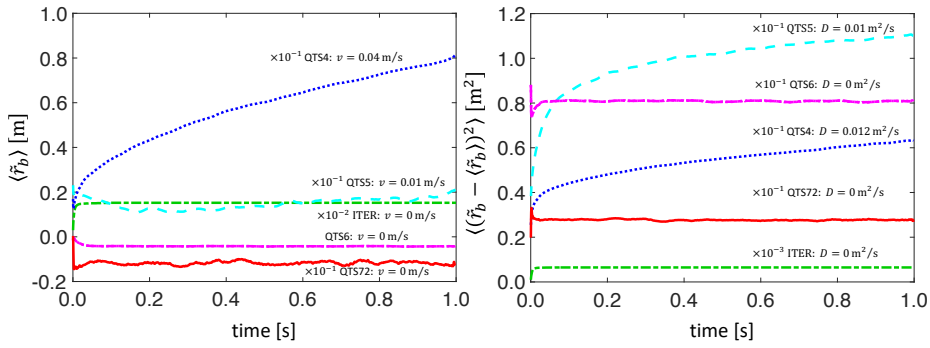

Figure 2.13: Time dependence of the first (left) and second (right) moments of the probability density function of confined reflected α-particles for ITER and the four QTS configurations.

Applying the running moments method to these radial distributions confirms numerically the visual result of Figure 2.12. There are almost no convection nor diffusion for ITER, QTS6 and QTS72, $D \sim V \sim 0$, see Figure 2.13. This is consistent with the collisionless approximation for all ITER reflected particles and the very few

QTS6 and QTS72 reflected particles that are not lost in 1 s and also demonstrates that *numerical diffusion* was kept under control in the simulations. For the QTS4 and QTS5 configurations, the values obtained for the convective velocity and the diffusion coefficient from the slope of the first and second moments of the radial distribution are $V = 0.04$ m/s and $D = 0.012$ m^2/s and $V = 0.01$ m/s and $D = 0.01$ m^2/s respectively.

The source of diffusion for the configurations with broken symmetry is the so-called stochastic diffusion, which is due to the magnetic field inhomogeneity [60, 65, 81, 75]. Even for conditions of mildly breaking the toroidal symmetry like in the QTS4 configuration with $\sigma_{qt} \approx 0.9$ at $r/a = 0.9$ and where the fraction of losses is small $< 4\%$, one may be tempted to conclude that these are the transport coefficients of α-particles. However, these values should be put into question when one considers the clear asymmetry of the distribution, its non-gaussian shape and that part of the left side of the distribution remains the same for almost one second, see Figure 2.12. A remainder that within the 15% of confined reflected particles a certain fraction has no radial drifts, like in ITER and QTS72, though its identification and separation does not seem possible at the moment. Farther away from symmetry, like in the QTS72 configuration with $\sigma_{qt} \approx 0.6$ at $r/a = 0.9$, there is a $\sim 20\%$ of losses and the only confined reflected particles are the ones that do not suffer stochastic diffusion, thus giving the same result as for ITER. An analysis based on ignoring the warnings and using all trapped particles will result in a time varying PDF normalization (because of the loss of particles) from which no relevant statistical conclusions can be drawn.

Throughout this work, collisions have been intentionally neglected to highlight the link between the magnetic field and the dynamics of α-particles. Collisions mix different types of orbits causing passing particles to become trapped and vice versa, producing diffusion both in real and momentum spaces. For reactor conditions, the characteristic spatial and temporal scales are the banana width and the collisional time. In the case of ITER, where collisionless banana orbits are not drifting radially, see Figure 2.13, the convective velocity will remain negligible, but the expected diffusion coefficient instead of being zero will depend on the most probable banana width, $\Delta w \sim 0.1$, and the inverse collision time [115], $1/\nu_{coll} \sim 0.1$ s, thus giving $D \sim a^2 \Delta w^2 \, \nu_{coll} \sim 10^{-2}$ m^2/s. The situation is different for the stellarator configurations since

the effect of collisions is barely noticeable below $\sim 10^{-2}$ s [93], i.e. well before losses in QTS4 have started and after most of the QTS72 losses took place, see Figure 2.2. This time scale is too slow compared to the bouncing times of QTS4, $\tau \sim 20$ μs, and results in a diffusion coefficient, $D \sim a^2 \Delta w^2/\tau \sim 2 \times 10^4$ m^2/s, inconsistent with the running moments method. As for QTS72, one can expect that some confined orbits are scattered by collisions into regions that further increase the losses, thus supporting the conclusion that the process is not diffusive.

2.4 Summary and Conclusions

The original goal of this work was to study the effect of breaking the toroidal symmetry of the magnetic field on the transport of collisionless α-particles. To that end, five magnetic configurations were considered with different quasi-toroidal symmetry ratios σ_{qt}: a purely toroidal case with $\sigma_{qt} = 1$ and the parameters of ITER, that serves as a reference, and four stellarator examples, with $\sigma_{qt}(r/a = 0.5)$ ranging from 0.94 (QTS4) to 0.62 (QTS72) derived from a configuration inspired in the NCSX project. The behavior of α-particles was studied with the guiding center orbit following code MOCA.

The analysis of averaging escaping times of an ensemble of particles allowed to estimate the losses of every configuration and its dependence on the birth position. In the symmetric configuration only two types of confined particles, passing and reflected, were found. When toroidal symmetry is broken, apart from passing particles only trapped and transition particles born close to the magnetic field maximum remain confined. Two different methods were used to obtain the fraction of reflected particles f_r, one based on particle trajectories and the other on the magnetic well depth.

A novel algorithm was introduced to define the trapped orbit center, width, and bouncing times based on particle trajectories. It was confirmed that banana width and bouncing times increase as the configuration departs from symmetry. New bouncing times appear as a result of the new field ripples of the quasi-toroidally symmetric configurations. These results were corroborated by independent numerical procedures for calculating the average bouncing times and connection lengths along the field lines. The statistical analysis of the orbit center displacements, responsible of the stochastic collisionless transport,

points to the existence of several entangled spatial scales.

Transport coefficients were estimated by using the calculated most probable banana width and bouncing times ($\Delta w \sim 0.2$ and $\tau \sim 30$ μs) and by fitting the time dependence the moments of the radial probability density functions. For the QTS4 configuration, for which both methods can be compared, the first procedure, returns results for the diffusion coefficient $D \sim 2 \times 10^4$ m^2/s which is inconsistent with those obtained by the second method, $D \sim 10^{-2}$ m^2/s.

The results obtained here put into question the classical convection/diffusion approach to adequately describe collisionless trapped α-particles transport as the magnetic configuration departs from toroidal symmetry, a result that can probably be applied to other symmetries. A description based on the use of *fractional transport equations* [43] for collisionless α-particle transport is underway.

Acknowledgements

The authors would like to thank R. Sánchez, A. Bustos and J. Alcusón for fruitful discussions. This work was supported in part by the Spanish project ENE2012-33219 and the Erasmus Mundus Program: International Doctoral College in Fusion Science and Engineering FUSION-DC. Part of this research was carried at the Max-Planck Institute for Plasma Physics in Greifswald (Germany), whose hospitality is gratefully acknowledged. MOCA calculations were done in Uranus, a supercomputer cluster located at Universidad Carlos III de Madrid and funded jointly by EU-FEDER and the Spanish Government via Project No. UNC313-4E-2361, ENE2009-12213-C03-03, ENE2012-33219 and ENE2015-68265.

Chapter 3

Non-diffusive transport of α-particles

The content of this chapter was accepted for publication in **Physics of Plasmas** by A. Gogoleva, V. Tribaldos, J.M. Reynolds-Barredo, R. Sánchez, J. Alcusón and A. Bustos under the name "*Non-diffusive nature of collisionless α-particle transport: dependence on toroidal symmetry in stellarator geometries*". It is reproduced here with the permission of the copyright owner *AIP publishing*. For the consistency with the rest of the manuscript, the typography has been adapted and only small changes in notation have been made.

In this chapter we addressed the nature of the collisionless α-particle transport resulting from the inhomogeneities of the magnetic field in cases of quasi-toroidal stellarators with different levels of symmetry using the fractional transport theory. Our results indicate that the α-particle ripple-enhanced transport is non-Gaussian, non-Markovian and become strongly subdiffusive as the level of quasi-toroidal symmetry increases. These findings not only question the validity of the diffusive model, which is frequently used *per se* for the theoretical and experimental interpretations of fast particle transport, but also determine the fractional transport coefficients for describing it. A better understanding of the α-particle dynamics is essential for the development of the future fusion-based reactors, in particular of the stellarator kind.

Abstract

An adequate confinement of α-particles is fundamental for the operation of future fusion powered reactors. An even more critical situation arises for stellarator devices, whose complex magnetic geometry can substantially increase α-particle losses. A traditional approach to transport evaluation is based on a diffusive paradigm, however, a growing body of literature presents a considerable amount of examples and arguments towards the validity of non-diffusive transport models for fusion plasmas, particularly in cases of turbulent driven transport [R. Sánchez and D.E. Newman, Plasma Phys. Control. Fusion **57** 123002 (2015)]. Likewise, a recent study of collisionless α-particle transport in quasi-toroidally symmetric stellarators [A. Gogoleva *et al.*, Nucl. Fusion **60** 056009 (2020)] puts the diffusive framework into question. In search of a better transport model, we numerically characterized and quantified the underlying nature of transport of the resulting α-particle trajectories by employing a whole set of tools, imported from fractional transport theory. The study was carried out for a set of five configurations to establish the relation between the level of magnetic field toroidal symmetry and the fractional transport coefficients, i.e. the Hurst H, the spatial α and the temporal β exponents, each being a merit of non-diffusive transport. The results indicate that the α-particle ripple-enhanced transport is non-Gaussian and non-Markovian. Moreover, as the degree of quasi-toroidal symmetry increases, it becomes strongly subdiffusive. Although, the validity of the fractional model itself becomes doubtful in the limiting high and low symmetry cases.

3.1 Introduction

There is still no fully satisfactory explanation of the experimental particle and energy transport across the magnetic field in fusion devices. The cost of an economically viable thermonuclear fusion powered reactor is largely determined by this radial transport that has, so far, been estimated and extrapolated using semi-empirical methods based on traditional diffusive-like models. However, it is still unclear whether these models are sufficiently complete and adequate to describe radial transport in all reactor-relevant regimes. These are pressing issues

for the radial transport of α-particles, whose confinement is essential for the overall plasma performance. This transport has been assumed diffusive in the literature [66, 97, 98, 99, 59, 60, 81], which allowed to create transport models able to fit the relevant experimental data [65]. However, the diffusion paradigm rests on the assumption that transport dynamics is Gaussian and Markovian thus it fails to adequately describe systems with correlations, memory and spatial effects [43]. In fact, turbulent transport has been shown to be superdiffusive when it is close to marginal state and for weak mean/zonal flows; this effect was considered on the example of the gradient-induced instabilities [25, 26, 27, 28] and dissipative trapped-electron modes (DTEM) instabilities [29, 30, 31]. On the contrary, turbulence induced transport across flows with sufficient shear tends to be subdiffusive; as it was demonstrated on some instances of the ion temperature-gradient modes (ITG) [32, 33, 34, 35, 36] or shear Alfvén, drift tearing and ballooning modes [37, 116]. In the particular case of quasi-poloidally symmetric stellarator geometries, turbulent transport associated with supercritical ITG turbulence becomes subdiffusive [36] as the degree of quasi-poloidal symmetry increases triggering the effect of sheared flows. Also, a number of experimental and numerical studies at TORPEX [38, 39, 40, 41, 42] has demonstrated that suprathermal ion transport changes from being subdiffusive to superdiffusive depending on the ion energy and turbulent fluctuation amplitudes. Furthermore, while large intermittent and persistent $\mathbf{E} \times \mathbf{B}$ drifts lead to superdiffusion their suppression results in subdiffusion.

On the other hand, it was found [117] that the α-particle transport for realistic ITG and TEM turbulent regimes is diffusive and becomes significant only at energies ~ 100 keV. A recent work [118] shows clear indications of the non-diffusive nature of 3.5 MeV α-particle neoclassical transport; i.e. when transport originates from the averaged radial drifts due to the non-uniform three-dimensional magnetic field and not from the collisions dynamics, which is low enough to be neglected. This transport is of special relevance for stellarator geometries, whose non-axisymmetric character strongly impacts particle dynamics. In fact, the confinement of α-particles is one of the most critical points in the design of a viable stellarator fusion reactor [81, 91, 92, 93, 90].

The aim of this work is to examine the collisionless α-particles neoclassical transport [118] by means of fractional transport theory adapting the techniques used in characterizing the non-diffusive dy-

namics of turbulent transport [43]. Of particular interest is the effect of the level of quasi-toroidal symmetry on the fractional transport coefficients. To this end, five configurations stepwise breaking the symmetry were considered: from a perfectly symmetric ITER tokamak model to four stellarator configurations with different levels of quasi-toroidal symmetry. Fractional transport coefficients were estimated applying Lagrangian and Eulerian techniques to a set of trapped α-particle trajectories corresponding to the largest fraction of losses obtained with the Monte Carlo orbit following code MOCA [94, 119, 104, 118]. The set comprises only the confined part of these particle trajectories, i.e. before the particles are lost, to avoid contaminating the statistics with the effect of ripple at the outer radial positions, which leads to convective (ballistic) behavior.

The remainder of the paper is organized as follows. Section 3.2 presents the basic approximations used, the magnetic configurations considered and the numerical tools applied. The techniques of fractional transport theory and their application are described in Section 3.3. A summary of the results is given in Section 3.4. The final Section 3.5 briefly discusses the validity of a non-diffusive approach in building an effective model of ripple-enhanced α-particle transport.

3.2 Approximations, Magnetic Configurations and Numerical Methods

This section summarizes the main approximations used, introduces the magnetic configurations under study and the equations of motion of α-particles together with some details about the numerical neoclassical code MOCA.

The three approximations applied here are the *small gyroradius ordering*, neglecting the electric field and neglecting the α-particle collisions. Along with these approximations, throughout all simulations particles are considered monoenergetic and all perturbations (e.g. Alfvén, drift tearing, ballooning, ..., modes) are neglected. The spatial and temporal drift orderings are justified (except perhaps in the pedestal region) because of the ratio between, on the one hand, the large spatial scale lengths of field corrugations $L \sim 1$ m and orbit widths $L \sim 0.5$ m in reactor conditions with the α-particle Larmor radius $\rho_\alpha \sim 0.05$ m, and, on the other hand, the slow circulating $\tau \sim 5\mu$s,

bouncing $\tau \sim 20\mu$s, collisional slowing-down $\tau_{slow} \sim 1$s and scattering $\tau_{scatt} \sim 5$s times compared with the cyclotron times. The orbit widths, circulating and bouncing times were obtained in Ref. [118], while the slowing-down and scattering times correspond to typical reactor conditions, i.e. $n \sim 1$ and 5×10^{20} m^{-3} as $T \sim 25$ and 15 keV for tokamaks and stellarators respectively. The reason for ignoring electric field effects is the huge difference between the α-particle speed $v_\alpha \approx 1.3 \times 10^7$ m/s and the $\mathbf{E} \times \mathbf{B}$ drift speed, or either the unrealistic electric fields required to make them comparable. Finally, to focus only on the relation between the symmetry level of the magnetic configuration and α-particle dynamics, collisions will be neglected.

In this work, the magnetic configurations considered are based on an ideal ripple-less tokamak with ITER [95] parameters, $B \sim 5.3$ T, $a = 2.67$ m, $R = 6.2$ m and $V \sim 900$ m^3 (approximately corresponding to a $Q \approx 10$ and $I_p = 15$ MA scenario) and a quasi-toroidally symmetric (QTS) stellarator loosely based on a vacuum NCSX [12, 14] project configuration and having the same nominal field and volume as ITER but a different size $a = 2.15$ m, $R = 9.8$ m. The structure of the magnetic field for these two configurations was obtained using the 3D ideal Variational Magnetohydrodynamic Equation solver Code VMEC [102] and thus excludes the existence of both islands and stochastic regions. Since the orbit following code MOCA works in Boozer coordinates, the two VMEC equilibria are decomposed in Boozer [7] magnetic flux coordinates using 1050 modes to guarantee a precise description of the equilibria. Notice, however, that the accurate calculation of particle trajectories, just depending on the magnetic field magnitude, requires much less modes than those needed to capture its three dimensional shape. Moreover, particle orbits depend on spatial scales larger than those needed for stability calculations (ballooning, peeling-ballooning, ...) where a precise representation of small scales is necessary to localize unfavorable regions on the flux surfaces.

Based on the neoclassical community experience [104], to accurately describe the *long mean free path* collisionality regime, similar in requirements to our analysis of collisionless α-particles, it is sufficient to consider only the Boozer normalized harmonics larger than a threshold $\delta = 10^{-3} - 10^{-4}$, even for stellarators as complex as TJ-II [94]. To be on the safe side, the smallest threshold $\delta = 10^{-4}$ was used to obtain the ITER and QTS72 magnetic field configurations which have seven and 72 modes respectively. Though this number

of modes is insufficient to capture the smallest spatial scales of the original equilibrium, and cannot be used to perform any stability calculations, it is adequate to describe the original VMEC equilibrium magnetic field and provides the two references for our work: an ideal axisymmetric tokamak and a realistic quasi-toroidally symmetric stellarator. Nevertheless, to be sure that the configuration QTS72 was sufficiently close to the original QTS equilibrium, all the procedures described in this work were applied to a magnetic field configuration obtained with $\delta = 10^{-5}$ and having 197 modes, giving results almost identical, within the error bars, to that of QTS72. Since both, the full QTS and QTS72 magnetic field configurations are relatively far from being axisymmetric, see Figure 3.1, the strategy followed to study the effect of approaching quasi-toroidal symmetry was to use the original Boozer decomposition of the QTS equilibrium and increase stepwise the threshold put on the normalized harmonics from $\delta = 10^{-4}$ of QTS72 to 1/180, 1/150 and 10^{-2} to obtain magnetic configurations with 6, 5 and 4 modes respectively, see Figure 3.1. This process guarantees that the ripples introduced by these modes are included based on their importance to the original QTS equilibrium. QTS4 contains the following four $B_{m,n}$ modes: $B_{0,0}$, $B_{1,0}$, $B_{2,0}$ and $B_{2,1}$, ordered in decreasing absolute value. QTS5 adds to those harmonics the mode $B_{1,-1}$ and QTS6 includes also $B_{3,2}$. The modes B_{mn} with $n \neq 0$ are the responsible of breaking the toroidal-symmetry. The five magnetic configurations considered in this work, namely ITER, QTS4, QTS5, QTS6 and QTS72 are the same used in Ref [118] and though none of them are exact solutions of the original QTS VMEC equilibrium, they share the same dominant modes (by construction), have the same basic field structure and results in magnetic configurations with decreasing degree of quasi-toroidal symmetry σ_{qt}, shown in Figure 3.1 and defined as:

$$\sigma_{qt}(\psi) = \frac{\sum_{m=1}^{M} |B_{m0}(\psi)|}{\sum_{n=1}^{N} |B_{0n}(\psi)| + \sum_{m=1}^{M} \sum_{n=-N}^{N} |B_{mn}(\psi)|} \tag{3.1}$$

In the small gyroradius approximation, the motion of collisionless α-particles in the aforementioned magnetic configurations is described by the next two equations. One for the guiding center position $\mathbf{r}_g$

$$\dot{\mathbf{r}}_g = pv\frac{\mathbf{B}}{B} + \frac{mv^2}{2qB^3}(1+p^2)\,\mathbf{B}\times\nabla\mathbf{B} \tag{3.2}$$

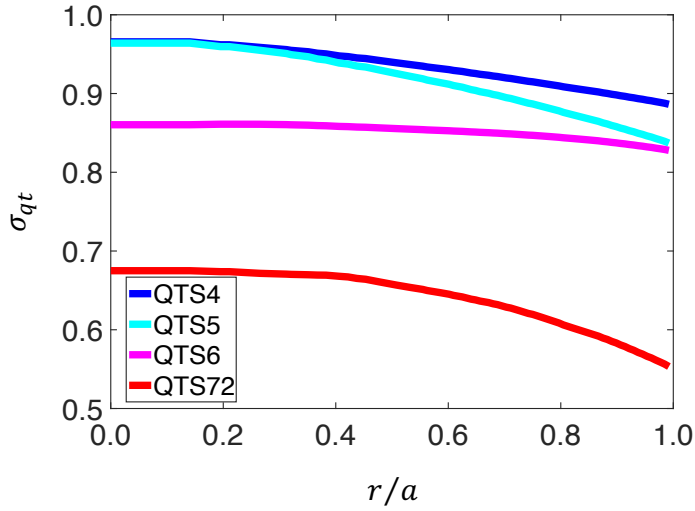

Figure 3.1: Quasi-toroidal symmetry ratio σ_{qt} for the four quasi-toroidal stellarators as a function of radial coordinate r/a.

and another for the pitch $p = v_{\parallel}/v$ (it should not be confused with the usual definition for the canonical momentum P)

$$\dot{p} = -\frac{v}{2B^2}(1-p^2)\mathbf{B}\cdot\nabla\mathbf{B} \tag{3.3}$$

where the dot implies derivative with respect to time, v and q are the speed and charge of the particle and $\mathbf{B}$ and B are the magnetic field and its magnitude. Notice that no equation is required for the evolution of the particle speed since electric field and collisional effects are neglected. These two equations reduce to a set of four coupled ordinary differential equations depending on the field strength $B(\psi,\theta,\varphi)$ and it derivatives with respect to the radial ψ, poloidal θ and toroidal φ spatial Boozer coordinates. For every magnetic configuration, the transport was modeled by an ensemble of α-particles, whose trajectories are simulated integrating this system of ODEs with the Monte Carlo code MOCA. A parallel FORTRAN code working in Boozer coordinates that uses a three-dimensional grid $N_\psi \times N_\theta \times N_\varphi \equiv 100 \times 360 \times 360$ per machine period to pre-store and interpolate the magnetic field magnitude and its derivatives using the Bulirsh-Stoer algorithm [107] to integrate particle trajectories.

In all simulations presented, α-particles are initialized at the half-

radius $r/a = 0.5$ with a fixed energy of 3.5 MeV. They are distributed uniformly in pitch and randomly in poloidal angle for ITER (65536 particles) and in poloidal and toroidal angles for the stellarator cases (262144 particles each). The random distribution used for the poloidal and toroidal angles has been chosen to be inversely proportional to the Jacobian, $1/J(\psi, \theta, \varphi) = (B(\psi, \theta, \varphi)/B_0)^2$, of the coordinate transformation to keep a uniform density on the flux surface in real space, thus initializing more particles in regions of higher magnetic field. The time step used, $\Delta t \approx 10^{-8}$ s, was the result of a trade-off between the orbit following code integration accuracy (measured with the relative change in particle energy during their lifetimes, which was kept below $\sim 10^{-5}\%$) and the total simulation time, which was chosen to ensure that no new *regimes* appear in the cumulative loss fraction of particles for any configuration, see Figure 3.2. The actual value used, $t = 10$ s was the result of a rather long simulation performed for QTS4 (the one with the expected longer saturation time) and suffices to guarantee that the *plateau* was fully achieved for QTS72 and QTS6 and fairly indicated for QTS5 and QTS4. All results were checked to be independent of the number of particles considered and the grid size and grid interpolation scheme applied to define the 3D magnetic field.

In all five configurations, particle trajectories can be broadly classified into two groups as those that keep or change their initial pitch sign, called *passing* and *trapped* respectively. Notice that the latter naming convention differs from the one commonly associated with the parallel dynamics in neoclassical theory [108, 109, 110]. In the quarter million particles used for the simulations, these two types of trajectories can be further subdivided into finer kinds of executed orbits [66]: passing, stagnation, potato, ripple trapped, bananas, ... and combinations between them since particles can change their orbits from one type to another during their lifetimes, even without considering collisions. Before trying to characterize α-particle transport, it is necessary to classify the fractions of the different types of particle trajectories and followed orbits since their confinement varies. For example, the average radial drift of collisionless passing and stagnation orbits is negligible compared to that of banana or ripple trapped orbits, mixing them in a unique analysis could contaminate the statistics and mask the transport dynamics of interest.

Firstly, we have calculated the cumulative fraction of loss particles, see Figure 3.2. For ripple-less ITER not even a single particle is lost

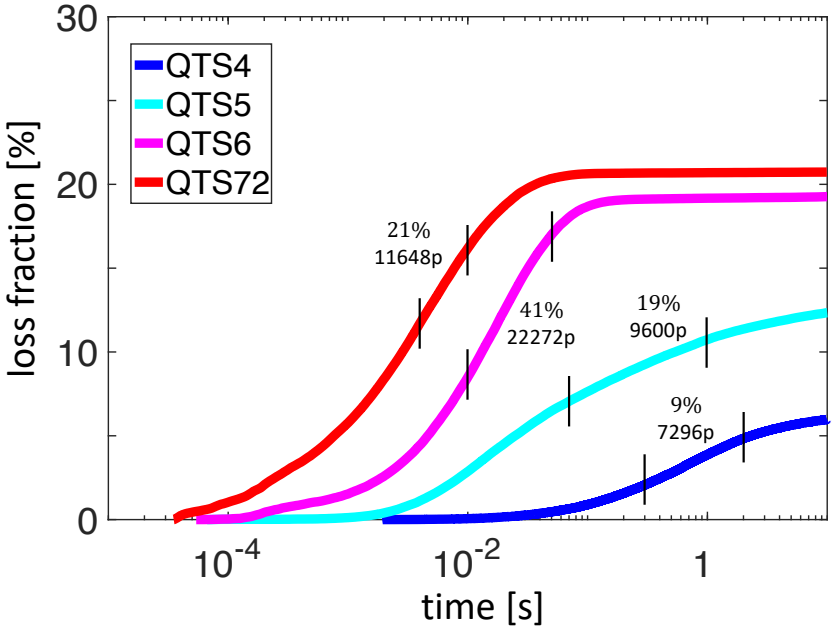

Figure 3.2: Loss fraction of α-particles over time for the four quasi-toroidal stellarators. Vertical lines indicate the exit-time range of the particles considered for the fractional transport analysis, whose number and percentage among trapped particles are given for each configuration, the first (left) vertical lines correspond to the simulation time of the selected α-particles.

during the simulation, which is also an efficient test to demonstrate the fairly low numerical diffusion of MOCA. For the four QTS configurations, the trend shows that the decrease in symmetry level leads to larger losses. This can be explained by the fact that confinement relies on ensemble average radial drifts. For a toroidally symmetric configuration, like ripple-less ITER, the radial average automatically cancels, but as soon as symmetry is broken, as for the other four configurations considered, the radial average rapidly increases. The different slopes in Figure 3.2 indicate that the particle escaping rates vary, contributing in different ways to the transport.

Secondly, particle orbits are classified in two basic types: trapped and passing, depending on whether they change, or not, the sign of their pitch respectively. We found that not a single passing particle

was lost for any configuration. While the fraction of trapped particles in ITER is $\sim$ 30% and all are perfectly confined, in the QTS configurations it is $\sim$ 20% and the lost fraction increases as the level of quasi-symmetry decreases. A study was done for the five configurations with a newly developed numerical procedure that classifies and characterizes particle orbits, based on the analysis of reflection points and the poloidal angle at which they cross (or not) the equatorial plane between consecutive reflection points. The analysis of all trapped particle trajectories in the five configurations shows that more than a 90% of their orbits are either bananas or ripple trapped. As an example, Figure 3.3 presents two trapped α-particle trajectories with adjacent initial conditions, where one escapes following solely banana orbits and the other eventually transitions its orbit to the ripple trapped. No further attempt was made to distinguish the other 10% of orbit types. More in detail, two limiting cases are found, on the one hand, ITER with 97% of bananas and zero ripple trapped orbits, and, on the other hand, QTS72 with 54% bananas and 35% ripple trapped orbits. The procedure also allows to estimate the width and center of banana orbits, see Ref. [118] for details and other orbit examples.

Lastly, with the aim to evaluate particle transport, it is necessary to select the kind of particles and time scales of interest for a given configuration. With this in mind, neither passing particles nor particles belonging to the saturation region in Figure 3.2 contribute to transport and, therefore, will be ignored together with the prompt losses, whose established *convective* behavior would only mask the results. To characterize the relevant transport parameters, the region with the steepest slope in the loss fraction is chosen; i.e. the range belonging to the largest fraction of particle losses. The analysis of Section 3.3 will be performed on the trajectories of all trapped particles which are lost in the interval marked with vertical black lines in Figure 3.2. The number of particles considered in each QTS configuration and their percentage among trapped particles are also indicated in the figure. Despite the fact that collisionless α-particles in ITER lack any kind of transport, a set consisting of $\sim 20,000$ trapped particles will be analyzed for testing purposes.

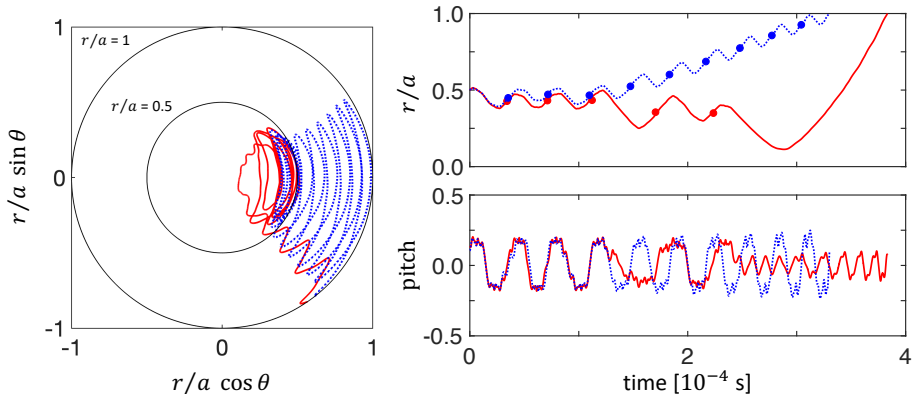

Figure 3.3: Left: poloidal projection of two trapped α-particle trajectories with adjacent initial conditions in Boozer coordinates for the QTS72 configuration from their initialization at $r/a = 0.5$ till their lost at $r/a = 1$. Blue/dashed trajectory follows only banana orbits, red/solid trajectory follows banana orbits and shortly after 0.2 ms becomes ripple trapped. Right: time evolution of the radial position r/a (top) and pitch (bottom) of the same trajectories. The centers of all the banana orbits are indicated by the circles (top).

3.3 Fractional transport diagnostics

In this section we will provide a brief introduction to the basics of the fractional transport equation and to some methods to estimate its exponents by means of tracked particles. These are the methods that will be used in the reminder of the paper to analyze the characteristics of the transport of α-particles.

3.3.1 Fractional transport equation and transport exponents

A well-known example of the mathematical relation between some macroscopic transport equations and certain features of its microscopic transport dynamics is the classical diffusion equation,

$$\frac{\partial n}{\partial t} = D\frac{\partial^2 n}{\partial x^2} \tag{3.4}$$

where D is the classical diffusion coefficient. Although the validity of this equation could be assumed ad-hoc, it can also be easily derived

from stochastic or probabilistic descriptions of the underlying microscopic transport process. For example, it can be obtained from the classical continuous-time random walk (CTRW) [20], that describes the motion of a population of walkers that execute jumps of length Δx after having waited at their current location for an amount of time Δt. The probability density distributions (pdfs) of steps, $p(\Delta x)$ and waiting times, $\psi(\Delta t)$ define the CTRW. Not every CTRW results in a macroscopic diffusion equation. But in the case of a symmetric CTRW (i.e., the jump pdf has zero mean), if both jumps and waiting-times are uncorrelated and have a well-defined associated scale, given by the (square-root of the) variance of step pdf, σ, and the mean of the waiting-time pdf τ. It is readily found that the motion of the microscopic walkers is well-described by equation 3.4 for long times and distances. In fact, $D \propto \sigma/\tau$. Mathematically speaking, these conditions translate into the need for the step-size pdf of being within the basin of attraction of the Gaussian distribution of the same variance, as dictated by the central limit theorem, and the waiting-time pdf to be in the basin of the exponential pdf with the same mean [120].

If the macroscopic transport exhibits features such as the presence of long temporal correlations or an apparent lack of characteristic scales, it should then be expected that equation 3.4 provides a poor description of the transport dynamics. It has been suggested by many authors that, in these cases, a more general transport equation is needed. One possibility is the fractional transport equation,

$$\frac{\partial n}{\partial t} = D_t^{1-\beta}\left[K\frac{\partial^\alpha n}{\partial |x|^\alpha}\right], \qquad 0<\beta<1,\ 0<\alpha<2, \tag{3.5}$$

where D_t^γ represents the fractional Riemann-Liouville operator of the order γ, K is a constant and $\partial^\alpha n/\partial|x|^\alpha$ is the Riesz fractional derivative of the order α [19]. Fractional operators are integro-differential equations so that the temporal fractional derivative integrates over the full history of the system, thus being able of including memory effects. Similarly, spatial fractional derivatives integrate over the whole system domain and can capture non-local effects.

The convenience of using fractional transport equations can be justified similarly to how we previously did for the classical diffusion equation. Starting with the usual CTRW, equation 3.5 can be obtained as its long-time, long-distance limit whenever one introduces the observed

lack of characteristic scales by choosing step-size pdfs with diverging variance, (i.e., $p(\Delta x) \sim \Delta x^{-(1+\alpha)}$, $0 < \alpha < 2$) and waiting-time pdfs with divergent means (i.e., $\psi(\Delta t) \sim \Delta t^{-(1+\beta)}$, $0 < \beta < 1$) [21]. Mathematically, this is again tantamount to choosing them from within the basin of attraction of the proper subfamily of Lévy pdfs [120] as dictated by the generalized central limit theorem.

The exponents α and β in equation 3.5 are known as fractional transport exponents. In the limit $\alpha \to 2$ and $\beta \to 1$, the usual classical diffusion equation is recovered. However, if $\alpha < 2$, non-local spatial effects are relevant. Similarly, if $\beta < 1$, memory effects are essential in determining future transport. It is also common to define a third exponent, $H \equiv \beta/\alpha$, known as the Hurst exponent [121]. For the diffusive case, $H = 1/2$. Therefore, any equation with $H > 1/2$ is usually referred to as superdiffusive, and subdiffusive if $H < 1/2$. These transport dynamics has very interesting features. For instance, perturbations can spread in them very quickly (superdiffusion) or extremely slowly (subdiffusion). In the former case, they can resemble avalanche-like transport while in the latter, they may exhibit extreme stickiness. For that reason, they are used to model transport in situations in which these features are known to exist [21, 111].

The best manner to test whether equation 3.5 provides a good model for transport in any system is to estimate the values of the fractional transport exponents that best reproduced its observed transport features. There are a few methods to do this, most of them based on specific features of equation 3.5 and its propagator, $P(x,t)$. The propagator of any differential equation is the temporal evolution of its initial conditions. Or, in other words, the probability of finding at time t a particle at position x if it was initially at x_0. Values of the fractional exponents that best model transport in any system can then be obtained with relative ease by comparing the propagator of equation 3.5 with some numerical reconstruction of the propagator in the system of interest, usually by employing tracked or tracer particles. A review of many of these techniques can be found elsewhere [43], but we will focus on two of them in what follows.

3.3.2 The Eulerian method

The Eulerian method relies on exploiting some scaling properties of the propagator of equation 3.5. In particular, it can be shown that,

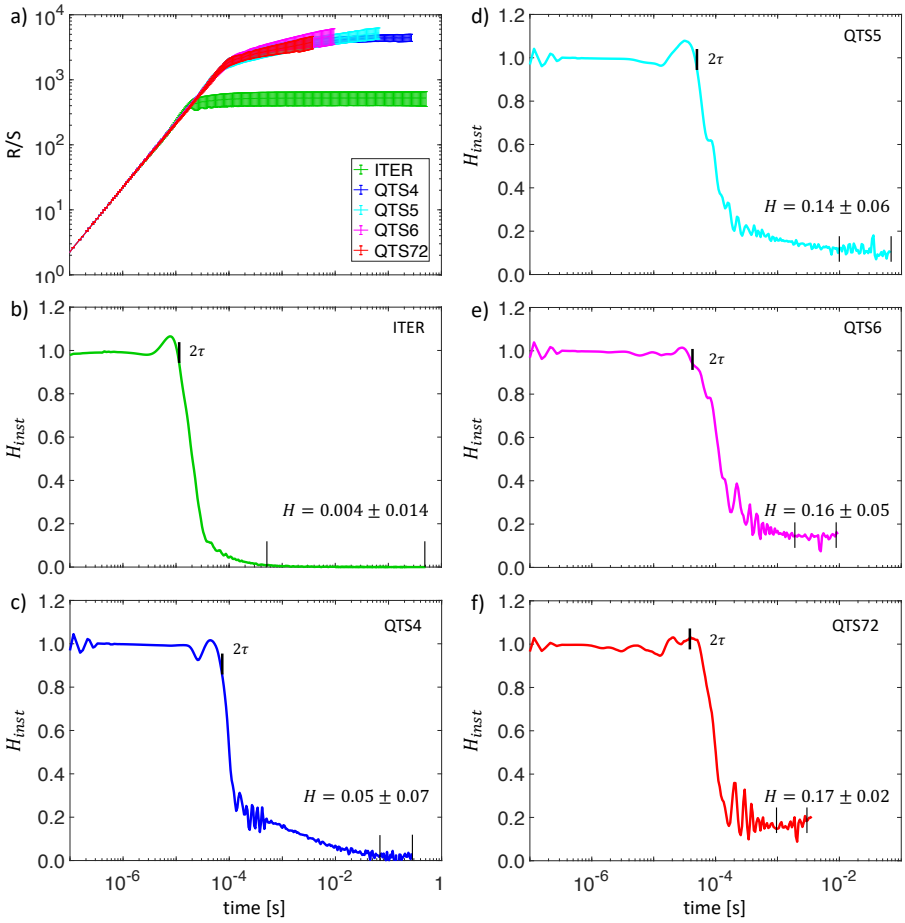

Figure 3.4: Rescale range analysis (a) and instantaneous Hurst exponent, $[R/S] \sim \tau^H$, for ITER (b), QTS4 (c), QTS5 (d), QTS6 (e) and QTS72 (f), τ_b is the characteristic bouncing time. Vertical lines indicate fitting range, i.e. the mesoscale, for the resulting Hurst exponent H.

for fixed time t_i the propagator scales as [96, 26]:

$$P(x, t_i) \sim |x - x_0|^{-(1+\alpha)}, \qquad |x - x_0| \gg K^{1/\beta} t_i^{\beta/\alpha} \tag{3.6}$$

from where α could be found by fitting the tail of the propagator $P(x, t_i)$ to a power law in log-log scale. The derivative of the propa-

gator at fixed time gives the local spatial exponent:

$$\alpha(x) = -\left[1 + \frac{x}{P(x)}\frac{\mathrm{d}P}{\mathrm{d}x}\right] \tag{3.7}$$

that should come out to be rather independent of x (or at least over a sufficiently long range) to be meaningful.

To apply this method to our system of interest, one could follow a population of N tracked particles in time, record their trajectories $x_j(t),\ j = 1, \cdots, N$, and then build an approximation of the propagator simply by building the probability density function of $x_j(t) - x_j(0)$. The tail of the resulting pdf, at sufficiently long times, should behave as equation 3.6 if the fractional transport equation does provide a reasonable model for transport in the system.

The temporal exponent, β, can be estimated in a similar way using another scaling property of the propagator of equation 3.5. For any fixed location, x_i, that is sufficiently far from x_0 the propagator scales as [96, 26]

$$P(x_i, t) \sim t^{\beta}, \quad t \ll K^{1/\beta} x_i^{\alpha/\beta}, \tag{3.8}$$

and,

$$P(x_i, t) \sim t^{-\beta}, \quad t \gg K^{1/\beta} x_i^{\alpha/\beta}. \tag{3.9}$$

Thus, one could in principle estimate β by following in time the value of the numerical propagator, constructed as we discussed earlier, at any fixed location.

The Hurst exponent can be estimated as the ratio $H = \beta/\alpha$ once their values are available from the determinations previously described. But it can also be estimated directly from the numerical propagator. Indeed, yet another property of equation 3.5 is that all finite moments of its propagator satisfy,

$$\int |x - x_0|^{\mu} P(x, t_i)\mathrm{d}x \propto t^{\mu H}, \qquad 0 < \mu < \alpha. \tag{3.10}$$

Since the determination of β is usually the most challenging one from a practical point of view, it is sometimes preferable to determine H using equation 3.10, and then infer it via the relation $\beta = \alpha H$.

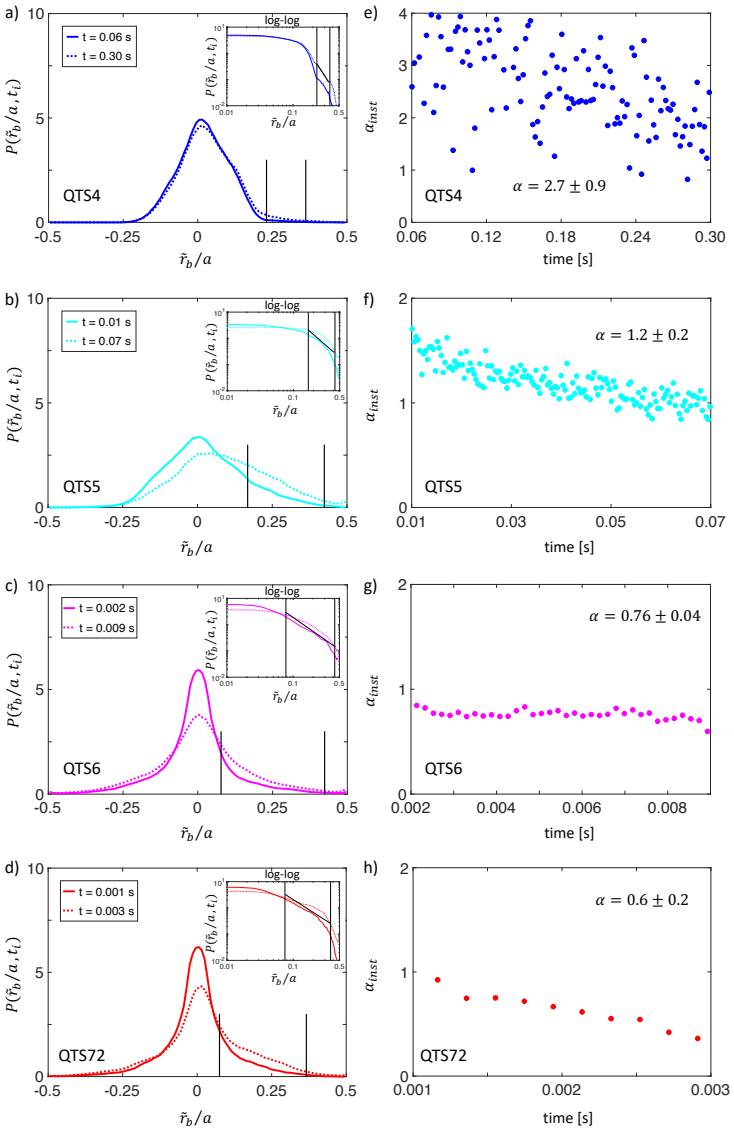

Figure 3.5: Left: Propagator constructed as density function of normalized banana centers $\tilde{r}_b/a$ at the beginning and end of the *mesoscales* for QTS4 (a), QTS5 (b), QTS6 (c) and QTS72 (d) in linear and logarithmic scales. Vertical lines indicate fitting range for the exponent α. Right: Instantaneous spatial exponent and its averaged over the mesoscale value α for QTS4 (e), QTS5 (f), QTS6 (g) and QTS72 (h).

3.3.3 The Lagrangian method: R/S analysis

There is another way to estimate H that does not require the calculation of the numerical propagator, but that can be directly inferred from the analysis of the trajectories of individual tracked particles or, more precisely, their instantaneous velocities [30]. In particular, H can be obtained by performing the so-called rescaled range analysis [121] on the velocity of each particle, and then averaging over as many particles as are available. The procedure for a single particle is to consider the velocity series $\{V_k = x_{k+1} - x_k \ , k = 1, 2, \ldots, N\}$ of each tracked particle, and calculate its rescaled range at iteration $k = \tau$ using:

$$[R/S](\tau) = \frac{\max\limits_{1\leq k\leq \tau} W(k,\tau) - \min\limits_{1\leq k\leq \tau} W(k,\tau)}{(\langle V^s\rangle_\tau - \langle V\rangle_\tau^s)^{1/s}} \tag{3.11}$$

where,

$$W(k,\tau) = \sum_{i=1}^{k} V_i - k\langle V\rangle_\tau \tag{3.12}$$

and $\langle\cdot\rangle_\tau$ represents the average up to iteration τ. The denominator is the fractional standard deviation of order $0 < s < \alpha$ [31]. If transport is indeed scale-free and governed by an equation similar to equation 3.5, one should find that $[R/S] \sim \tau^H$ (with $H = \beta/\alpha$) over a meaningful range of times [30], from which the fractional exponent H can be inferred. It is also possible to determine the instantaneous Hurst exponent via:

$$H(\tau) = \frac{\tau}{[R/S](\tau)} \cdot \frac{\mathrm{d}[R/S]}{\mathrm{d}\tau}(\tau), \tag{3.13}$$

that should be rather independent of τ, at least over a sufficiently large range, to be meaningful.

3.3.4 On the sensitivity and validity of methods

To what extent can one trust the results of the previous analysis to estimate transport exponents? First of all, any scaling exponent will only be meaningful if it remains valid over a sufficiently large range of the relevant scale, usually referred to as *mesoscale*. It is difficult to define what "sufficiently large" is in most cases, but we would require at least half, if not a full decade.

Secondly, the methods previously described can be proved to yield the same results only for equation 3.5, that exhibits scale-invariance for all scales. This is not the case in any real system, that will exhibit scale-invariance at best for a finite range of scales. In that situation, the values obtained with the different methods may vary. In fact, the Eulerian and Lagrangian methods have different sensitivities. Any method based on propagators usually is quite sensitive to finite-size effects, particularly if the system size is not too large. Rescaled-range analysis is usually much more robust, being rather insensitive to the presence of boundaries as well as other noise sources, but feels the presence of any periodic contamination rather strongly. It also tends to work best at values of $H \sim 0.5$, but somewhat overestimates the exponent for $H < 0.3$ and underestimates it for $H > 0.8$ [43]. It is important to be aware of these limitations when interpreting the obtained values of transport exponents while using the aforementioned methods.

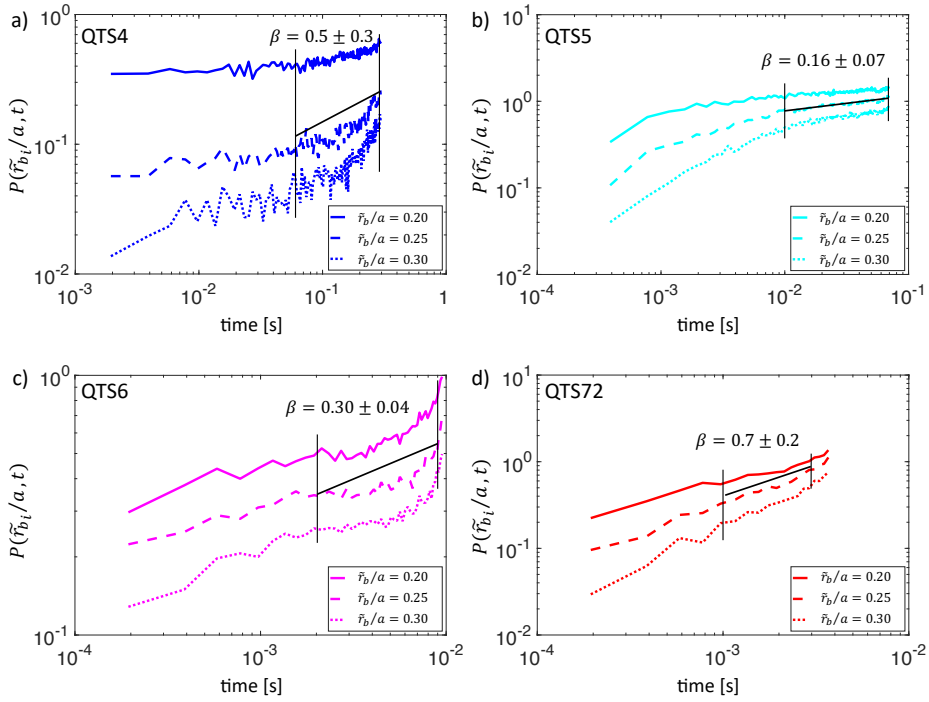

Figure 3.6: Propagator of the banana centers for three fixed radial positions and averaged temporal exponent β fitted over mesoscale for QTS4 (a), QTS5 (b), QTS6 (c) and QTS72 (d).

3.4 Results

We analyzed a set of trapped α-particles for QTS configurations, whose exit-times are marked by the vertical lines in Figure 3.2, where the first (left) vertical lines correspond to the simulation time of the selected α-particles being 0.004 s, 0.01 s, 0.07 s and 0.3 s for QTS72, QTS6, QTS5 and QTS4, respectively, before losses occurs to avoid any biasing (particularly to avoid contaminating the statistics by ripple trapped orbits, which have convective behaviour at the end of particle lifetimes). For ITER we characterized all trapped particles $\sim 20,000$ for half a second since they are perfectly confined. The Lagrangian Rescale range $[R/S]$ diagnostic described in Section 3.3 was performed using $r_g^{k+1} - r_g^k$ as V_k in equation 3.11, which is proportional to the radial guiding center speed $\dot{r}_g$. On the other hand, the Eulerian technique was performed by constructing the propagator of the banana centers , $P(\tilde{r}_b/a, t)$, as $x - x_0 = \tilde{r}_b/a$. Here $P(\tilde{r}_b/a, t)$ is the probability density function of the normalized radial displacements of the banana orbit centers with respect to their initial positions at time t. This is done because the dynamics of the guiding center radial transport and the banana-centre motion are different for times shorter than the average banana orbit time, but become identical at longer times scales. The reason is that a banana-centre barely moves during the banana orbiting, while the guiding centre is moving back and forth in radius, as it follows the banana. The relevant transport dynamics happen in the mesoscale range, which is well beyond the banana orbit time. In the calculation of the Hurst exponent, the coexistence of these two process at different timescales does not really alter the procedure, since they appear separated at different scaling ranges. For the calculation of the propagator, however, the two processes become more mixed, since the propagator calculated with guiding centres will be significantly deformed at the earlier timescales due to the back and forth motion, making more complicated the analysis at longer timescales. This distortion can be easily removed by considering only the banana center motion. Moreover, the displacement is computed with respect to its initial position instead from the position at the beginning of the mesoscale range since the calculation is approximately invariant under time-translations and it is difficult to specify the start of the mesoscale. The Eulerian method was applied solely for the QTS configurations due to the lack of any radial propagation of these orbits and the ab-

sence of stochastic tip diffusion [60] in perfectly axisymmetric ITER. The resulting transport exponents were estimated over the mesoscale range (indicated in all following figures).

3.4.1 The Lagrangian method: R/S analysis

The $[R/S]$ functions for the five configurations under consideration (all calculated with a fixed parameter $s = 0.3$ in equation 3.11 for consistency with the Eulerian method as $0 < s < \alpha$) are shown in the top left plot of Figure 3.4. The fact that the $[R/S]$ function changes its slope in ITER five times faster compared to the results for the four stellarators is pointing out to their quite different transport time scales. This can be more clearly seen in the instantaneous Hurst exponents obtained according to equation 3.13 and also shown in Figure 3.4. The sharp drop from the ballistic phase with $H = 1$ should be related to the underlying banana orbits. Indeed, the steep plunge in H occurring at ~ 10 μs for ITER and between 40 and 60 μs for the stellarators corresponds to the time necessary to complete one full banana orbit, $2\tau_b$ (i.e. two bouncing times), estimated according to the connection lengths of the magnetic field lines Ref. [118]. Moreover, the difference between these values and the oscillations seen after the decay around $\gtrsim$100 μs can be attributed to helically trapped orbits with longer connection lengths and slower bouncing times.

The Hurst exponent was estimated as the average of the instantaneous H over the region where it stabilizes, i.e. the mesoscale, bounded by the vertical lines in Figure 3.4. The result for ITER, where $H \sim 0$, suggests pure intermittency, being a typical characteristic of harmonic functions and confirming that the *frozen* bananas in ITER lack radial displacements. The modest values of H for the stellarators point to subdiffusion with the clear trend of increasing Hurst exponent for decreasing level of toroidal symmetry, but always staying way below the diffusive threshold of $H = 0.5$.

3.4.2 The Eulerian method

In the absence of the radial propagation of trapped particles in ITER, the Eulerian method was applied only to the four QTS stellarators. To estimate all three fractional exponents for each configuration, we choose the same fitting range, i.e. the mesoscale, as the one used

in the $[R/S]$ calculations of the previous subsection, see Figure 3.4. The fractional spatial exponent α was obtained by fitting the tail of the propagator at fixed times $P(\tilde{r}_b/a, t_i)$ to a power law according to equation 3.6. The propagator at the beginning and the end of the mesoscale is presented in the left plots of Figure 3.5 both in linear and logarithmic scales (in log-log scale the resulting power law fit is given by a tilted black line in between the vertical bars). The slight radial asymmetry of the spatial propagators is due to the inhomogeneity of the magnetic field, that makes radial displacements towards the inside and the outside not completely symmetric. The results show an increasing variation of $P(\tilde{r}_b/a, t_i)$ with decreasing level of quasi-toroidal symmetry. The instantaneous spatial transport exponents $\alpha_{inst}(t)$ are presented in the right plots of Figure 3.5 and obtained by fitting to a power law the propagator, $P(\tilde{r}_b/a, t_i) \sim \tilde{r}_b/a^{-(1+\alpha)}$, from the beginning until the end of the mesoscale in the spatial regions marked by vertical lines on the left plots. The very small difference in $P(\tilde{r}_b/a, t_i)$ for QTS4 during such long period corresponds to the the very narrow saturation range in the $[R/S]$, see Figure 3.4 (c), and translates in a large dispersion of $\alpha_{inst}(t)$ for this configuration. The large variation of α_{inst} for QTS72, varying from around 0.9 to 0.3, makes the results rather unreliable. Besides these difficulties, there is a clear trend in reducing α from around 2.7 to 0.6 as the quasi-toroidal symmetry decreases.

The Eulerian technique can also be used to obtain the fractional transport exponent associated with the temporal dependence, β, by fitting the time decay of the propagator $P(\tilde{r}_{b_i}/a, t)$ according to equation 3.8. We choose three radial positions, $\tilde{r}_{b_i}/a = 0.20$, 0.25 and 0.30, corresponding to the center of the regions used in estimating α enclosed by vertical lines on the left plots in Figure 3.5. The temporal exponent β was calculated by averaging the three values obtained from fitting $P(\tilde{r}_{b_i}/a, t) \sim t^{\beta}$ over the mesoscale, likewise, being delimited with vertical bars in Figure 3.6 together with the resulting power law fit given by a tilted black line in between the bars. The values estimated for QTS5 and QTS6 are $\beta \sim 0.2$, while the results for QTS4 and QTS72 are significantly larger $\beta \sim 0.5 - 0.7$, however, the standard deviations for them are larger as well.

Finally, it is possible to estimate the Hurst exponent from the time dependence of the fractional standard deviation σ using equation 3.10, i.e. the finite moment of the propagator of order less than α, according

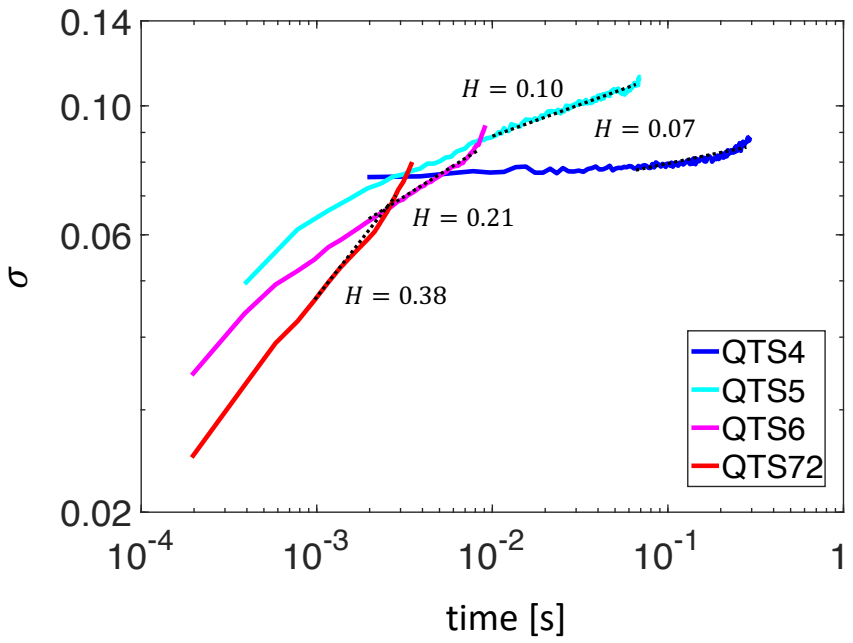

Figure 3.7: Fractional standard deviation σ and the fitted over the mesoscale (indicated by dashed lines) Hurst exponent for the four stellarators.

to the results depicted in Figure 3.6. The resulting fractional standard deviation is presented in Figure 3.7 in log-log scale along with the power law fit of H over the mesoscale and is calculated with $\mu_{QTS4} = 1.5$, $\mu_{QTS5} = \mu_{QTS6} = 0.5$ and $\mu_{QTS72} = 0.2$ each satisfying $\mu < \alpha$. As it was found previously by an alternative $[R/S]$ method, Hurst exponents increase as the stellarator configuration departs from quasi-toroidal symmetry but without exceeding the diffusive limit in $H = 0.5$ even for QTS72.

As a final part of our study, we also performed a rescaling of the propagator using the obtained fractional coefficients to confirm its good self-similar properties. A function $f(x)$ is called self-similar if $f(\lambda x) = \lambda^{-\gamma} f(x)$, where γ is called self-similarity exponent. In seeking for the self-similarity signatures of the propagator, we constructed the renormalized distribution $t^{\gamma} P(\tilde{r}_b/a, t)$, where as gamma we used either $\gamma = \beta/\alpha$ or $\gamma = H$ and plotted it as a function of the scaling variable $(\tilde{r}_b/a)/t^{\gamma}$ for the two time instances corresponding to the be-

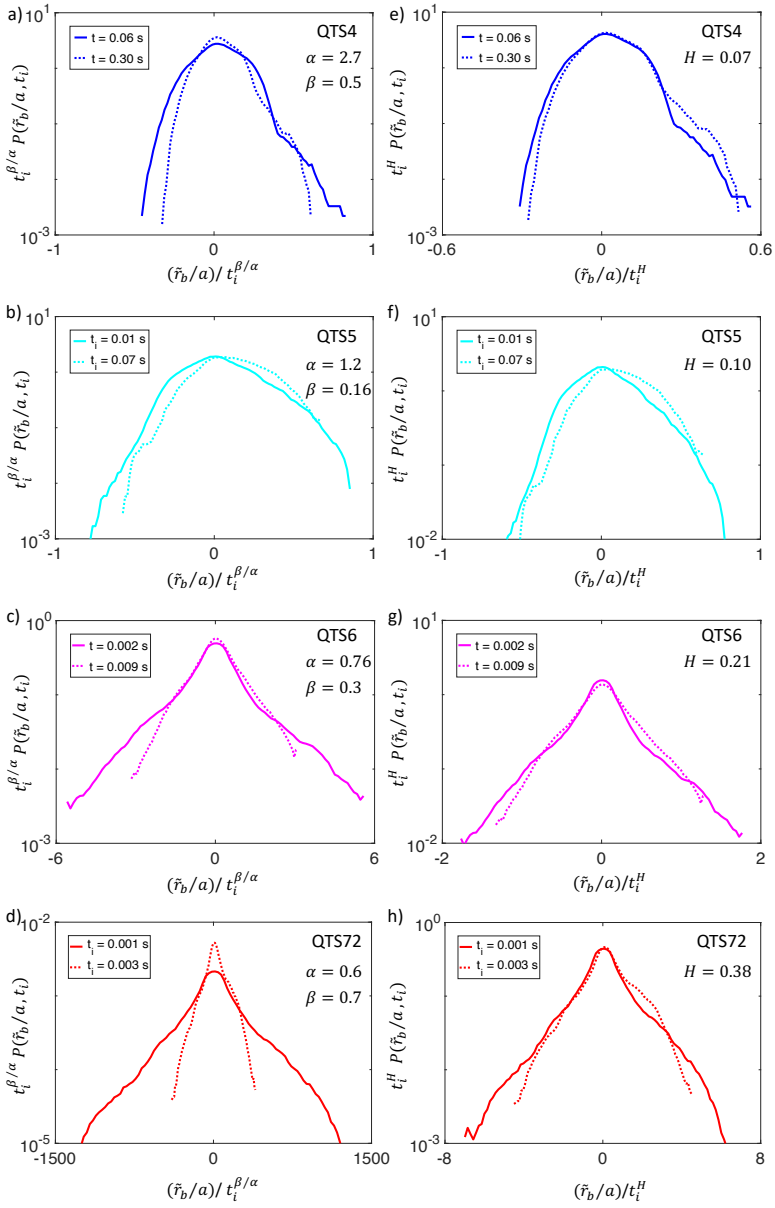

Figure 3.8: Left: The renormalized distribution as a function of the similarity variable with $\gamma = \beta/\alpha$ for QTS4 (a), QTS5 (b), QTS6 (c) and QTS72 (d) in a log-linear scale. Right: The renormalized distribution as a function of the similarity variable with $\gamma = H$ for QTS4 (e), QTS5 (f), QTS6 (g) and QTS72 (h) in a log-linear scale.

ginning and end of the mesoscale, see Figure 3.8 in a log-linear scale. In both cases, the distributions are far from having a Gaussian shape. However, the pdfs begin to resemble the parabolic profile with an increasing level of quasi-symmetry, which is also reflected by the increase of the estimated spatial exponent α that gradually approaches the value of two. In the limiting case of low symmetry for QTS72, the results with $\gamma = \beta/\alpha > 1$ are not reliable, while the results with $\gamma = H$ seem to be more trustworthy.

3.5 Discussion and Conclusions

The trajectories of collisionless trapped α-particles dictated by neoclassical theory for five magnetic configurations with different levels of toroidal symmetry have been analyzed with fractional transport tools to determine the effective nature of radial transport. The $[R/S]$ analysis applied to the perfectly confined trapped particles of the purely axisymmetric ITER tokamak results in a Hurst exponent $H = 0.004 \pm 0.014$ indicating ideal intermittency and the absence of radial transport. For this case, the Eulerian analysis becomes not feasible. The resulting Hurst exponents for the quasi-toroidal stellarators estimated by both the Lagrangian and the Eulerian techniques agree within the error bars except for QTS72, see Table 3.1. This is possibly a consequence of its fast losses and the importance of finite size effects since propagator based estimations are quite sensitive to them, particularly if the system size is not too large. The values clearly suggest a subdiffusive transport behavior that becomes more pronounced as the level of quasi-toroidal symmetry increases.

The values of the spatial exponent α strongly decrease with decreasing symmetry and point to the presence of spatial correlations and the non-local nature of transport for these configurations. One might infer that the spatial exponent $\alpha = 2.7 \pm 0.9$ for QTS4 implies Gaussian statistics, but it is rather an artifact due to small broadening caused by the reduced average drifts for its highly quasi-toroidal symmetry. Additionally, in all cases the value of H stays well below $1/\alpha$, thus revealing the presence of strong anti-correlations [120].

The temporal exponent β deduced from the propagator analysis, see Table 3.1, shows a large disparity between QTS5/QTS6 configurations where $\beta \sim 0.2-0.3$, and the limiting cases of high/low symmetry

	Lagrangian	Eulerian			
	H	H	α	β	$\beta = H * \alpha$
ITER	0.004 ± 0.014				
QTS4	0.05 ± 0.07	0.07	2.7 ± 0.9	0.5 ± 0.3	0.18 ± 0.06
QTS5	0.14 ± 0.06	0.10	1.2 ± 0.2	0.16 ± 0.07	0.12 ± 0.02
QTS6	0.16 ± 0.05	0.21	0.76 ± 0.04	0.30 ± 0.04	0.16 ± 0.01
QTS72	0.17 ± 0.02	0.38	0.6 ± 0.2	0.7 ± 0.2	0.24 ± 0.06

Table 3.1: Transport exponents obtained by the Lagrangian and Eulerian techniques for the five configurations.

in QTS4/QTS72 with $\beta \sim 0.5 - 0.7$. As it was mentioned at the end of Section 3.3.2, the more reliable technique to obtain β is by using H and α values via $\beta = H\alpha$. As shown in the last column of the Table 3.1, this technique offers values of $\beta \sim 0.2$ for the four QTS configurations. A reason for the large disparity between the QTS configurations estimated by the first technique (the propagator) could be related to the radial particle drifts. In particular, the β estimation may not be suitable for relatively slow particle drifts in QTS4 and, conversely, for fairly fast particle drifts in QTS72. On the other hand, both techniques are in good agreement for the QTS5 and QTS6 stellarators. In any case, the values of β for all configurations stay below 1 indicating a significant non-Markovian transport.

The difficulties encountered for QTS72 are a consequence of the fast losses due to its broken symmetry, which leads to short trajectories and a short range for the power law fits of $P(\tilde{r}_b/a, t)$ that can not capture the dynamics of α-particles in configuration accurately. On the other extreme is QTS4, whose high toroidal symmetry results in a minute variation of $P(\tilde{r}_b/a, t)$ leading to a large dispersion in the transport exponents. In between for QTS5 and QTS6, the resulting values of the transport coefficients appear to be quite robust and consistent, considering both the Hurst exponents obtained by the Lagrangian and Eulerian methods and the β values estimated by the two techniques.

The results of our collisionless α-particle simulations, within the approximations used and the quasi-toroidally symmetric configurations examined, suggest that an increasing departure from quasi-toroidal symmetry results in faster and larger neoclassical losses. The analysis with fractional transport theory tools indicates that the transport of

trapped but not prompt lost particles is non-Gaussian, non-Markovian and strongly subdiffusive. Moreover, fractional transport coefficients describe transport as becoming more subdiffusive as the level of the quasi-toroidal symmetry increases, which is similar to the results of Ref. [36] for supercritical turbulent transport in the presence of quasi-poloidal symmetry. Although, the validity of the fractional model itself becomes doubtful in the limiting cases of high and low symmetry.

Acknowledgements

This work was supported in part by the Spanish project ENE2012-33219, the project SIMTURB-CM-UC3M from the Convenio Pluri-anual Comunidad de Madrid, Universidad Carlos III de Madrid and the Erasmus Mundus Program: International Doctoral College in Fusion Science and Engineering FUSION-DC. Part of this research was carried at the Max-Planck Institute for Plasma Physics in Greifswald (Germany), whose hospitality is gratefully acknowledged. MOCA calculations were done in Uranus, a supercomputer cluster located at Universidad Carlos III de Madrid and funded jointly by EU-FEDER and the Spanish Government via Project No. UNC313-4E-2361, ENE2009-12213-C03-03, ENE2012-33219 and ENE2015-68265.

Chapter 4

Conclusions

This thesis considered the relation between the collisionless α-particles transport and the toroidal symmetry level of the magnetic field and addressed the nature of the underlying processes.

The statistical analysis of the α-particles transport was performed based on ensemble average of a large set of guiding center trajectories obtained numerically with the Monte Carlo code MOCA. Three approximations conforming to fusion relevant α-particles were made: the small gyroradius ordering, neglecting the electric field and ignoring the collisions with other particles.

The study considered five reactor-scale configurations: a ripple-less ITER tokamak and four quasi-toroidally symmetric (QTS) stellarators loosely based on the NCSX project. These configurations are characterized by a newly developed quasi-toroidal symmetry figure of merit σ_{qt}, which is $\sigma_{qt} = 1$ for the purely toroidally symmetric ITER configuration and ranges from $\sigma_{qt} = 0.94$ to 0.62 for the QTS stellarator configurations.

For each configuration, we analyzed the α-particles losses and their dependence on the particle birth positions. The α-particle trajectories were classified as being either passing or trapped, and their fractions were estimated by two methods: one based on particle trajectories and the other on the magnetic well depth. A newly developed numerical procedure classified trapped orbits as mostly being bananas and to a lesser extent potato, ripple trapped and transition. For ITER, the ratio of passing to trapped particles is $\sim 70/30$, all of them are perfectly confined and where 97% of the trapped fraction are banana orbits. For the QTS configurations, the ratio is $\sim 80/20$ but some

trapped particles got lost. A departure from QTS results in faster and larger losses, being the limiting case QTS72 where almost all trapped particles escape and whose orbits are 54% bananas and 35% ripple trapped. As expected, most of those losses belong to particles being born with small pitch at regions of low magnetic field at the outer midplane.

These are precisely the trapped α-particles that are mainly responsible for transport, for this reason, a novel algorithm was developed to define the trapped orbit center and its other characteristic orbit parameters, i.e. bouncing times τ and widths Δw, from their trajectories. It was shown that the decrease in the toroidal symmetry level results in particle trajectories with wider banana orbits and longer bouncing times (the most probable values are in the range of $\Delta w \sim 0.15 - 0.25$ and $\tau \sim 20 - 30$ μs). These results were corroborated by an independent numerical procedure based on connection lengths along the field lines.

Convective velocities and diffusion coefficients were estimated using the characteristic bouncing times τ and widths Δw and by fitting the time dependence of the moments of the radial probability distribution function with the running moments method. Large discrepancies were found between both methods, e.g. $D \sim 2 \times 10^4$ m^2/s using the first and $D \sim 10^{-2}$ m^2/s using the second for the QTS4 configuration.

These results question the validity of the classical convection/diffusion model to adequately describe the collisionless trapped α-particle transport for the magnetic configurations considered.

Inspired by the success of the fractional transport theory to build an effective transport model for turbulent driven transport in fusion plasmas, we implemented its tools to determine the effective nature of the ripple-enhanced α-particle radial transport. The fractional transport coefficients, i.e. the Hurst H, the spatial α and the temporal β exponents, were estimated with the Eulerian and Lagrangian techniques (the propagator and the $[R/S]$ analysis respectively) using the trajectories of trapped α-particles for the same five configurations.

Both the Eulerian and the Lagrangian analyses reveal that the transport of collisionless trapped α-particles has non-diffusive features being non-Gaussian, non-Markovian and strongly subdiffusive.

As expected, the perfectly confined trapped particles of the rippleless ITER configuration are characterized by the absence of radial transport with almost zero Hurst exponent, $H = 0.004 \pm 0.014$. For

the quasi-toroidal stellarators, the values of the Hurst exponents estimated by both the Eulerian and Lagrangian methods were found to be in agreement, clearly suggesting a strong subdiffusive character of transport, which becomes more pronounce as the level of quasi-toroidal symmetry increases. Only for the QTS72 configuration, the resulting Hurst exponents did not agree within the error bars, a consequence of its fast losses and finite size effects.

For the four stellarators, the resulting spatial exponents α point out to the non-Gaussian statistics and non-local nature of transport. The values of α strongly decrease with decreasing symmetry, moreover, the inverse of it, $1/\alpha$, never exceeds the estimated Hurst exponents, revealing the presence of strong spatial anti-correlations. The atypical value of $\alpha_{QTS4} = 2.7 \pm 0.9$ rather than being an indicator of Gaussian statistics, might be an artefact due to the reduced spatial drifts, to which the Eulerian technique is more sensitive.

The temporal exponents, β, obtained by the Eulerian method indicate a significant non-Markovian transport behaviour and the corresponding relevance of memory effects. Despite a large disparity between $\beta_{QTS5/QTS6} \sim 0.2 - 0.3$ and $\beta_{QTS4/QTS72} \sim 0.5 - 0.7$ was found, all values of β stay below 1. These results were compared with a more reliable technique that estimates β based on H and α as $\beta = H\alpha$, which offered $\beta \sim 0.2$ for the four QTS configurations.

The main results of this thesis show that the collisionless trapped α-particle transport cannot be adequately described by the classical convection/diffusion approach for the quasi-toroidally symmetric configurations considered, whereas the fractional transport theory can provide an effective transport model. The fractional transport coefficients indicate that the transport is non-diffusive being non-Gaussian, non-Markovian and strongly subdiffusive. As the level of the quasi-toroidal symmetry increases, the ripple-enhanced transport of α-particles becomes strongly subdiffusive. Although, the validity of the fractional model itself becomes doubtful in the limiting cases of high and low symmetry.

The work presented here could naturally be expanded to: i) examine the validity of the fractional transport model onto other types of quasi-symmetric or isodynamic configurations, ii) clarify if the non-diffusive description is still necessary when collisions are considered, iii) study the effects of density, temperature and α-particle birth profiles, iv) consider resonant and non-resonant MHD instabilities, etc.

Chapter 5

Conclusiones

Esta tesis ha considerado la relación entre el transporte de las partículas α no colisionales y el nivel de simetría toroidal del campo magnético, abordando la naturaleza subyacente de estos procesos.

El análisis estadístico del transporte de las patículas no colisionales se llevó a cabo empleando un amplio conjunto de trayectorias de su centro guia, calculadas con el código Monte Carlo MOCA. Para ello se han realizado tres aproximaciones, que se ajustan a las condiciones de las partculas α en reactores de fusion, se supone que tanto el radio de Larmor como el efecto del campo eléctrico y de las colisiones con otras partículas son despreciables.

El estudio ha considerado cinco configuraciones con tamaño de reactor: un tokamak sin *ripple* similar a ITER y cuatro stellarators simétricos cuasi-toroidales basados vagamente en el proyecto NCSX. Estas configuraciones se caracterizan por σ_{qt}, una nueva figura de mérito para cuantificar el nivel de simetría cuasi-toroidal que hemos desarrollado, que es $\sigma_{qt} = 1$ para configuraciónes con simetría toroidal pura como la ITER y varía entre $\sigma_{qt} = 0.94$ y 0.62 para las configuraciones los stellarators QTS.

Para cada configuracíon, hemos analizado las pérdidas de las partículas α y su dependencia con la posición de nacimiento. Las trayectorias de las partículas α fueron clasificadas como pasantes o atrapadas y sus fracciones se estimaron mediante dos métodos: uno basado en la trayectoria de las partículas y otro en la profundidad del pozo magnético. Un procedimiento mumérico desarrollado por primera vez clasificó estas órbitas atrapadas como principalmente bananas, y en menor como órbitas *potatoes*, *ripple trapped* y en tránsito. Para ITER,

la proporción entre partículas pasantes y atrapadas es de $\sim 70/30$, y todas ellas están perfectamente confinadas, y donde el 97% de las partículas atrapada son órbitas banana. Para las configuraciones QTS, la proporción es $\sim 80/20$ pero algunas partículas atrapadas se fugan. La ruptura de la simetría quasi-toroidal QTS resulta en pérdidas mayores y más rápidas, siendo QTS72 el caso limíte, donde casi todas las partículas atrapadas escapan, y cuyas órbitas son 54% bananas y 35% *ripple trapped*. Como se esperaba, la mayoría de estas pérdidas pertenecen a partículas nacidas con un ángulo de ataque pequeño en regiones de campo magnético bajo en la zona externa del plan ecuatorial.

Las partículas α atrapadas son precisamente las principales responsables del transporte, por esta razón desarrollamos un nuevo algorítmo para definir el centro de la órbita atrapada y otros parámetros característicos de su órbita, como sus tiempos de rebote τ y sus anchuras Δw, a partir de sus trayectorias. Se demostró que la disminución en el nivel toroidal de simetría resulta en trayectorias de partículas con órbitas bananas más anchas y tiempos de rebote más largos (cuyos valores más probables fluctúan entre $\Delta w \sim 0.15 - 0.25$ y $\tau \sim 20 - 30$ μs). Estos resultados fueron corroborados por un procedimiento numérico independiente basado en las longitudes de conexión a lo largo de las líneas del campo.

Las velocidades convectivas y los coeficientes de difusión se estimaron usando los tiempos de rebote característicos τ y las anchuras Δw y ajustando la dependencia tiemporal de la función de distribución radial de probabilidad con el método de los momentos. Encontrando grandes discrepancias entre ambos métodos, obteniendo $D \sim 2 \times 10^4$ m^2/s usando el primero y $D \sim 10^{-2}$ m^2/s usando el segundo para la configuración QTS4.

Estos resultados cuestionan la validez del modelo clásico de difusión y convección para describir adecuadamente el transporte de las partículas α atrapadas no colisionales en los campos magnéticos considerados.

Inspirados por el éxito de la teoría de transporte fraccionario para construir un modelo efectivo para el transporte generado por turbulencias en plasmas de fusión, implementamos sus herramientas para determinar la naturaleza efectiva del transporte radial de las partículas α atrapadas. Los coeficientes de transporte fraccionario: el exponente de Hurst H y los exponentes espacial α y temporal β se calcularon con

las técnicas Eularianas y Lagrangianas (con la metodología del propagator y el anaĺisis $[R/S]$ respectivamente) usando las trayectorias de las partículas α atrapadas para las cinco mismas configuraciones.

Tanto los análisis Eulerianos como los Lagrangianos revelan que el transporte de las partículas α atrapadas no colisionales es no difusivos, no Gaussianas, no Markovianas y fuertemente subdifusivas.

Como se esperaba, las partículas atrapadas, perfectamente confinadas, de la configuración ITER sin *ripple* se caracterizan por la ausencia de transporte radial con un exponente Hurst casi igual a cero, $H = 0.004 \pm 0.014$. Para los stellarators cuasi-toroidales los valores de los exponentes de Hurst estimados tanto por el método Euleriano como por el Lagrangiano resultaron ser los mismos, sugiriendo de forma clara un carácter fuertemente subdifusivo del transporte, que es cada vez más pronunciado a medida que los niveles de simetría cuasi-toroidal aumentan. Sólo para la configuración QTS72, los exponentes de Hurst resultantes no coincidían dentro de las barras de error, como consecuencia de sus rápidas pérdidas y efectos de tamaño finito.

Para los cuatro stellarators, los exponentes espaciales α resultantes señalan a una estadísticas no Gaussianas y la naturaleza no local del transporte. Los valores de α descienden fuertemente con valores de simetría decreciente y además $1/\alpha$ nunca excede los valores del exponente de Hurst estimados, revelando la presencia de fuertes anti-correlaciones espaciales. El valor atípico de $\alpha_{QTS4} = 2.7 \pm 0.9$, más que ser un indicador de una estadística Gaussiana, puede ser un artefacto debido a las pequeñas derivas radiales, para las que la técnica Euleriana es más sensible.

Los exponentes temporales, β, obtenidos por el método Euleriano indican un comportamiento del transporte significativamente no Markoviano y la relevancia de efectos de memoria. A pesar de que se encontró una gran disparidad entre $\beta_{QTS5/QTS6} \sim 0.2-0.3$ y $\beta_{QTS4/QTS72} \sim 0.5-0.7$, todos los valores de β se encontraban por bajo de 1. Estos resultados se compararon con una técnica más fiable que estima a β basado en H y α como $\beta = H\alpha$, que ofreció $\beta \sim 0.2$ para las cuatro configuraciones QTS.

Los resultados principales de esta tesis demuestran que el transporte de las partículas α atrapadas no colisionales no se puede describir adecuadamente mediante el enfoque clásico de convección/difusión para las configuraciones cuasi-toroidales que consideramos. Los coeficientes de transporte fraccionario indican que el transporte no di-

fusivo, no Gaussiano, no Markoviano y fuertemente subdifusivo. A medida que el nivel de simetría cuasi-toroidal aumenta, el transporte de las partículas α atrapadas se vuelve fuertemente subdifusivo. Sin embargo, la validez del modelo fraccionario en si mismo es mas dudosa en casos de simetría extremadamente altos o bajos.

El trabajo aquí presentado podría ser ampliado naturalmente en cuanto a: i) examinar la validez del modelo fraccionario de transporte en relación a otros tipos de configuraciones cuasi-simétricas o isodinámicas, ii) aclarar si la descripción no difusiva es todavía necesaria cuando se consideran las colisiones, iii) estudiar los efectos de la densidad, la temperatura y los perfiles de nacimiento de las partículas alfa, iv) considerar las inestabilidades MHD resonantes y no resonantes, etc.

Chapter 6

Conclusies

Dit proefschrift onderzocht de relatie tussen het botsingsloze α-deeltjestransport en het toroïdale symmetrieniveau van het magnetische veld en ging in op de aard van de onderliggende processen.

De statistische analyse van het transport van α-deeltjes werd uitgevoerd op basis van het ensemblegemiddelde van een groot aantal 'guiding-center orbit' trajecten die numeriek werden verkregen met de Monte Carlo-code MOCA. Er zijn drie benaderingen gemaakt die overeenstemmen met fusierelevante α-deeltjes: de kleine gyroradiusorde, het verwaarlozen van het elektrische veld, en het negeren van de botsingen met andere deeltjes.

De studie onderzocht vijf configuraties op reactorschaal: een rimpelloze ITER-tokamak en vier quasi-toroïdaal symmetrische (QTS) stellarators losjes gebaseerd op het NCSX-project. Deze configuraties worden gekenmerkt door een nieuw ontwikkelde quasi-toroïdale symmetriecijfer van orde σ_{qt}, waar $\sigma_{qt} = 1$ is voor de puur toroïdaal symmetrische ITER-configuratie en waar het varieert van $\sigma_{qt} = 0.94$ tot 0.62 voor de QTS stellarator-configuraties.

Voor elke configuratie analyseerden we de verliezen van α-deeltjes en hun afhankelijkheid van de geboorteposities van de deeltjes. De trajecten van α-deeltjes werden geclassificeerd als passerend of ingesloten, en hun fracties werden geschat op twee manieren: één gebaseerd op deeltjestrajecten en de andere op de magnetische putdiepte. Een nieuw ontwikkelde numerieke procedure classificeerde gevangen banen als voornamelijk bananen en in mindere mate gevangen aardappelen, rimpel en overgang. Voor ITER is de verhouding tussen passerende en gevangen deeltjes $\sim$ 70/30, zijn ze allemaal perfect opgesloten

en is 97% van de gevangen fractie een bananebaan. Voor de QTS-configuraties is de verhouding $\sim 80/20$, maar zijn sommige gevangen deeltjes zijn verloren gegaan. Een afwijking van QTS resulteert in snellere en grotere verliezen, waarbij het beperkende geval QTS72 is. Hier onsnappen bijna alle gevangen deeltjes en van de banen zijn 54% gevangen als bananen en 35% als rimpel. Zoals verwacht, behoren de meeste van die verliezen tot deeltjes die worden geboren met een kleine pitch in gebieden met een laag magnetisch veld aan het buitenste middenvlak.

Dit zijn precies de opgesloten α-deeltjes die voornamelijk verantwoordelijk zijn voor transport. Omwille van deze reden werd een nieuw algoritme ontwikkeld om het opgesloten baancentrum en zijn andere karakteristieke baanparameters te definiren, namelijk stuitertijden τ en breedtes Δw, vanuit hun traject. Er werd aangetoond dat de afname van het torusvormige symmetrieniveau resulteert in deeltrajecten met bredere bananenbanen en langere stuitertijden (de meest voorkomende waarden liggen in het bereik van $\Delta w \sim 0.15 - 0.25$ en $\tau \sim 20 - 30\ \mu$ s). Deze resultaten werden bevestigd door een onafhankelijke numerieke procedure op basis van verbindingslengtes langs de veldlijnen.

Convectiesnelheden en diffusiecofficinten werden geschat met behulp van de karakteristieke stuitertijden τ en breedtes Δw en door de tijdsafhankelijkheid van de momenten van de radiale kansverdelingsfunctie aan te passen aan de loopmomentenmethode. Er werden grote verschillen gevonden tussen beide methoden, b.v. $D \sim 2 \times 10^4$ m^2/s met de eerste en $D \sim 10^{-2}$ m^2/s met de tweede voor de QTS4-configuratie.

Deze resultaten stellen de validiteit van het klassieke convectie/diffusie model ter discussie om het botsingloze opgesloten α-deeltjes transport voor de beschouwde magnetische configuraties adequaat te beschrijven.

Geïnspireerd door het succes van de fractionele transporttheorie om een effectief transportmodel te bouwen voor turbulent aangedreven transport in fusieplasma's, hebben we de tools geïmplementeerd om de effectieve aard van het radiale transport van door rimpels versterkte α-deeltjes te bepalen. De fractionele transportcofficinten, dwz de Hurst H, de ruimtelijke α en de tijdelijke β exponenten, werden geschat met de Euleriaanse en Lagrangiaanse technieken (respectievelijk de propagator en de $[R/S]$ analyse) gebruik makend van de trajecten van

ingesloten α-deeltjes voor dezelfde vijf configuraties.

Zowel de Euleriaanse als de Lagrangiaanse analyse laten zien dat het transport van botsingsvrij opgesloten α-deeltjes niet-diffusieve kenmerken heeft die niet-Gaussiaans, niet-Markoviaans en sterk subdiffusief zijn.

Zoals verwacht, worden de perfect opgesloten deeltjes van de rimpelloze ITER-configuratie gekenmerkt door de afwezigheid van radiaal transport met bijna nul Hurst-exponent, $H = 0.004 \pm 0.014$. Voor de quasi-toroidale stellarators bleken de waarden van de Hurst-exponenten, geschat door zowel de Euleriaanse als de Lagrangiaanse methode, in overeenstemming te zijn, wat duidelijk wijst op een sterk subdiffusief karakter van transport, dat meer uitgesproken wordt naarmate het niveau van quasi-toroïdale symmetrie toeneemt. Alleen voor de QTS72-configuratie waren de resulterende Hurst-exponenten het niet eens binnen de foutmarges, een gevolg van de snelle verliezen en eindige grootte-effecten.

Voor de vier stellaratoren wijzen de resulterende ruimtelijke exponenten α op de niet-Gaussiaanse statistieken en het niet-lokale karakter van transport. De waarden van α nemen sterk af met afnemende symmetrie, bovendien overschrijdt de inverse waarde daarvan, $1/\alpha$, nooit de geschatte Hurst-exponenten, wat de aanwezigheid van sterke ruimtelijke anticorrelaties onthult. De atypische waarde van $\alpha_{QTS4} = 2.7 \pm 0.9$ zou, in plaats van een indicator te zijn voor Gauss-statistieken, een artefact kunnen zijn vanwege de verminderde ruimtelijke drift, waarvoor de Euleriaanse techniek gevoeliger is.

De temporele exponenten, β, verkregen volgens de Euleriaanse methode, wijzen op een significant niet-Markoviaans transportgedrag en de overeenkomstige relevantie van geheugeneffecten. Ondanks een grote ongelijkheid tussen $\beta_{QTS5/QTS6} \sim 0.2 - 0.3$ en $\beta_{QTS4/QTS72} \sim 0.5 - 0.7$ werd gevonden dat alle waarden van *beta* onder 1 blijven. Deze resultaten werden vergeleken met een betrouwbaardere techniek die β schat op basis van H en α als $\beta = H\alpha$, waarmee $\beta \sim 0.2$ verkreeg voor de vier QTS-configuraties.

De belangrijkste resultaten van dit proefschrift laten zien dat het botsingsloze opgesloten α-deeltjes transport niet adequaat kan worden beschreven door de klassieke convectie / diffusie benadering voor de quasi-toroïdaal symmetrische configuraties die worden beschouwd, maar dat de fractionele transporttheorie wel een effectief transportmodel kan bieden. De fractionele transportcofficinten geven aan dat

het transport niet diffuus is omdat het niet Gaussiaans, niet Markoviaans en sterk subdiffusief is. Naarmate het niveau van de quasi-toroïdale symmetrie toeneemt, wordt het door rimpel versterkte transport van α-deeltjes sterk subdiffusief. Hoewel de validiteit van het fractionele model zelf twijfelachtig wordt in de beperkende gevallen van hoge en lage symmetrie.

Het hier gepresenteerde werk zou op natuurlijke wijze kunnen worden uitgebreid door: i) de geldigheid van het fractionele transportmodel te onderzoeken op andere soorten quasi-symmetrische of isodynamische configuraties, ii) te verduidelijken of de niet-diffusieve beschrijving nog steeds nodig is wanneer botsingen worden overwogen, iii) de effecten van dichtheid, temperatuur en α-deeltjes geboorteprofielen te bestuderen, iv) te overwegen om resonante en niet-resonante MHD instabiliteiten er bij te betrekken, etc.

Bibliography

[1] BP Statistical Review of World Energy 2019. London: British Petroleum Co.

[2] IEA (2019). *World Energy Outlook 2019*. OECD Publishing, Paris.

[3] J.D. Lawson. *Proc. Phys. Soc. B.*, **70**(6), 1957.

[4] Weston M. Stacey. *Fusion Plasma Physics*. Wiley VCH, 2012.

[5] E. Rebhan and G. Van Oost. *Transactions of Fusion Science and Technology*, **49**, 2006.

[6] F. Wagner. *EPJ Web of Conferences*, **54**(6), 2013.

[7] A. H. Boozer and G. Kuo-Petravic. *Phys. Fluids*, **24**:851–859, 1981.

[8] H. E. Mynick. *Phys. of Plasmas*, **13**(058102), 2006.

[9] L.S. Hall and B. McNamara. *Physics of Fluids B*, **18**(5):552–565, 1975.

[10] J. Nührenberg. *Plasma Phys. Control. Fusion*, **52**(12):124003, 2010.

[11] P. Helander. *Reports on Progress in Physics*, **28**(1), 2014.

[12] M. C. Zarnstorff, L. A. Berry, A. Brooks, E. Fredrickson, G-Y. Fu, S. Hirshman, S. Hudson, L-P. Ku, E. Lazarus, D. Mikkelsen, D. Monticello, G. H. Neilson, N. Pomphrey, A. Reiman, D. Spong, D. Strickler, A. Boozer, W. A. Cooper, R. Goldston, R. Hatcher, M. Isaev, C. Kessel, J. Lewandowski,

J. F. Lyon, P. Merkel, H. Mynick, B. E. Nelson, C. Nührenberg, M. Redi, W. Reiersen, P. Rutherford, R. Sanchez, J. Schmidt, and R. B. White. *Plasma Physics and Controlled Fusion*, **43**(12A):A237–A249, 2001.

[13] D.A. Spong, S.P. Hirshman, L.A. Berry, J.F. Lyon, R.H. Fowler, A.S. Ware, D. Alban, R. Sanchez, G.Y. Fu, D.A. Monticello, W.H. Minerand, and P.M. Valanju. *Nuclear Fusion*, **41**(711), 2001.

[14] B. E. Nelson, L. A. Berry, A. B. Brooks, M. J. Cole, J. C. Chrzanowski, H. M. Fan, P. J. Fogarty, P. L. Goranson, P. J. Heitzenroeder, S. P. Hirshman, G. H. Jones, J. F. Lyon, G. H. Neilson, W. T. Reiersen, D. J. Strickler, and D. E. Williamson. *Fusion Engineering and Design*, **66-68**:205–210, 2003.

[15] F. S. B. Anderson, A. F. Almagri, D. T. Anderson, P. G. Mathews, J. N.Talmadge, and J. L. Shohet. *Fusion Technology*, **27**(273), 1995.

[16] B. B. Kadomtsev and O. P. Pogutse. *Sov. Phys. JETP*, **24**:1172–1179, 1967.

[17] P. Helander. *Fusion Science and Technology*, **61**(2T):133–141, 2012.

[18] A. Fick. *Annalen der Physik*, **170**(59-86), 1855.

[19] I. Podlubny. *Fractional Differential Equations*. Academic Press, 1998.

[20] E.W. Montroll and G.H. Weiss. *J. Math. Phys.*, 6:167, 1965.

[21] R. Metzler and J. Klafter. *Phys. Rep.*, **339**:1, 2000.

[22] B. A. Carreras, B. Van Milligen, C. Hidalgo, R. Balbin, E. Sanchez, I. Garcia-Cortes, M. A. Pedrosa, J. Bleuel, and M. Endler. *Physical Review Letters*, **83**:3653–3656, 1999.

[23] B. A. Carreras, B. Ph Van Milligen, M. A. Pedrosa, R. Balbín, C. Hidalgo, D. E. Newman, E. Sánchez, R. Bravenec, G. McKee, I. García-Cortés, J. Bleuel, M. Endler, C. Ricardi, S. Davies,

G. F. Matthews, E. Martines, and V. Antoni. *Physics of Plasmas*, **6**:1885–1892, 1999.

[24] C. X. Yu, M. Gilmore, W. A. Peebles, and T. L. Rhodes. *Physics of Plasmas*, **10**:2772–2779, 2003.

[25] B. A. Carreras, V. E. Lynch, and G. M. Zaslavsky. *Phys. Plasmas*, **8**:5096, 2001.

[26] D. Del-Castillo-Negrete, B. A. Carreras, and V. E. Lynch. *Phys. Rev. Lett.*, **94**:065003, 2005.

[27] D. Del-Castillo-Negrete. *Nonlinear Proc. Geoph.*, **17**:795, 2010.

[28] L. Garcia and B. A. Carreras. *Phys. Plasmas*, **13**:022310, 2006.

[29] J. A. Mier, L. García, and R. Sánchez. *Phys. Plasmas*, **13**:102308, 2006.

[30] J. A. Mier, R. Sánchez, L. García, B. A. Carreras, and D. E. Newman. *Phys. Rev. Lett.*, **101**:165001, 2008.

[31] J. A. Mier, R. Sánchez, L. García, D. E. Newman, and B. A. Carreras. *Phys. Plasmas*, **15**:112301, 2008.

[32] X. Garbet and R. E. Waltz. *Phys. Plasmas*, **5**:2836, 1998.

[33] R. Sánchez, D. E. Newman, J. N. Leboeuf, V. K. Decyk, and B. A. Carreras. *Phys. Rev. Lett.*, **101**:205002, 2008.

[34] R. Sánchez, D. E. Newman, J. N. Leboeuf, B. A. Carreras, and V. K. Decyk. *Phys. Plasmas*, **16**:055905, 2009.

[35] R. Sanchez, D. E. Newman, J. N. Leboeuf, and V. K. Decyk. *Plasma Phys. Control. Fusion*, **53**:074018, 2011.

[36] J. A. Alcuson, J. M. Reynolds-Barredo, A. Bustos, R. Sanchez, V. Tribaldos, P. Xanthopoulos, T. Goerler, and D. E. Newman. *Physics of Plasmas*, **23**(10):102308, 2016.

[37] G. Sánchez Burillo, B. Ph Van Milligen, and A. Thyagaraja. *Phys. Plasmas*, **16**:042319, 2009.

[38] K. Gustafson, P. Ricci, I. Furno, and A. Fasoli. *Phys. Rev. Lett.*, **108**:035006, 2012.

[39] A. Bovet, I. Furno, A. Fasoli, K. Gustafson, and P. Ricci. *Nuc. Fusion*, **52**:094017, 2012.

[40] A. Bovet, I. Furno, A. Fasoli, K. Gustafson, and P. Ricci. *Plasma Phys. Control. Fusion*, **55**:124021, 2013.

[41] A. Bovet, M. Gamarino, I. Furno, P. Ricci, A. Fasoli, K. Gustafson, D. E. Newman, and R. Sánchez. *Nuc. Fusion*, **54**:104009, 2014.

[42] I. Furno, A. Bovet, A. Fasoli, C. Gauthey, K. Gustafson, P. Ricci, and B. Ph Van Milligen. *Plasma Phys. Control. Fusion*, **58**:014023, 2015.

[43] R. Sánchez and D. E. Newman. *Plasma Phys. Control. Fusion*, **57**(123002):1–56, 2015.

[44] R. D. Hazeltine. Recursive derivation of drift-kinetic equation. *Plasma Physics*, **15**(1):77–80, jan 1973.

[45] A. Einstein. *Ann. Phys. Lpz.*, **332**:549–60, 1905.

[46] R.H. Fowler, J.A. Rome, and J.F. Lyon. *Phys. Fluids*, **28**(1), 1985.

[47] J. Egedal. *Nuclear Fusion*, **40**:1597–1610, 2000.

[48] B. B. Kadomtsev, O. P. Pogutse, and I. V. Kurchatov. *Nuclear Fusion*, **11**:67–92, 1971.

[49] T. E. Stringer. *Plasma Physics*, **16**(7):651–659, 1974.

[50] A. H. Boozer. *Phys. Fluids*, **23**:2283, 1980.

[51] F. Porcelli, L. G. Eriksson, and I. Furno. *Physics Letters A*, **216**(6):289–295, 1996.

[52] A.J. Brizard. *Physics of Plasmas*, **18**:022508, 2011.

[53] K. C. Shaing, M. Schlutt, and A. L. Lai. *Physics of Plasmas*, **23**(2):022508, 2016.

[54] V. P. Nagornyj and V. A. Yavorskij. *Sov. J. Plasma Phys.*, **15**(5):534–545, 1989.

[55] M. Wakatani. *Stellarator and Heliotron Devices*. Oxford University Press, 1998.

[56] J. A. Rome. *Nuclear Fusion*, **35**(2):195–206, 1995.

[57] R. Farengo, H. E. Ferrari, M. C. Firpo, P. L. Garcia-Martinez, and A. F. Lifschitz. *Plasma Physics and Controlled Fusion*, **54**:025007, 2012.

[58] M. Khan, A. Zafar, and M. Kamran. *Journal of Fusion Energy*, **34**(2):298–304, 2015.

[59] R. J. Goldston and H. H. Towner. *J. Plasma Phys.*, **26**:283, 1981.

[60] R. J. Goldston, R. B. White, and A. H. Boozer. *Physical Review Letters*, **47**:647–649, 1981.

[61] K. Tani, T. Takizuka, M. Azumi, and H. Kishimoto. *Nuclear Fusion*, **23**:657–665, 1983.

[62] R. B. White, R. J. Goldston, M. H. Redi, and A. R.V. Budny. *Physics of Plasmas*, **3**:3043–3054, 1996.

[63] Ya I. Kolesnichenko and V. A. Yavorskij. *Nuclear Fusion*, **29**:1319–1323, 1989.

[64] I. G. Eriksson and P. Helander. *Nuclear Fusion*, **33**:767–775, 1993.

[65] R. B. White and H. E. Mynick. *Phys. Fluids B*, **1**:980–982, 1989.

[66] W..W. Heidbrink and G. J. Sadler. *Nuc. Fusion*, **34**:535–615, 1994.

[67] S. V. Putvinskij, B. J.D. Tubbing, L. G. Eriksson, and S. V. Konovalov. *Nuclear Fusion*, **34**:495–506, 1994.

[68] R. L. Boivin, S. J. Zweben, and R. B. White. *Nuclear Fusion*, **33**:449–465, 1993.

[69] M. H. Redi, M. C. Zarnstorff, R. B. White, R. V. Budny, A. C. Janos, D. K. Owens, J. F. Schivell, S. D. Scott, and S. J. Zweben. *Nuclear Fusion*, **35**:1191–1211, 1995.

[70] M. H. Redi, R. V. Budny, D. S. Darrow, H. H. Duong, R. K. Fisher, A. C. Janos, J. M. McChesney, D. C. McCune, S. S. Medley, M. P. Petrov, J. F. Schivell, S. D. Scott, R. B. White, M. C. Zarnstorff, and S. J. Zweben. Modelling TF ripple loss of alpha particles in TFTR DT experiments. *Nuclear Fusion*, **35**(12):1509–1516, dec 1995.

[71] P. N. Yushmanov. *Nuclear Fusion*, **23**:1599–1612, 1983.

[72] K. Tani, T. Takizuka, and M. Azumi. *Nuclear Fusion*, **33**:903–914, 1993.

[73] V. Ya Goloborod'ko and V. A. Yavorskij. *Nuclear Fusion*, **24**:627–631, 1984.

[74] L. M. Kovrizhnykh and S. G. Shasharina. *Nuclear Fusion*, **30**:453–469, 1990.

[75] P. N. Yushmanov, J. R. Cary, and S. G. Shasharina. *Nuclear Fusion*, **33**:1293–1303, 1993.

[76] M. Isobe, K. Tobita, T. Nishitani, Y. Kusama, and M. Sasao. *Nuclear Fusion*, **37**:437–444, 1997.

[77] V. A. Yavorskij, D. Darrow, V. Ya Goloborod'Ko, S. N. Reznik, U. Holzmueller-Steinacker, N. Gorelenkov, and K. Schoepf. *Nuclear Fusion*, **42**:1210–1215, 2002.

[78] K. G. McClements. *Physics of Plasmas*, **12**:1–8, 2005.

[79] K. C. Shaing, J. A. Rome, and R. H. Fowler. *Physics of Fluids*, **27**:1–4, 1984.

[80] W. Lotz, P. Merkel, J. Nührenberg, and E. Strumberger. *Plasma Physics and Controlled Fusion*, **34**:1037–1052, 1992.

[81] C. D. Beidler, Ya. I. Kolesnichenko, V. S. Marchenko, I. N. Sidorenko, and H. Wobig. *Physics of Plasmas*, **8**(6):2731–2738, 2001.

[82] Ya I. Kolesnichenko, V. V. Lutsenko, A. V. Tykhyy, A. Weller, A. Werner, H. Wobig, and J. Geiger. *Physics of Plasmas*, **13**:072504, 2006.

[83] A. V. Tykhyy, Ya I. Kolesnichenko, Yu V. Yakovenko, A. Weller, and A. Werner. *Plasma Physics and Controlled Fusion*, **49**:703–711, 2007.

[84] V. S. Marchenko and S. N. Reznik. *Plasma Physics and Controlled Fusion*, **58**:055004, 2016.

[85] K. C. Shaing and S. A. Hokin. *Physics of Fluids*, **26**:2136–2139, 1983.

[86] M. S. Smirnova. *Nuclear Fusion*, **36**(11):1455–1476, 1996.

[87] M. S. Smirnova. Effect of high order magnetic field harmonics on trapped particle confinement in torsatrons and heliotrons. *Nuclear Fusion*, **36**(11):1455–1476, nov 1996.

[88] J. M. Faustin, W. A. Cooper, J. P. Graves, D. Pfefferlé, and J. Geiger. *Nuclear Fusion*, **56**:092006, 2016.

[89] O. Fischer, W. A. Cooper, M. Yu Isaev, and L. Villard. *Nuclear Fusion*, **42**:817–826, 2002.

[90] M. D. J. Cole, R. Hager, T. Moritaka, S. Lazerson, R. Kleiber, S. Ku, and C. S. Chang. *Physics of Plasmas*, **26**(3):032506, 2019.

[91] S. V. Konovalov, E. Lamzin, K. Tobita, and Yu. Gribov. In *28th EPS Conference on Contr. Fusion and Plasma Phys., Funchal, 18-24 June, ECA Vol.* ***25A***, pages 613–616, 2001.

[92] M. Drevlak, J. Geiger, P. Helander, and Y. Turkin. *Nuclear Fusion*, **54**(7):073002, 2014.

[93] S. A. Henneberg, M. Drevlak, C. Nührenberg, C. D. Beidler, Y. Turkin, J. Loizu, and P. Helander. *Nuc. Fusion*, **59**:026014, 2018.

[94] V. Tribaldos. *Physics of Plasmas*, **8**(4):1229–1239, 2001.

[95] J. M. Reynolds-Barredo, V. Tribaldos, A. Loarte, A. R. Polevoi, M. Hosokawa, and R. Sánchez. *Submitted for publication to Nuc. Fusion*, 2019.

[96] D. Del-Castillo-Negrete, B. A. Carreras, and V. E. Lynch. *Phys. Plasmas*, **11**:3854, 2004.

[97] J. Jacquinot, S. Putvinski, G. Bosia, A. Fukuyama, R. Hemsworth, S. Konovalov, Y. Nagashima, W. M. Nevins, F. Perkins, K. Rasumova, F. Romanelli, K. Tobita, K. Ushigusa, J. W. Van Dam, V. Vdovin, and S. Zweben. ITER Physics Basis. *Nuclear Fusion*, **39**(12):2471–2494, 1999.

[98] A. Fasoli, C. Gormenzano, H.L. Berk, B. Breizman, S. Briguglio, D.S. Darrow, N. Gorelenkov, W.W. Heidbrink, A. Jaun, S.V. Konovalov, R. Nazikian, J.-M. Noterdaeme, S. Sharapov, K. Shinohara, D. Testa, K. Tobita, Y. Todo, G. Vlad, and F. Zonca. *Nuclear Fusion*, **47**:S264–S284, 2007.

[99] V. Yavorskij, L. G. Eriksson, V. Kiptily, K. Schoepf, and S. E. Sharapov. *Journal of Fusion Energy*, **34**(4):774–784, 2015.

[100] D. Palumbo. *Il Nuovo Cimento B Series*, **61**(2T):133–141, 1968.

[101] R.V. Budny. *Nuclear Fusion*, **41**(711-716):711–716, 2002.

[102] S. P. Hirshman, W. I. van RIJ, and P. Merkel. *Computer Physics Communications*, **43**:143–155, 1986.

[103] J. Geiger, C. D. Beidler, Y. Feng, H. Maaßberg, N.B. Maruschenko, and Y. Turkin. *Plasma Phys. Control. Fusion*, **57**(014004):1–11, 2015.

[104] C. D. Beidler, K. Allmaier, M. Yu. Isaev, S. V. Kasilov, W. Kernbichler, G. O. Leitold, H. Maaßberg, D. R. Mikkelsen, S. Murakami, M. Schmidt, D. A. Spong, V. Tribaldos, and A. Wakasa. *Nuclear Fusion*, **51**(7):076001, 2011.

[105] G. Kuo-Petravic. *Journal of Computational Physics*, **52**(1):209–213, 1983.

[106] S. Äkäslompolo, T. Kurki-Suonio, O. Asunta, M. Cavinato, M. Gagliardi, E. Hirvijoki, G. Saibene, S. Sipilä, A. Snicker, K. Särkimäki, and J. Varje. *Nuclear Fusion*, **55**(9):093010, 2015.

[107] W. T. Vetterling W. H. Press, S. A. Teukolsky and B. P. Flannery. *Numerical Recipes - The Art of Scientific Computing*. Cambridge University Press, second edition, 1994.

[108] A. A. Galeev and R. Z. Sagdeev. *Sov. Phys. JETP*, **26**(1):233–240, 1968.

[109] M. N. Rosenbluth, R. D. Hazeltine, and F. L. Hinton. *Physics of Fluids*, **15**(1):116–140, 1972.

[110] S. P. Hirshman and D. J. Sigmar. *Nuc. Fusion*, **21**:1079–1201, 1981.

[111] R. Sánchez and D. Newman. *A Primer on Complex Systems - With Applications to Astrophysical and Laboratory Plasmas*. Springer Netherlands, 2018.

[112] N. Wiener. *Journal of Mathematics and Physics*, **2**(1-4):131–174, 1923.

[113] M. Kac. *Proceedings of the National Academy of Sciences*, **35**(5):252–257, 1949.

[114] R. Balescu. *Aspects of Anomalous Transport in Plasmas*. CRC Press, 2005.

[115] D. L. Book. NRL Plasma Formulary. Naval research Laboratory, Washington, DC, 1990.

[116] G. Spizzo, R. White, M. Maraschek, V. Igochine, and G. Granucci. Nonlocal transport in toroidal plasma devices. *Nuc. Fusion*, **59**(1):016019, 2018.

[117] A. Croitoru, D.I. Padale, M. Vlad, and F. Spineanu. *Nuc. Fusion*, **57**:036019, 2017.

[118] A. Gogoleva, V. Tribaldos, J.M. Reynolds-Barredo, and C.D. Beidler. *Nuc. Fusion*, **60**:056009, 2020.

[119] V. Tribaldos and J. Guasp. *Plasma Phys. Control. Fusion*, **47**:545, 2005.

[120] G. Samoradnitsky and M.S. Taqqu. *Stable non-Gaussian random processes: Stochastic models with infinite variance*. Stochastic modeling. Chapman & Hall, New York, 2017.

[121] H. E. Hurst. *Transactions of the American Society of Civil Engineers*, **116**:770, 1951.

List of Figures

List of Tables